Fluid-Structure Interaction Modeling of Pulmonary Artery Blood Flow in End-Stage Renal Disease Patients

By Daniel Pearce, M.S.B.E

July 2020

Directed by: Stephanie George, Ph.D.

Department of Engineering

If unaddressed, end-stage renal disease (ESRD) can result in impaired renal function, development of cardiovascular diseases, and death. Although effective, dialysis conducted via arteriovenous fistulas (AVF) has been linked to the development of pulmonary hypertension (PH). The objective of this work was to use magnetic resonance imaging (MRI) and computational fluid dynamics (CFD) to model pulmonary artery (PA) blood flow and PA fluid-structure interactions so properties of these models could be related to clinical parameters relevant to PH and ESRD. Due to the global pandemic, one (*n* =1) adult ESRD patient underwent cardiac MRI for PA reconstruction. Short-axis cine scans and phase-contrast scans were used respectively to recreate the patient's PA geometry in Mimics 20.0, an imaging segmentation software, and derive a patient-specific velocity waveform of blood flow at the PA inlet. Computational fluid dynamics (CFD) and finite element models of vessel deformation were created in ANSYS Workbench 19.1. Steady-state models (CFD, linear elastic fluid-structure interaction (FSI), and hyperelastic FSI) were run using a constant inlet velocity and, where applicable, mechanical properties for vessel walls taken from literature. Transient models (CFD and linear elastic FSI) were also created to simulate pulsatile blood flow and, where applicable, the interaction with the artery wall. Moderate differences were observed among the various steady-state models, whereas only minimal differences were found between transient models. These differences may be due to limited mesh resolution, which was later identified in a mesh sensitivity analysis. Although only minor

differences were found between fluid results for the transient CFD and FSI model, the computational cost of the FSI model was much greater. FSI models of PA hemodynamics may not offer different results for hemodynamic properties, but they may be used in future studies when arterial remodeling and cellular stress and strain distributions are of interest. This study offered insight into computational modeling of PA blood flow and may be used as reference for future studies seeking to apply this methodology to a larger patient population. Eventually, this type of modeling may be used to identify metrics of interest that physicians can use to more closely monitor AVF development during hemodialysis.

Fluid-Structure Interaction Modeling of Pulmonary Artery Blood Flow in End-Stage Renal Disease Patients

A THESIS

Presented to the Faculty of the Department of Engineering

College of Engineering and Technology

East Carolina University

In Partial Fulfillment of Requirements for the Degree

Master of Science in Biomedical Engineering

By

Daniel Pearce

July 2020

Fluid-Structure Interaction Modeling of Pulmonary Artery Blood Flow in End-Stage Renal Disease Patients

By Daniel Pearce

APPROVED BY:

Stephanie George, Ph.D., Director

Ali Vahdati, Ph.D., Committee Member

Robert Lust, Ph.D., Committee Member

Veeranna Maddipati, M.D., Committee Member

Barbara Muller-Borer, Ph.D., Department Chairperson

Paul J. Gemperline, Ph.D.

Dean of the Graduate School

ACKNOWLEDGEMENTS

This work was funded by the East Carolina University Department of Engineering and Faculty Senate’s Research/Creative Activities Committee. In addition, I would like to further acknowledge and thank the physicians on the team, Dr. Maddipati and Dr. Marcu, for their constant help with all things clinical and for showing me what pulmonary arteries and arteriovenous fistulas look like in MR images; Dr. Lust for agreeing to help out with the project during such a chaotic time; Dr. Cynthia Christiano for helping further inform us about end-stage renal disease; the prospective patient for agreeing to participate in the study; Keith Thomson for all the technical support required throughout this project; Dr. Vahdati for allowing me to use his desktop computer and for his always encouraging attitude; and Dr. George, for always sharing her expertise and for showing me what I want do with my career in the future.

TABLE OF CONTENTS

LIST OF TABLES

LIST OF FIGURES

ALPHABETICAL GLOSSARY

- **2D –** Two-Dimensional
- **3D –** Three-Dimensional
- **4D –** Four-Dimensional
- **AVF –** Arteriovenous Fistula
- **CFD –** Computational Fluid Dynamics
- **CKD –** Chronic Kidney Disease
- **CO –** Cardiac Output
- **CT –** Computed Tomography
- **ESRD –** End-Stage Renal Disease
- **FSI –** Fluid-Structure Interaction
- **GFR –** Glomerular Filtration Rate
- **GRE** – Gradient Recalled Echo
- **IRB –** Internal Review Board
- **mPAP –** Mean Pulmonary Artery Pressure
- **MRI –** Magnetic Resonance Imaging
- **OSI –** Oscillatory Shear Index
- **PA –** Pulmonary Artery
- **PC-MRI –** Phase-Contrast Magnetic Resonance Imaging
- **PCWP –** Pulmonary Capillary Wedge Pressure
- **PH –** Pulmonary Hypertension
- **PISO –** Pressure Implicit with Split Operator
- **PVR –** Pulmonary Vascular Resistance
- **RHC –** Right Heart Catheterization
- **SAWSS –** Spatially Averaged WSS
- **SIMPLE –** Semi-Implicit Method for Pressure Linked Equations
- **sPAP –** Systolic Pulmonary Artery Pressure
- **TAWSS –** Time-Averaged WSS
- **TR –** Tricuspid Regurgitation
- **UDF –** User-Defined Function
- **WSS –** Wall Shear Stress

CHAPTER 1. INTRODUCTION

1.1 Overview and Proposed Work

Over 50 million Americans suffer from chronic kidney disease [1]. If this condition is unaddressed or improperly managed, it can develop into end-stage renal disease, which is a life-threatening and progressive condition characterized by severely impaired renal function, anemia, and the development of various cardiovascular diseases. In 2013, over 117,000 new cases of end-stage renal disease were reported and 5-7% annual increases in the number of diagnoses made have been seen in recent years [2]. In addition to this increasing prevalence, serious health disparities for African Americans (3-fold increased prevalence compared to other races) and Hispanics (1.4-fold increased prevalence compared to non-Hispanics) were observed [2].

The surgical creation of an arteriovenous fistula intended for use in hemodialysis is one of the most common ways to indefinitely manage end-stage renal disease; unfortunately, recent studies have suggested connections between fistula creation and the development of pulmonary hypertension, which is a progressive and life-threatening condition characterized by elevated pressures in the pulmonary vasculature, in this patient population [3]–[6]. It is believed that quantitative evidence supporting this connection and correlations between fistula shape and flow and the development of pulmonary hypertension may be used by physicians to monitor end-stage renal disease patients at risk of developing pulmonary hypertension and to encourage earlier preventative measures to alter fistula flow. Advancement of modeling techniques used to simulate PA blood flow, such as computational fluid dynamics and fluid-structure interaction modeling with different material models, may offer insight into hemodynamic properties and stress-strain distributions in the arterial wall that can be used to better study PH development in this population.

Prevention of pulmonary hypertension is critical in this patient population not only because of the complications of elevated pulmonary artery pressures, but also because end-stage renal disease patients with pulmonary hypertension are removed from the kidney transplant list. It is clear that a better understanding of the connections between fistula creation and pulmonary hypertension development in this patient population will lead to improved monitoring and risk identification, and may offer physicians evidence for earlier surgical interventions intended to limit the detrimental effects of hemodialysis conducted through arteriovenous fistulas. In time, this may lead to better healthcare outcomes for this patient population and a reduction of the aforementioned health disparities associated with this condition.

1.2 Organization of Thesis

Chapter 1 of this document provides an overview of the work and an outline for the following chapters. Chapter 2 covers the relevant anatomy and physiology of chronic kidney disease, end-stage renal disease, and pulmonary hypertension; various non-invasive screening and monitoring techniques for pulmonary hypertension; and includes an explanation of computational fluid dynamics, fluid-structure interaction models, and a review of literature pertaining to models of pulmonary artery and arteriovenous fistula hemodynamics. Chapter 3 explains the methodology used for patient recruitment, steady-state model setup, transient model set-up, and model analysis, whereas Chapter 4 explains the results obtained through this methodology. Chapter 5 is a discussion of results and the significance thereof, as well as steps that should be carried out in future projects concerning this subject matter. Finally, Chapter 6 is a conclusion of the thesis. This is followed by a list of references sorted numerically, supplementary figures and tables, and documents related to the ethical concerns of this study.

CHAPTER 2. BACKGROUND

This section of the thesis serves as an overview of kidney anatomy and physiology, chronic kidney disease and end-stage renal disease, the disease's prevalence, current treatment protocol, and treatment shortcomings. It also discusses pulmonary hypertension development in this patient population, screening and diagnostic techniques for pulmonary hypertension, and the clinical implications of using computational fluid dynamics to model blood flow through patient-specific models of pulmonary arteries and fistulas. This chapter provides a basic overview of physiology and pathology related to ESRD and PH, as well as a review of both clinical and technical literature related to this project.

2.1 Kidney Anatomy and Physiology

The kidneys (Figure 2.1) are located against the dorsal wall of the abdominal cavity, and are covered by fibrous capsules [7]. Together, the kidneys serve to filter blood delivered through the descending aorta, renal artery, and renal arterioles. They also serve to maintain net fluid balance and help regulate hormones influencing blood pressure. Kidneys can receive roughly 1000 mL of blood per minute, which is about 20% of total cardiac output in a healthy individual [7]. Blood delivered to the kidneys flows through the encapsulated glomerulus and is either filtered into a nephron or allowed to continue flowing through a connected arteriole. A nephron (Figure 2.2) is the functional filtration unit of the kidneys; these structures are housed within the renal cortex.

Unfiltered blood first enters into the nephron by way of the afferent arteriole, where it then passes through the glomerulus. A portion of blood plasma is filtered at the glomerulus and into the Bowman's Capsule. This ultrafiltrate of plasma then flows into the proximal tubule, where most of the water reabsorption occurs. The plasma ultrafiltrate then flows through the Loop of Henle, the distal convoluted tubule, and into the collecting duct, which collects filtrate and absorbs more water under the control of vasopressin. The remaining filtrate, or urine, flows through the collecting duct, into the renal pelvis, and into the ureter [7]. Urine is then collected in the bladder until it is voluntarily excreted.

By filtering waste and toxins from the circulatory system, the kidneys maintain a stable, homeostatic extracellular environment and help regulate complex ionic balances. These balances, whether it be sodium, potassium, chloride, or calcium, allow for proper physiological function. Kidney performance is typically assessed by glomerular filtration rates (GFR) and is defined as the total amount of fluid filtered through functioning nephrons per unit time [1], [7]. For healthy individuals, this value typically ranges between 90 – 120 mL/min/1.73 m^2 [7]. Kidney function can be compromised by elevated blood pressures, diabetic complications, interstitial nephritis, and a variety of environmental factors and lifestyle choices [1].

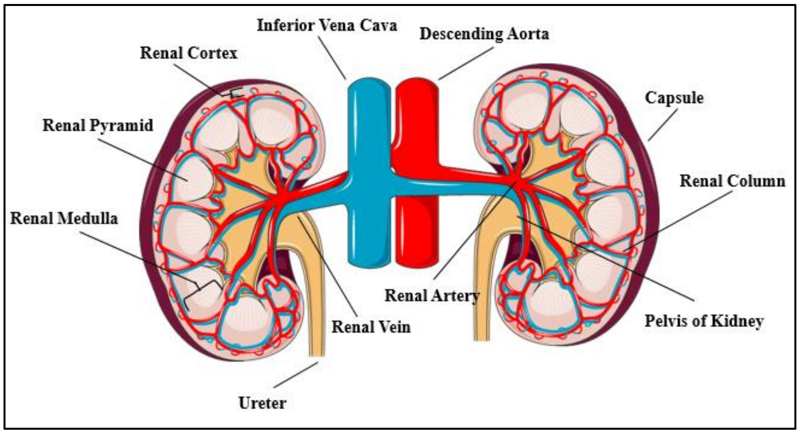

Figure 2.1. Illustrated human kidney anatomy.

This image was taken from Servier Medical Art by Les Laboratoires Servier under a Creative Commons License [8]. License available at: https://creativecommons.org/licenses/by/3.0/us/legalcode.

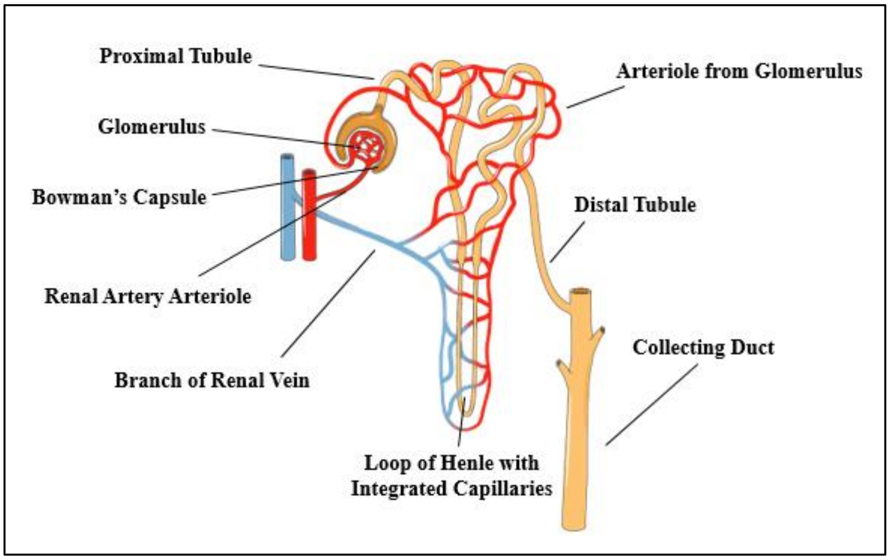

Figure 2.2. An illustrated nephron.

This image was taken from Servier Medical Art by Les Laboratoires Servier under a Creative Commons License [8]. License available at: https://creativecommons.org/licenses/by/3.0/us/legalcode.

2.2 Chronic Kidney Disease and End-Stage Renal Disease

Over 15% of adults in the United States have chronic kidney disease (CKD) caused by permanent structural damage to the kidneys that results in impaired renal function defined by a GFR ≤ 60 mL/min [1]. As this condition progresses, kidney function will continue to suffer. Once a patient's GFR falls below 15 mL/min, individuals are classified as having reached end-stage renal disease (ESRD) [1]. Complications of CKD progression and ESRD development include nausea, central nervous system depression, anemia, pathological mineral calcification, various cardiovascular disease, and, if unaddressed, death [1]. Individuals with diabetes, elevated blood pressures, cardiovascular diseases, and genetic predispositions are all at higher risks of developing ESRD. Additionally, African-American, Hispanic, Native American, Asian, and elderly patients all suffer from higher rates of ESRD [9]. It is estimated roughly 100,000 patients progress to ESRD annually [2], [10].

2.3 End-Stage Renal Disease Management

ESRD management is both time and resource intensive. Estimates suggest the United States spent over $25 billion on ESRD care in 2013. This accounts for almost 7% of all United States Medicare expenditures [11]. The most common form of disease management for ESRD patients is replacement therapy. This includes methods such as total organ transplant, peritoneal dialysis, and hemodialysis, which is the most common form of replacement [12]. While total organ transplants provide ESRD patients with new, functional kidneys, this method is limited by the number of available donors and demand regularly far exceeds supply. Furthermore, increased mortality rates also have been associated with this method for patients with a higher body mass index [13]. Since obesity is often present in CKD and ESRD, this is a critical limitation [14], [15]. Peritoneal dialysis, which involves waste product filtration via a catheter inserted through a patient's abdomen, has recently been suggested to have better outcomes compared to hemodialysis; however, not all patients are eligible for this management option and there is an increased risk of infection associated with peritoneal dialysis. This has resulted in an underutilization of peritoneal dialysis [11]. Thus, hemodialysis is the most commonly used method for ESRD management.

Hemodialysis accounts for over 64% of renal replacement therapy plans and requires creation of an arteriovenous fistula (AVF; shown in Figure 2.3) to allow for increased blood flow through a dialysis machine and back to the right side of a patient's heart [16], [17]. The three most common AVFs created in ESRD patients include radiocephalic fistulas, which are usually created in the distal forearm; brachiocephalic fistulas, usually created in the proximal forearm; and brachial artery-to-transposed basilica vein fistulas in the upper arm [18]. Radiocephalic fistulas are created by anastomosing the end of the cephalic vein to the side of the radial artery and are recommended as the first choice for fistula creation since it preserves future options for access sites [18]. Most fistulas mature within six weeks of creation and roughly 90% of all AVFs are developed and able to be used for dialysis within eight months of creation. This development, which is marked by an increase in fistula diameter and blood flow through the fistula, is often referred to as *maturation* [19]. One disadvantage of radiocephalic fistulas is increased rates of nonmaturation, defined by early thrombosis or the inability to be used successfully for dialysis over a sustained period of time; however, it should be noted there is no universally agreed upon definition of nonmaturation or AVF failure [20].

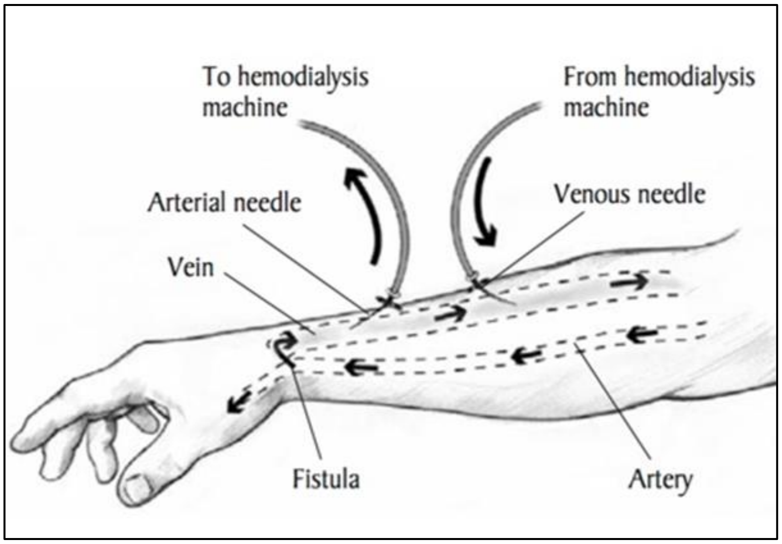

Figure 2.3. An illustrated arteriovenous fistula.

An illustrated arteriovenous fistula in a patient's right forearm [21].

While dialysis can work indefinitely to prolong patient's lives, serious comorbidities can develop during this treatment. One of these conditions is pulmonary hypertension (PH), clinically diagnosed by a mean pulmonary artery pressure (mPAP) $\geq$ 20 mmHg. Many of these patients develop pre-capillary PH, defined by an mPAP $\geq$ 20 mmHg, a pulmonary capillary wedge pressure (PCWP) $\leq$ 15 mmHg, and a pulmonary vascular resistance (PVR) $\geq$ 3 Wood Units upon right heart catheterization (RHC) [22], [23]. Pre-capillary PH is a life-threatening, progressive disease contributing to right heart failure, elevation of pressure in the vessels carrying blood to the lungs, and, if left untreated, death [24]. It is estimated between 30 – 50% of ESRD patients develop pre-capillary PH and suffer from impaired endothelial function, increased cardiac output, myocardial defects, and left heart dysfunction [25]. More information on PH is given in Section 2.4.

A number of recent studies have explored connections between matured AVFs and PH development in ESRD patients. In 2003, Yigla et al. [3] observed a PH prevalence of nearly 40%

in hemodialysis patients with fistulas. These PH patients had significantly higher cardiac outputs than normotensive dialysis patients (6.9 L/min vs. 5.5 L/min), prompting this group to later claim that dialysis may promote dysfunctional endothelium that reduces the ability of the pulmonary vasculature to accommodate AVF-induced increases in cardiac output [4]. Similar findings were reported by Dagli et al. [5], who discovered significantly increased AVF flow rates in pre-capillary PH patients when compared to normotensive patients, and Santosh et al. [6], who found that systolic pulmonary artery pressure (sPAP) increases by roughly 2.4 mmHg/year in patients undergoing dialysis. This finding seemed to suggest that patients have an increased risk of developing PH the longer they remain on dialysis [26], [27]. This work purports multiple physiological factors may lead to PH development, including volume overload, increased pulmonary flow, and increased pulmonary pressure [28]. These altered conditions can lead to ventricular hypertrophy, ventricular dilation, and elevated diastolic pressures [29]. However, the exact developmental mechanisms and pathogenesis of PH in ESRD patients are unclear and there are some conflicts in the existing literature about AVF creation and its underlying connection to increased pulmonary pressures. Acarturk et al. [30] and Unal et al. [31] both reported no correlation between flow rates of blood through AVFs and increases in mPAP. Likewise, a recent study by Hayati et al. [32] claimed there is little connection between ESRD and the development of PH and that the presence of PH plays a negligible role in the duration of dialysis, which differs from findings reported earlier [6], [26], [27]. One possible explanation for these discrepancies is the lack of a consistent definition for PH used in these studies.

There is clearly conflicting evidence in the available literature pertaining to this problem. While some studies have reported that AVF flow rates are correlated with increased PA pressures, few studies have explored connections between fistula creation and performance and the development of PH in ESRD patients. Even fewer studies, if any at all, have offered quantitative evidence suggesting a direct connection between fistula shape or hemodynamics and PA hemodynamics.

2.4 The Heart and Pulmonary Hypertension

The superior and inferior vena cava carry deoxygenated blood into the right atrium of the heart through a process known as venous return. This blood flows through the tricuspid valve and into the right ventricle, where it is pumped through the pulmonary valve and into the PA. Deoxygenated blood then flows through the main PA and towards the lungs through either the right or left PA, which both bifurcate into many smaller vessels as they approach the lungs. Deoxygenated blood flows through the pulmonary capillaries at the lungs, where bicarbonate is converted to carbon dioxide. This carbon dioxide leaves the pulmonary capillary along a concentration gradient. Oxygen enters into the pulmonary capillary by diffusion, binds to hemoglobin molecules in the blood, and that blood then flows back to the heart through the pulmonary veins. Freshly oxygenated blood flows through the left atrium, through the mitral valve, and is pumped from the left ventricle into the aorta, where it flows to the rest of the body. The aforementioned anatomical landmarks involved in healthy blood flow through the heart are denoted below in Figure 2.4.

2.4.1 Basics of Pulmonary Hypertension

Healthy, normotensive individuals typically have an mPAP between 12 – 16 mmHg, which is measured via RHC at the base of the PA; a PCWP, which is a surrogate measure for pulmonary venous pressure, between 2 – 14 mmHg, which is measured by guiding a catheter through the PA and towards the capillaries at the lung; and PVR less than 1 Wood Unit [33]. Similar to Ohm's Law, PVR (Equation 1) is defined as the relationship between the pressure gradient between the right heart and lungs and an individual's cardiac output. This indicator is defined as:

$$PVR = \frac{mPAP - PCWP}{CO} \tag{1}$$

where *mPAP* is the mean pulmonary artery pressure in mmHg, *PCWP* is the pulmonary capillary wedge pressure in mmHg, and *CO* is the cardiac output in L/min. PVR is usually given in Woods Units but can be multiplied by a factor of 80 to yield $\frac{\mathrm{dyn \cdot s}}{\mathrm{cm^5}}$.

Although there are other options for diagnosis, PH is determined often by RHC. This is an invasive procedure in which a physician guides a pressure catheter through a patient's vein (typically the femoral vein), into the heart, through the right atrium, and into the right ventricle. The catheter can then be inserted into the PA for determination of the patient's mPAP, and towards their pulmonary capillaries for measurement of the patient's PCWP. PVR can then be calculated using these invasively measured parameters, the individual's cardiac output, and the relationship shown in Equation 1. Although invasive, these hemodynamic measurements are extremely useful for accurately diagnosing PH and discriminating between PH types (pre-capillary PH, which is associated with elevated pressures in the pulmonary arteries before the lungs; post-capillary PH, which is associated with elevated pressures in the pulmonary veins carrying oxygenated blood back to the heart; and combined PH, which describes conditions belonging to both pre- and post-capillary PH) and groups (Groups 1 – 5). This discrimination is extremely important, as the treatments for Group 1 pre-capillary PH patients can be detrimental to individuals in other groups. The different PH groups are shown below in Table 2.1. Group 1 PH consists of individuals with pulmonary arterial hypertension or pre-capillary PH, Group 2 PH is PH due to left heart disease, Group 3 PH is PH due to lung diseases, Group 4 PH is caused by PA obstructions, and Group 5 PH is comprised of unclear and multifactorial cases of PH [34]. Most ESRD patients are classified as Group 5 PH since the exact mechanisms of development are not well known.

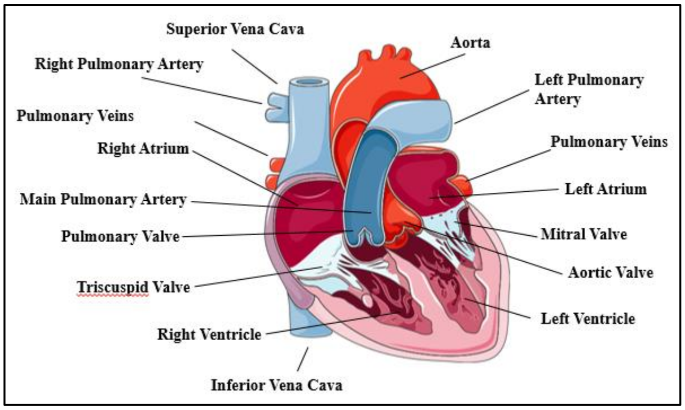

Figure 2.4. Basic anatomy of the heart and pulmonary vasculature.

This image was taken from Servier Medical Art by Les Laboratoires Servier under a Creative Commons License [8]. License available at: https://creativecommons.org/licenses/by/3.0/us/legalcode.

Table 2.1. Pulmonary hypertension classifications [34].

Definition	Clinical Determinants	Clinical Groups
Pre-Capillary PH	mPAP > 20 mmHg, PCWP ≤ 15 mmHg, PVR ≥ 3 Woods Units	1, 3 , 4, and 5
Isolated Post-Capillary PH	mPAP > 20 mmHg, PCWP > 15 mmHg, PVR < 3 Woods Units	2 and 5
Combined Pre- and Post-Capillary PH	mPAP > 20 mmHg, PCWP > 15 mmHg, PVR ≥ 3 Woods Units	2 and 5

2.5 Non-invasive Screening Techniques for Pulmonary Hypertension

This section includes an overview of non-invasive methods for screening and detecting pulmonary hypertension. Brief discussions of echocardiography, magnetic resonance imaging, and more novel techniques employing computational fluid dynamics are included. Applications of computational fluid dynamics models for modelling arteriovenous fistulas are also given.

2.5.1 Echocardiography

Since RHCs are invasive, non-invasive screening techniques, such as echocardiography, are recommended as the initial step for identifying incidences of PH [35]. Doppler echocardiography is widely accessible, provides useful information about direction and speed of blood flow, and can be used to assess and monitor right heart function. Systolic pulmonary artery pressure (sPAP) is estimated via transthoracic echocardiograms used to assess the backwards flow of blood from the right ventricle, through the tricuspid valve, and back into the right atrium [35]. This is referred to as tricuspid regurgitation (TR) and can be mathematically related to sPAP using a simplified form of the Bernoulli equation. This formula (Equation 2) is defined as:

$$sPAP = 4v_{tr}^2 \tag{2}$$

where v_{tr} is the maximum TR jet velocity identified by the sonographer. Due to errors in right atrial pressure estimation and poor imaging of the TR jet, it has been suggested that echocardiography may be inaccurate for estimating PA pressures [36]. Fisher et al. [36] found that echocardiography estimations of sPAP varied by more than ±10% compared to invasive measurements roughly 48% of the time. Additionally, the magnitude of pressure underestimation tended to be greater than overestimation [36]. Shujaat et al. [37] reported that transthoracic echocardiography was capable of identifying hypertensive patients, but had limited success when identifying normotensive patients since sPAP was consistently overestimated. Furthermore, it was later observed that differences between echocardiography estimated sPAP and RHC measurements increased in patients suffering from more extreme cases of TR and PH [38].

2.5.2 Three-Dimensional Magnetic Resonance Imaging

The adoption of cardiac magnetic resonance imaging (MRI) has been suggested as one possible route to more reliably estimate PA pressures and right ventricle function since it is currently one of the most accurate and repeatable non-invasive methods available for assessing cardiac structure and function [39], [40]. Johns et al. [39] conducted a retrospective analysis of patients suspected of having PH that had undergone RHC and MRI. Using parameters such as the angle of the interventricular septum, ventricular mass index, and the extent of blood flow in a black blood imaging technique, this group generated a regression equation for mPAP estimation with a sensitivity of 93% and a specificity of 79% when [39]. A study by Bane et al. [41] reported similar success when estimating mPAP using the ratio between end diastolic volume and ejection fraction in the right ventricle, and PCWP using the ratio between peak early diastolic mitral inflow velocity and peak early diastolic mitral annular velocity. Parameters obtained from MRI correctly identified all patients as having PH and were able to discriminate between pre-capillary PH and post-capillary PH 71% of the time [41]. Lungu et al. [42] studied 27 PH patients and 8 normotensive patients and found that MR images could be used to derive diagnostic indices based on one-dimensional pressure-wave equations or a three-element (RCR) Windkessel model. This group reported positive correlations between the ratio of the power of the reflected wave to that of the incident wave and the severity of PH. A comparable relationship was found for increased distal resistance in the pulmonary vasculature and PH severity [42]. Lungu et al. [42] found statistically significant differences in these parameters for normotensive patients, mild PH patients, and severe PH patients and concluded that this methodology could be used to further develop a non-invasive diagnostic test for patients suffering from PH. Another MR-based approach is the use of phase-contrast MRI scans to non-invasively determine blood flow rates and velocities. While this technique was found to have limited diagnostic ability by Schafer et al. [43], it may still be applied to help screen patients and may be refined by combining it with RHC to assess flow and vasculature resistance during catheterization.

2.5.3 Four-Dimensional Magnetic Resonance Imaging

A recent advancement in non-invasive imaging is the development of four-dimensional MRI. This imaging modality uses velocity data encoded from phase-contrast MRI to create time-dependent 3D velocity fields [44]. Work done by Driessen et al. [45] aimed to compare tricuspid regurgitation measured by 2D and 4D MRI in a total of 88 patients. This group found that 4D MRI was able to accurately assess tricuspid regurgitation and that 4D measurements correlated strongly (ICC = 0.910) with 2D measurements, offering evidence in support of 4D MRI for non-invasively screening PH patients. Other studies utilizing 4D MRI have reported decreased magnitudes of wall shear stress (WSS) in PH patients compared to healthy, normotensive patients [46], [47]. Schafer et al. [46] reported decreases in peak WSS as large as 40% in the main PAs of hypertensive patients, whereas Odagiri et al. [47] reported decreases of roughly 54% in peak WSS in the main PAs of pre-capillary PH patients when compared to healthy participants. Odagiri et al. [47] also reported increased vortex formation and the early onset of retrograde flow in pre-capillary PH patients. Conversely, Kheyfets et al. [48] reported that decreased vorticity in the main PA of PH patients correlated well (r = -0.73) with increasing PVR. An example of 4D MRI flow measurements in normotensive and PH patients can be seen below (Figure 2.5). It should be noted that in a separate study, Kheyfets et al. [49] enumerated several limitations of 4D MRI, some of which included excessively noisy signals, low spatial and temporal resolution, and a decreased ability to visualize patient-specific flow patterns compared to computational models of fluid flow.

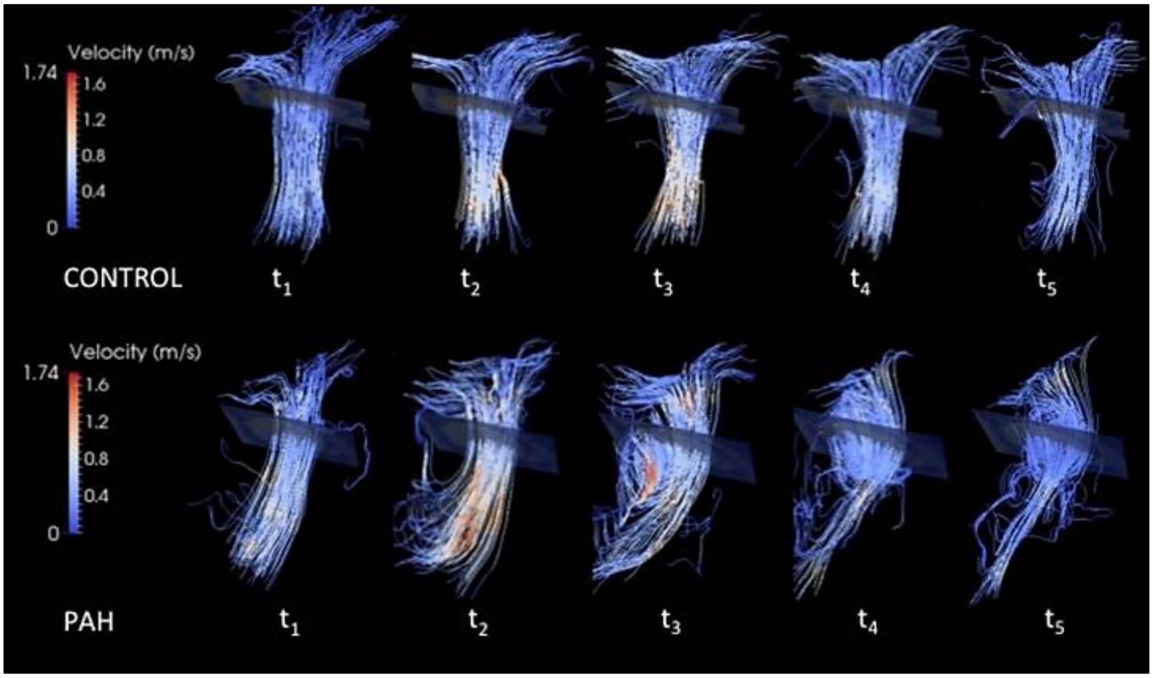

Figure 2.5. Velocity streamlines rendered with data from 4D MRI.

An example of velocity streamlines generated by 4D MRI in healthy (top) and pre-capillary PH (bottom) patients [48]. Reprinted with permission from John Wiley and Sons, *Journal of Magnetic Resonance Imaging*, Kheyfets et al. (2016). Copyright 2016, International Society for Magnetic Resonance in Medicine. No changes were made to this image.

2.5.4 Computational Modeling

Recent work has been done to develop computational methods to model blood flow, such as computational fluid dynamics (CFD), and vessel deformation due to blood flow, such as fluid-structure interaction (FSI) models. These models generally require a set of non-invasive CT or MR images to be acquired from a patient. These images are used to recreate the patient's anatomical geometry, which is then analyzed using software that approximates fluid and solid phenomena using an iterative approach.

2.5.4.1 Computational Fluid Dynamics

A novel technique for screening and detecting PH involves modeling blood flow through patient's PAs using computational fluid dynamics (CFD), which refers to computer software and algorithms that offer approximated numerical solutions to partially solved momentum and continuity equations. CFD software utilizes user-defined geometry, fluid properties, and boundary conditions to model continuous fluid flow with a series of partial differential equations. It then discretizes these partial differential equations into simplified algebraic equations, which are solved numerically [50]. Equation 3, given below, is derived from the conservation of mass, whereas Equations 4 is derived from Newton's second law and the conservation of momentum. Together, these equations are used by CFD software to model fluid flow and are defined as:

$$\frac{\partial(\rho)}{\partial t} + \nabla \cdot \left(\rho \vec{V}\right) = 0 \tag{3}$$

$$\rho\left[\frac{\partial\vec{V}}{\partial t}+\left(\vec{V}\cdot\nabla\right)\vec{V}\right]=-\nabla p+\nabla\cdot\bar{\bar{\tau}}+\rho\vec{f} \tag{4}$$

where ρ is density of the fluid, $\vec{V}$ is the velocity vector, p is the pressure, $\bar{\bar{\tau}}$ is the viscous stress tensor, and $\vec{f}$ is the body force per unit mass [51]. . After being converted into algebraic equations, these relationships are solved for a discrete number of points throughout a geometry, typically via the finite volume method [50]. CFD models belong to a more broad category of computational modelling and *in silico* simulations, which offer more affordable and timely information than many *in vitro* and *in vivo* experiments and display great potential for patient-specific medicine. The following sections cover the fundamentals of CFD, the general workflow for CFD projects, and existing models of PAs and AVFs.

2.5.4.2 Segmentation for CFD Analysis

CFD allows for fluid flow models to be created using a defined volume and series of inputs and boundary conditions. To obtain the volumes to be analyzed using CFD, non-invasive images acquired from MRI or computed tomography (CT) can be used. These medical scans, along with semi-automated meshing software such as Mimics, 3D Slicer, or ImageJ, can be used to recreate three-dimensional (3D) models of anatomy captured during imaging sessions through a process known as *segmentation*. Segmentation is defined as the process of extracting contiguous image slices from medical imaging to form a larger geometry that accurately replicates the anatomy of interest. This process usually consists of an initial “thresholding” phase to identify geometry and a subsequent “isolation” phase where the geometry is separated from the rest of the image [52]. During segmentation, each pixel in a medical scan is assigned a label based on user-defined criteria. This labeling allows pixels with the same labels to be connected and extracted, resulting in a patient-specific volume representative of an organ, blood vessel, or other anatomical structure [52]. Contrast-enhanced MR images obtained after the injection of gadolinium-based agents into the patient's circulatory system or CT images are preferred for improved model accuracy, but present risks associated with allergic reactions, mild toxicity, exposure to ionizing radiation, and damage to the kidneys respectively [53], [54]. Models created during segmentation are limited by the quality and resolution of the medical scans. Scans with thicker slices can result in the appearance of vessel discontinuities and the absence of smaller vasculature [53]. It is important that models analyzed for clinical purposes are created using scans containing an appropriate number of sufficiently thin slices with no distance between slices so that generated geometries are representative of realistic anatomical geometries.

2.5.4.3 Meshing for CFD Analysis

After 3D models of the anatomy of interest have been created using segmentation software, the models can be imported into a program, such as ANSYS Workbench, that discretizes the continuous model into a series of finite elements or volumes connected to each other at points known as nodes. This process of discretization, referred to as *meshing*, is necessary for further analysis since solutions to the continuity equation (Equation 3) and momentum equations (Equation 4) will be approximated for each element. For an accurate estimation of flow properties, it is important that the mesh is fine enough to capture important physical phenomenon such as fluid boundary layers and flow gradients [55]. For fluid modeling, it is more common to use the finite volume method to approximate continuous domains by breaking up the larger volume into a series of smaller control volumes. For solid modeling, the finite element method is used. This method involves discretizing the larger solid domain into a series of much smaller elements with their own mechanical properties. Meshes for fluid and solid domains are generated in similar ways when using commercial software such as ANSYS Workbench.

Meshes can be generated using tetrahedral, hexahedral, or polyhedral elements [56]. Past studies have shown that hexahedral meshes can be complicated to generate for PA models including multiple bifurcations [57]. Hexahedral meshes also make it difficult to locally refine mesh regions [58]. Typically, tetrahedral and polyhedral meshes are used to model fluid and an increase in mesh density near the walls of the model, known as *inflation*, can be used to provide researchers with a more accurate representation of fluid behavior at the walls. This is important for modeling the boundary layer of fluid flow so that wall shear stresses (WSS) be reliably estimated. It is also important for capturing fluid velocity and pressure so that wall deformation can be estimated during FSI modeling.

Two useful metrics for determining the quality of meshes constructed in ANSYS are skewness and orthogonal quality. Both skewness and orthogonal quality range between 0 and 1. Meshes of excellent quality are those where the average skewness ranges from 0 – 0.25 and the average orthogonal quality ranges from 0.95 – 1 [59]. While meshes can vary in quality, it is recommended that a mesh's skewness never exceed 0.95 and that a mesh's orthogonal quality never fall below 0.1 [59]. After a high-quality mesh has been generated, a mesh independence test should be conducted to ensure that the quality of the mesh does not affect the solutions of the model. This test should compare the difference between solutions obtained using meshes of varying densities to the solution realized using an exceptionally dense mesh assumed to yield the "true" solution [53]. Past work in this lab has utilized a mesh independence threshold of < 1% difference between solutions [60]. Once an acceptable mesh has been generated using the aforementioned techniques, it is ready to be imported into a software capable of approximating solutions to the partially solved momentum and continuity equations.

2.5.4.4 Boundary Conditions for CFD Analysis

Inlet and Outlet Boundary Conditions

Once the volume of interest has been discretized, inflow and outflow boundary conditions must be assigned to the model. These boundary conditions may consist of mass flow rates, fluid velocities, and inlet or outlet pressures. For patient-specific CFD models, inlet boundary conditions are usually prescribed based on clinically measured volumetric flow rate waveforms. These waveforms can be converted into mass flow rate waveforms and velocity waveforms that span multiple cardiac cycles [61]. The most physiologically accurate inlet boundary conditions are provided through invasive catheterization capable of providing volumetric flow rates and pressure measurements; however, echocardiography and phase-contrast MRI can both be used to obtain velocity waveform measurements as well [53]. Outlet boundary conditions typically utilized for patient-specific CFD models include pressure outlets, mass flow rate outlets, and outflow boundary conditions based on model geometry. When using zero traction outlet conditions, the pressure of each outlet is set to a constant value [62]. This is a common approach but can result in non-physiological flow since the flow split is governed entirely by the segmented geometry when downstream resistance is not considered [63]. Outflow boundary conditions can also be assigned based on a vessel resistance value corresponding to the cross-sectional area of the outlet, the flow split between outlets, and pressure values [64]. This technique requires measurements offering insight into the outlet flow split, which can be determined by non-invasive imaging or catheterization, and the outlet pressure value, which must either be assumed, estimated by a non-invasive imaging modality, or measured invasively by catheterization [64]. A slightly more complex method for defining outflow boundary conditions in patient-specific CFD models is the use of a three-element Windkessel model accounting for resistance and compliance of the distal vasculature [65], [66]. This model relates the outlet pressure to upstream vessel resistance, downstream vessel resistance, and downstream vessel compliance [67].

Fluid Properties

Before a solution can be approximated, the properties of the fluid filling the model's volume must be assigned. Most studies modeling blood flow assume the fluid to be incompressible and Newtonian, assigning blood a density of 1050 or 1060 kg/m^3 and a dynamic viscosity of approximately 0.0035 kg/m.s. These assumptions are inaccurate since blood is a compressible and non-Newtonian fluid, but the effects of these properties often are negligible and are much more computationally expensive. Studies using non-Newtonian properties, like the study discussed in this document, must define parameters such as the viscosity of the fluid at zero shear, viscosity of the fluid at infinite shear, the shear rate, and a time constant. Cho and Kensey [68] discussed several different models for non-Newtonian fluid behavior in their seminal 1991 paper. This study compared abilities of different non-Newtonian fluid to predict fluid viscosity at different shear rates. The Carreau model, which is used commonly in computational studies to model blood viscosity, was defined as having the following properties: time constant (λ) = 3.313 s, empirical exponent coefficient (n) = 0.3568, zero-shear viscosity (μ_o) = 0.56 Poise, and infinite shear viscosity (μ_∞) = 0.0345 Poise

2.5.4.5 Wall Boundary Conditions for FSI Analysis

Traditionally, walls encapsulating the fluid are assumed to be rigid, meaning they do not deform when stressed, and are assumed to have no-slip conditions, meaning the fluid at the boundary layer has a zero magnitude velocity relative to the wall or boundary. These assumptions are nearly ubiquitous in CFD models of blood flow; however, there has been a recent shift towards the inclusion of fluid-structure interaction (FSI) models in studies with clinical relevance since rigid wall assumptions have been found to globally overestimate WSS [69], [70]. FSI models forego the rigid wall assumption and attempt to model the deformation of the fluid's boundary – in this case, the vessel wall – with some sort of linear elastic modulus or hyperelastic relationship. One of these hyperelastic relationships is the 3rd order Yeoh model, which has been shown to accurately predict deformation at both small and large strains and is defined by three constants often determined through mechanical testing and curve fitting [67], [71], [72]. The addition of this component into CFD models can provide more accurate and realistic insight into the mechanical stresses experienced by the vasculature of interest. Since these mechanical stresses can be used to predict AVF failure and maturation [73]–[75], distinguish between normotensive and PH patients [46], [47], [64], and ultimately are what lead to vascular remodeling, it is critical that they are characterized and approximated as effectively as possible. It should be noted that FSI analysis is not merely another option in CFD software, such as FLUENT, but is its own analysis requiring its own mesh, geometry, and boundary conditions.

Similar to the meshing process for fluid volumes, the wall or boundary layer must be assigned a specific thickness and must then be discretized into a finite number of elements. The deformation and movement of these minute elements is usually the main parameter of interest during FSI analysis and requires three boundary considerations: (1) the amount of slip at the wall or interaction; (2) perivascular pressure, or the pressure acting on the outer surface of the vessel; and (3) the degree of freedom of movement for nodes located within the solid domain [53], [76]. As previously stated, most models assume no-slip conditions at the interface of the fluid and wall. Perivascular pressure is generally considered to be spatially uniform and can be estimated via image-based relative area change measurements taken during catheterization *or* assumed to be equivalent to atmospheric [77]. Finally, it must be specified whether nodes of the vessel wall can translate or rotate. The faces of the solid domain must be given boundary conditions similar to fluid modeling; for solid modeling, however, these inlets and outlets can be fixed, prescribed rollers to allow one-dimensional movement, assigned spring values to allow restricted motion, or left free to rotate and translate. Approximated solutions for the solid domain are made using the principles of impulse conservation [78].

Fluid and structure dynamics may be solved monolithically by relating all fluid and structure equations in a single matrix or by a partitioned approach in which equations of each respective system are solved separately and then combined iteratively [79]. Using a partitioned approach, the fluid dynamics calculations and structure dynamics may be coupled in one of two ways (Figure 2.6). *One-way coupling* allows for only the pressure exerted by the fluid domain to be transferred to the solid domain, whereas *two-way coupling* allows for the deformation of the solid domain to be transferred back to the fluid domain; thus, two-way coupling allows for the determination of secondary flow patterns based on the resultant behavior of the solid domain [78]. While two-way coupling is more computationally expensive than one-way coupling and constantly alters mesh quality for both domains, it offers greater insight into the overall behavior of the fluid. In vasculature that is stiff and hardened, the deformation of the solid domain may be negligible and one-way coupling may be adequate for modelling [53]. Models of highly deformable vessels, such as enlarged AVFs, may require two-way coupling for more accurate visualizations of blood flow [67], [77].

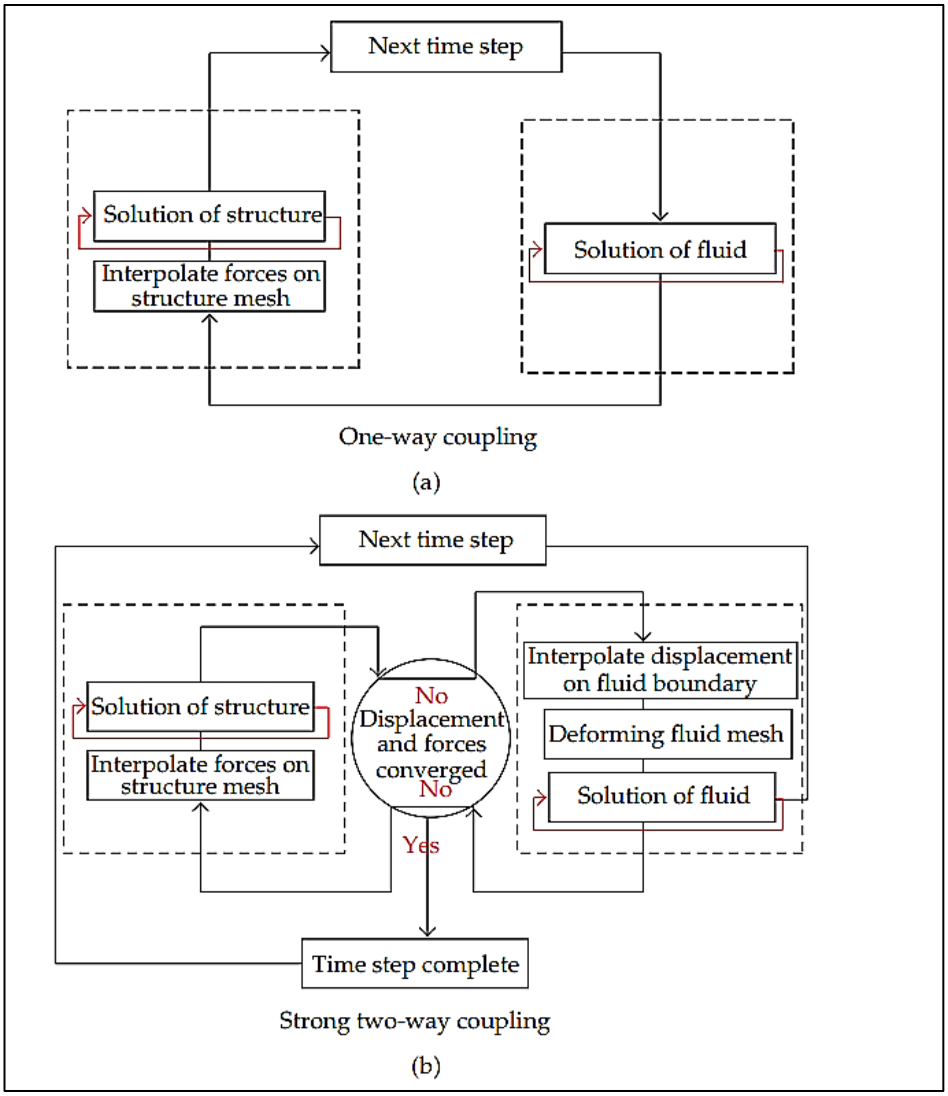

Figure 2.6. One-way vs. two-coupling methods for FSI analysis.

Comparison of one-way and two-coupling methods for FSI analysis [78]**. Original image published by Benra et al. (2011) in the *Journal of Applied Mathematics* under a Creative Commons Attributions License. No changes were made to this image. License available at: https://creativecommons.org/licenses/by/3.0/us/legalcode.**

2.5.4.6 Solver Preferences for CFD Analysis

In addition to the inputs discussed in the preceding sections, there are a few miscellaneous solver preferences that should be mentioned. The first preference involves the selection of a pressure- or density-based solver. Pressure-based solvers are typically used for incompressible flow and are used for blood flow models assuming that blood is an incompressible fluid [80]. Another preference that must be selected is the algorithm used for pressure-velocity coupling. Users have the option of selecting multiple solvers, two of which are the SIMPLE (Semi-Implicit Method for Pressure Linked Equations) algorithm and the PISO (Pressure Implicit with Split Operator) algorithm [81], [82]. Users must then select the number of iterations that the simulation will undergo. A sufficiently large number of iterations must be selected to allow the simulation to converge. During CFD analysis, a converged solution is a solution that has reached a specified threshold for tolerable error. This threshold is often defined by the scaled residual values existing within each finite control volume [83]. These residual values represent the local imbalances in each discretized equation for each control volume in the model. A root-mean-square residual level of 1×10^{-4} is the default residual option and is considered to be loosely converged. A residual level of 1×10^{-5} is considered well converged and a residual level of 1×10^{-6} is said to be tightly converged [83]. Residual levels are most commonly monitored for the continuity equation and momentum in the *x*, *y*, and *z* directions.

2.5.4.7 Post-Processing and Parameters of Interest for CFD Analysis

Blood flowing within vessels places stress on vessel walls and the endothelial cells lining the lumen of the vessels. This stress is categorized into two different types. The first stress is circumferential stress due to the pulse pressure within the vessel. The second stress, which is created by the tangential force of flowing fluid, is shear stress or wall shear stress (WSS) [84]. For generalized Newtonian fluids, WSS, one of the most commonly studied parameters in CFD analyses, can be calculated by using Equation 5 defined as:

$$\tau = \mu_{eff}(\dot{\gamma})\dot{\gamma} \tag{5}$$

where τ is WSS, μ_{eff} is the fluid's kinematic viscosity as a function of the shear rate, and $\dot{\gamma}$ is the shear rate [53], [84], [85]. Since endothelial cells align themselves with the direction of blood flow, significant changes in WSS magnitudes can promote vascular remodeling that has been directly correlated with increased cell proliferation and apoptosis [53]. Elevated WSS can lead to increases in the thickness of the vessel wall [86], whereas decreased WSS is frequently accompanied by turbulent flow, regions of blood circulation, and vortex formation [47], [87]–[91]. WSS, turbulent flow, vortex formation, abnormal pressure gradients, and unusually small or large fluid velocities are all hemodynamic properties that can be visualized through CFD analysis. Additionally, since many of these parameters are able to be non-invasively estimated in clinical settings by MRI and echocardiography, connections between these properties in fistulas and PAs of ESRD patients may offer physicians more effective metrics for monitoring AVF function and maturation so that pre-capillary PH development can be prevented when possible.

2.5.4.8 General Limitations of Computational Models and Analyses

Given that CFD and FSI analysis are both computational approaches to modelling physical phenomena, there are certain inherent errors and limitations associated with these techniques [92]. These methods do not provide closed form solutions where an exact answer is reached; instead, CFD models offer numerical approximations of the phenomena being modelled. The numerical approximations are all based on a series of initial assumptions made by the user. Patient-specific geometries have helped to promote more reliable and clinically relevant models but are still limited by the spatial resolution of imaging machines [93]. Similarly, patient-specific boundary conditions for CFD analysis are helpful for promoting accurate models but are often limited by a lack of knowledge about the mechanical properties of surrounding vasculature if an FSI analysis is included. Furthermore, these models only provide information about a limited window of time and do not currently present any utility for the continuous monitoring of physiological conditions. The computational power required to run these simulations is another limitation. Many models include inaccurate assumptions that allow for simplification so they can be conducted on computers with limited processing and storage capabilities. It is critical to address these limitations when one is performing a CFD analysis, provide convincing evidence in support of all assumptions, and seek model validation and verification when possible to ensure that the model is as accurate and reliable as possible.

2.5.4.9 Existing Models of Pulmonary Vasculature

Several groups have presented CFD models of pulmonary vasculature in both normotensive and PH patients using the processes outlined in earlier sections. Tang et al. [94] was one of the earlier groups to utilize CFD in an attempt to analyze hemodynamics in the PA. Using phase-contrast MR angiography scans from a group of six healthy participants, Tang et al. [94], who sought to quantify effects of exercise on PA hemodynamics, recreated proximal and distal portions of each patient’s PA using a custom segmentation algorithm. These models were then meshed using MeshSim software and a mesh independence test was conducted using each model’s mean WSS value and an independence threshold of 1.3% [94]. A patient-specific periodic flow waveform was assigned as the inlet boundary condition on the face of the main PA. Outlet boundary conditions were assigned based on a calculated resistance value derived from the cross-sectional area of the outlet, the left/right PA flow split determined by phase-contrast MRI, and an assumed healthy PCWP of 12 mmHg [94]. The walls of this model were assumed to be rigid and no-slip conditions were applied. The models had an average size of 1.5 million tetrahedral elements and modeled flow over four cardiac cycles. To simulate exercise, Tang et al. [94] assumed a doubled volumetric flow rate at the main PA and a 50% decrease in cardiac cycle time. Based on these assumptions, this group found increased WSS and a 60% reduction in the oscillatory WSS index (OSI) under simulated exercise conditions when compared to resting conditions. These results are partially depicted in Figure 2.7 and were used as the foundation for a follow-up study by the same group [64].

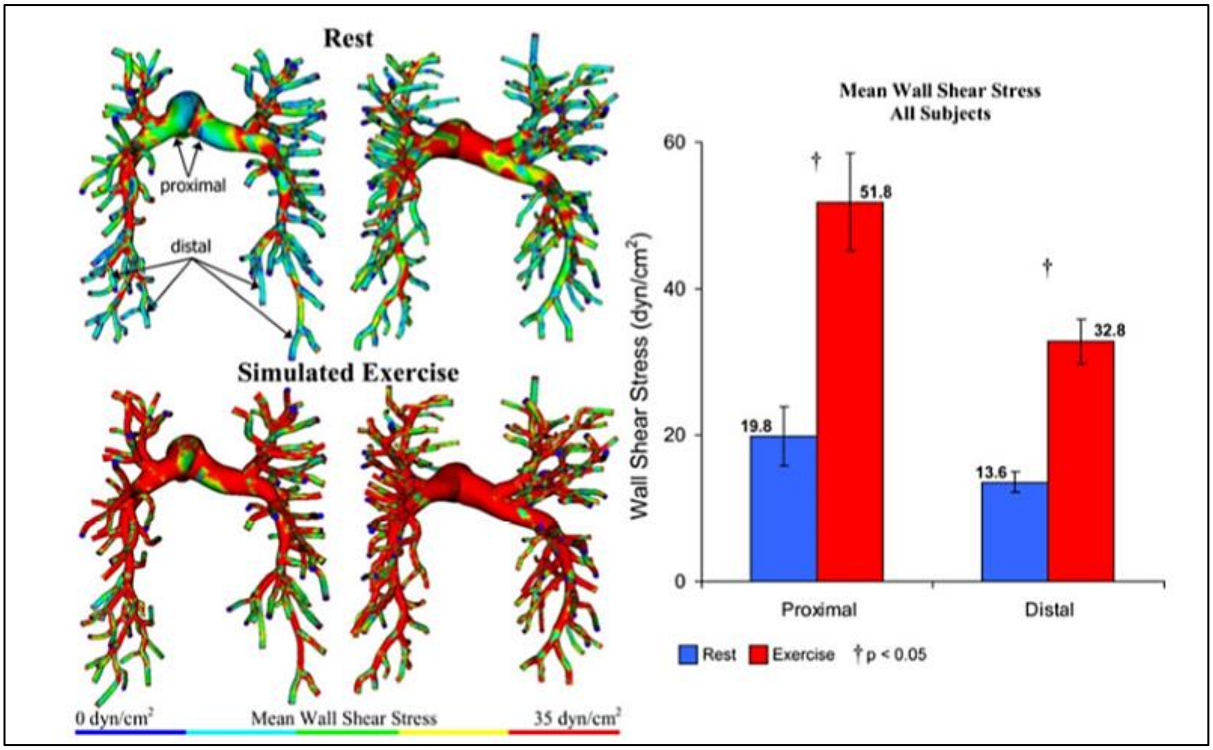

Figure 2.7. Mean pulmonary artery WSS during resting and simulated exercise.

Mean pulmonary artery WSS during resting and simulated exercise conditions [94]**. Reprinted by permission from Springer Nature: Springer, Annals of Biomedical Engineering,** ***Three-Dimensional Hemodynamics in the Human Pulmonary Arteries Under Resting and Exercise Conditions*** **by Tang et al. (2011). Copyright 2010, Published 2011. No changes were made to this image.**

In this follow-up study, Tang et al. [64] utilized an identical methodology as their earlier study to better quantify differences between pre-capillary PH and normotensive patients. Using five pre-capillary PH and five normotensive patients, models of pulmonary vasculature with an average size of 1.2 million tetrahedral elements were generated and analyzed using patient-specific properties similar to those utilized in this group's earlier 2011 study [94]. It was reported that pre-capillary PH patients have larger main, right, and left PA cross-sectional diameters, decreased cardiac outputs (3.7 ± 1.2 vs. 5.8 ± 0.6 L/min), and decreased WSS (4.3 ± 2.8 vs. 20.5 ± 4.0 dynes/cm^2) in their main PAs [64]. The authors concluded that since biomechanical factors like WSS directly impact endothelial health and function, these decreased levels of velocity (Figure 2.8) and WSS could play an important role in the progression of pre-capillary PH and, in the future, be used as a non-invasive parameter for screening and diagnosing hypertensive patients [64].

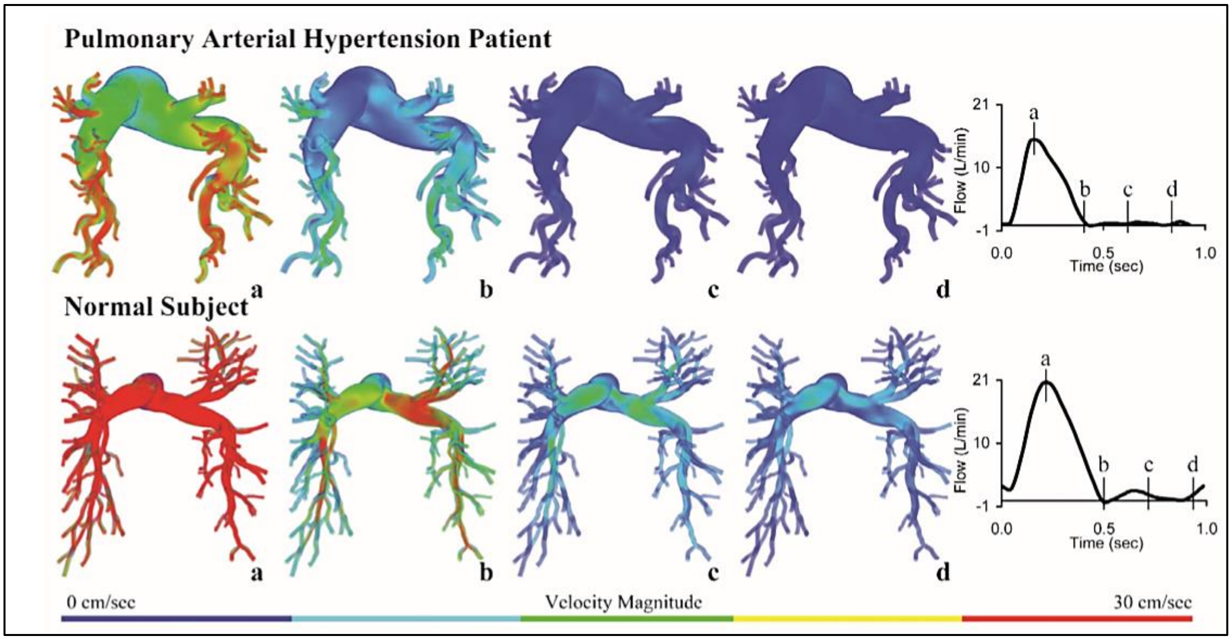

Figure 2.8. Volume-rendered velocity magnitudes in PH and normotensive patients.

Volume-rendered velocity magnitudes demonstrating the hemodynamic differences in pre-capillary PH patients (top) and normotensive patients (bottom) [64]**. Permission granted for republishing in a thesis/dissertation by SAGE Publications. Original image published by Tang et al. (2012) in *Pulmonary Circulation*. Copyright 2012. No changes were made to this image**.

Rabidou and George [60] corroborated these findings in a 2017 study comparing pre-capillary PH hemodynamics to normotensive hemodynamics. MR images were segmented and meshed in Mimics to create patient-specific three-dimensional models of PA anatomy. Models (3 pre-capillary PH, 1 normotensive) were then discretized into approximately 1.3 million tetrahedral elements, a number comparable to those used in earlier studies published by Tang et al. [64], [94]. Mesh density was increased at the walls using an inflation rate between 1.0 and 1.5 and a mesh independence test was conducted until differences in WSS fell below 1%; this independence threshold is just slightly lower than that used by Tang et al. [94]. Blood was assumed to be incompressible and Newtonian, and standard viscosity and density values were applied to the fluid model. The walls of the model were assumed to be rigid and to have no-slip conditions. Much like earlier studies, patient-specific inlet boundary conditions were applied using a user-defined function (UDF) meant to simulate three cardiac cycles and a blunt flow velocity profile representative of a full cardiac cycle [60]. All models were validated using MR-based velocity data and similar decreases in WSS were observed in PH patients. Rabidou and George [60] reported a maximum WSS of 5.57 dyn/cm^2 for their normotensive patient and 3.15 dyn/cm^2, 1.60 dyn/cm^2, and 1.52 dyn/cm^2 for their three pre-capillary PH patients. Not only was this decreased WSS magnitude (demonstrated in Figure 2.9) and decreased time-averaged WSS (TAWSS) similar to those reported in other computational studies [64], it was also comparable to decreases reported by some studies using 4D MRI to calculate WSS [47], [48].

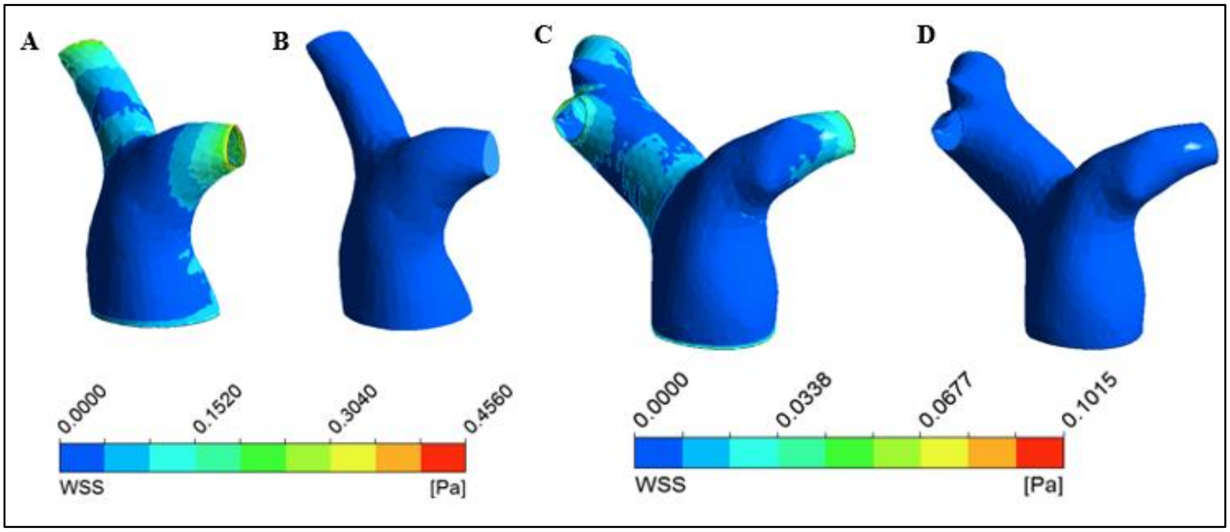

Figure 2.9. CFD models of PA hemodynamics in normotensive and hypertensive patients [60]**.**

CFD models created by Rabidou and George [60]**. (A) WSS at peak systole in a normotensive patients, (B) WSS during diastole in a normotensive patient, (C) WSS at peak systole in a hypertensive patient, and (D) WSS during diastole in a hypertensive patient.**

In 2015, Kheyfets et al. [49] sought to develop methods for non-invasively estimating PVR in 10 adult PH patients using CFD. CT scans were imported into Mimics for vasculature segmentation. All models were then subsequently meshed in ICEM-CFD using tetrahedral elements with a maximum allowable edge length of 0.84 mm that grew progressively in size from the endothelium surface to the volume core [49]. The fluid was assumed to be Newtonian and incompressible and standard density and viscosity values were assigned. Three simulations – each using its own unique set of inlet and outlet boundary conditions – were run for each model. The first simulation used a constant volumetric flow rate (90 cm^3/s) and a zero-traction outlet boundary condition. The second simulation used a patient-specific inlet flow rate determined from RHC measurements and, similar to the first model, a zero-traction outlet boundary condition. Finally, the third model used a patient-specific inlet flow rate determined via RHC and a structured tree outlet boundary condition [49]. In order to limit the effects of image resolution on model results, this group utilized a parameter referred to as spatially averaged WSS, calculated by integrating the WSS over the entire discretized lumen and dividing by the total surface area of the model wall as shown below in Equation 6:

$$SAWSS = \frac{1}{A}\int_{A} WSSdA \tag{6}$$

where $SAWSS$ is spatially averaged WSS and A is the total surface area of the model's walls [49]. When using patient-specific velocity inlets and a structured tree outlet boundary condition, this group found that spatially averaged WSS correlated well with invasive PVR measurements (R^2 = 0.77) and arterial compliance (R^2 = 0.63). Spatially averaged WSS, which the authors claimed was a metric independent of image resolution, could be used by other studies dealing with suboptimal MR or CT image resolutions [49].

In a later case study by a similar group, Kong et al. [95] employed both spatially averaged WSS and an FSI simulation into a single PA model. Images obtained during a CT scan of a healthy 19-year-old subject were used to reconstruct a model of the patient's PA that included incompressible Navier-Stokes equations governing fluid flow and a non-linear elasticity equation for the wall mechanics. This group assumed a constant arterial wall thickness of 1 mm, a fluid viscosity of 0.03 g/cm.s, a fluid density of 1 g/cm^3, a wall modulus (E) of 4×10^6 g/cm.s^2, a Poisson's ratio (υ) of 0.42, and a density of 1.2 g/cm^3 [95]. A velocity profile was derived from a given inflow rate and all outlets were assumed to be traction-free. While this study did not present any findings of clinical relevance, there were two main points mentioned that should be considered in future work. Although fairly obvious, the first observation made by Kong et al. [95] was that WSS magnitudes and pressure gradients were directly correlated with the velocity inlet conditions. This observation supports the inclusion of patient-specific inlet conditions when possible. The second observation made by this group was that the proximal PA vasculature undergoes increased displacement compared to the more distal vasculature (Figure 2.10). It should also be noted that during peak simulated systole, the maximum deformation of the PA wall was roughly 2 mm [95]. Since this study was only focused on presenting methodology for the development of a monolithically-coupled FSI model of a patient's PA, it did not compare the effects of the inclusion of an FSI on clinically useful metrics like WSS, fluid velocity, or pressure gradients. It is currently unclear whether the walls of a PA should be modeled in both normotensive and hypertensive patients and to what extent vascular hardening effects pulmonary hemodynamics and wall mechanics; however, it has been shown that PAs are deformable, so this is an inclusion that must be considered and acknowledged by future work [96]. A similar study was also done by Zambrano et al. [97], where the vessel walls of a normotensive patient were assigned a linear elastic modulus of 1.5 MPa and a hypertensive patient was assigned a modulus of 2.0 MPa.

The studies presented in this section (Table 2.2) offer clear evidence supporting the adoption of hemodynamic properties for screening and identifying pre-capillary PH patients from normotensive patients. By simulating blood flow in patient-specific PA geometries, Tang et al. [64] and Rabidou and George [60] both found decreased blood flow velocities and levels of WSS in the PAs of pre-capillary PH patients. Additionally, Tang et al. [64] reported that pre-capillary PH patient's PAs have larger cross-sectional diameters and that this population suffered from significantly decreased CO when compared to healthy normotensive patients. These findings are all in agreement with existing literature [46], [47], [98]–[101]. An FSI analysis of a single patient's PA was performed by Kong et al. [95], who found that the proximal PA undergoes much more deformation than distal pulmonary vasculature; unfortunately, the effects of including an FSI analysis in models of PA hemodynamics were not explicitly stated in this study. Further work is needed to better quantify the effects of including or excluding FSI analyses in models of pulmonary blood flow. There is also a lack of literature examining PA hemodynamics (specifically metrics like blood flow velocity, WSS, and WSS gradients) in ESRD patients. If similar decreases in WSS or velocity are present in ESRD patients undergoing dialysis via AVFs, it may be possible to correlate those properties with fistula hemodynamics. This correlation will allow physicians to better predict fistula outcomes and intervene during AVF development to limit the development of pre-capillary PH in this population.

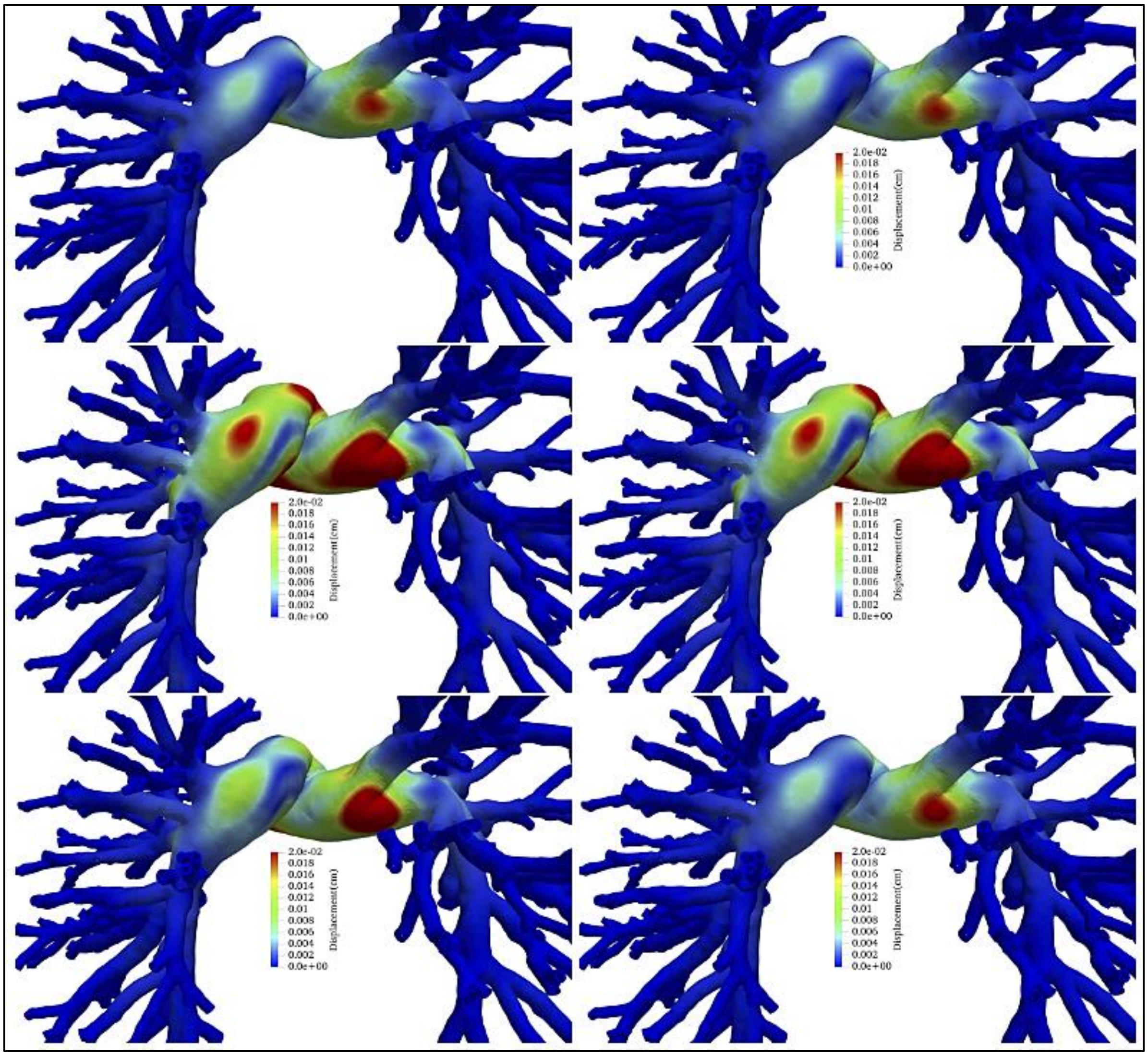

Figure 2.10. Simulated pulmonary artery deformation throughout a cardiac cycle.

(Top left) The undeformed pulmonary artery [95]**. Deformation of the arterial wall at the start of a patient-specific cardiac cycle (top right), 25% into a cardiac cycle (middle left), 33% into a cardiac cycle (middle right), 50% seconds into a cardiac cycle (bottom left), and at the conclusion of a cardiac cycle (bottom right). Reprinted with permission from John Wiley and Sons. Original image published by Kong et al. (2019) under a Creative Commons License. License available at: https://creativecommons.org/licenses/by/3.0/us/legalcode. No changes were made to this image.**

Table 2.2. Summary of Pulmonary Artery Models.

Group	Year	CFD or FSI?	Relevant Contribution
Tang et al. [94]	2011	CFD	Protocol for modelling PAs
Tang et al. [64]	2012	CFD	Increased cross-sectional area, decreased CO, decreased WSS in PH
Kheyfets et al. [49]	2015	CFD	Method for estimating PVR, Explanation of SAWSS
Rabidou and George [60]	2017	CFD	Decreased velocity and WSS in PH
Kong et al. [95]	2018	FSI	Protocol for FSI analysis of PA, Main PA undergoes more deformation than distal vasculature
Zambrano et al. [97]	2018	FSI	Protocol for FSI analysis of PA, relevant mechanical properties

2.5.4.10 Existing Models of Arteriovenous Fistulas

Computational fluid dynamics has been used extensively to model both idealized and anatomically realistic AVFs. This modelling has been done primarily using information from human patients, but some groups have incorporated information from animal models into their simulations. One such group is Pike et al. [102], who created CFD models of AVF blood flow in two murine models. Using ImageJ to reconstruct images acquired during 2D time-of-flight MR angiography and ICEM software to generate a mesh made of tetrahedral elements, models were made with an average of 1.5 million elements that had an average length of 0.37 µm [102]. MR-based velocity data was used to assign cross-sectional average blood flow velocity values for the arterial inlet and venous outlet of the recreated AVF. The arterial outlet boundary condition was set to zero stress. Standard blood density and viscosity values were assigned to the fluid, walls were assumed to be rigid, and no-slip conditions were applied. A mesh and time-step independence test were conducted using an independence threshold of 5% and residual levels were set to 10^{-5} [102]. Pike et al. [102] observed an average increase of 15% in the cross-sectional area of the AVF vein, which also experienced elevated levels of WSS, WSS gradients, and oscillating WSS indices compared to a jugular vein in a control mouse model (Figure 2.11). Additionally, this group reported increased levels of both blood recirculation and vortex formation in AVF veins, two parameters that previous work had linked to atherosclerosis and neointimal hyperplasia in AVFs [103]–[105].

Using MR images collected from a single human participant, a similar study was conducted by Bozzetto et al. [106]. AVF geometry was recreated using the Vascular Modelling Toolkit package from Orobix and discretized using meshing software from the OpenFOAM 4 software suite. Volumetric flow waveforms were extracted from MR scans and prescribed as boundary conditions at the proximal artery (inlet) and distal artery (outlet). The proximal vein (outlet) was assigned a zero traction boundary condition [106]. Similar to Pike et al. [102], no FSI analysis was done in this study; the walls were assumed rigid and no-slip conditions were applied. Interestingly enough, blood was assumed to be non-Newtonian and was modeled using the Bird-Carreau equation. Three cardiac cycles were modeled and results from the final cycle were used for analysis to avoid effects of start-up transients. Bozzetto et al. [106] observed transitional laminar to turbulent flow developing in the anastomotic vein and concluded their article by suggesting this technique was a valid option for clinics to visualize flow and monitor regions of vascular access.

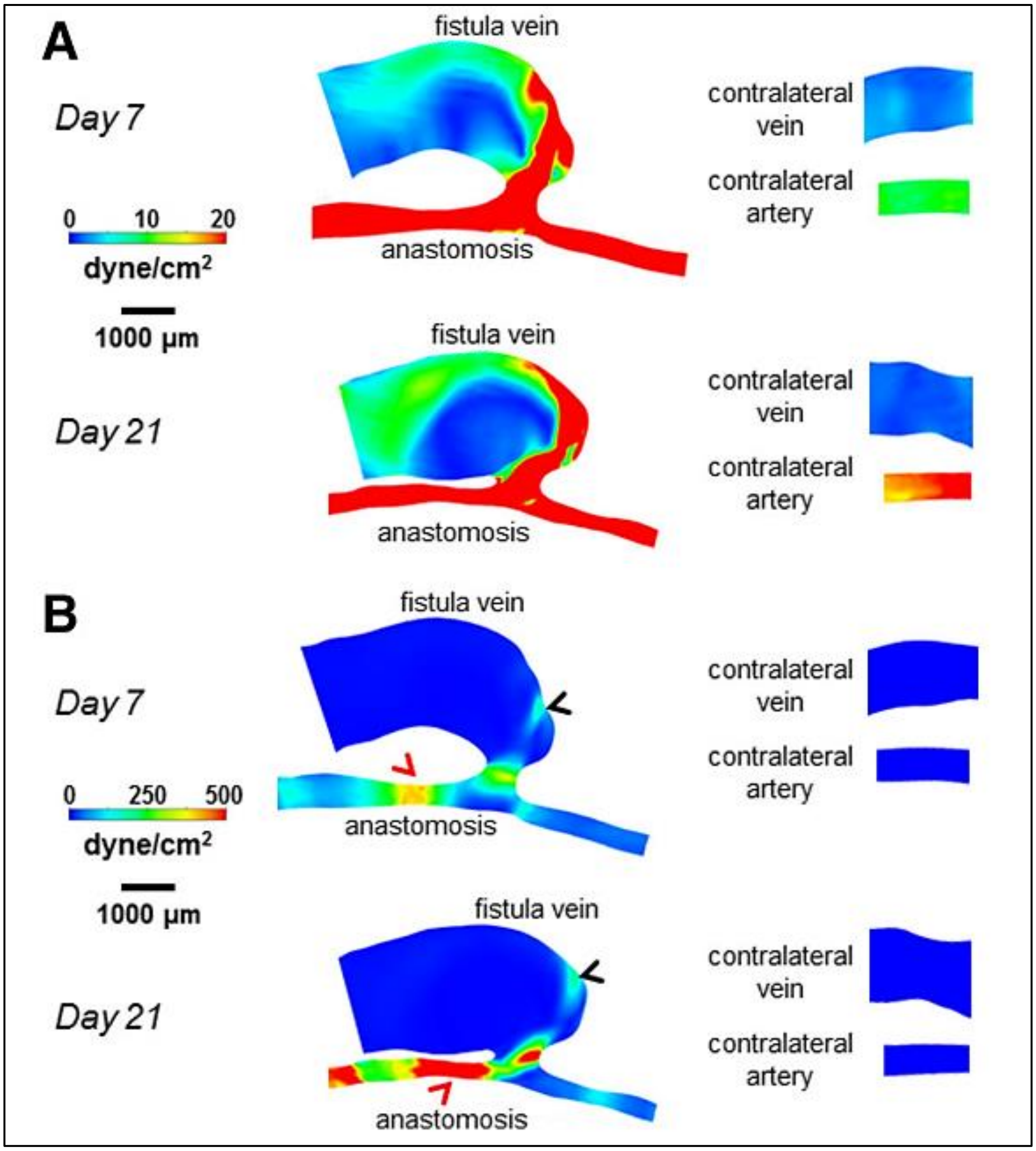

Figure 2.11. WSS in mouse AVFs.

WSS color maps for the two AVF murine models (left) and control vasculature (right) [102]**. The increase in the cross-sectional area of the AVF vein in both models should be noted. Original image published by Pike et al. (2017) in *Theoretical Biology and Medical Modelling* under a Creative Commons Attribution 4.0 International License. No changes were made to this image. License available at:** **https://creativecommons.org/licenses/by/4.0/legalcode.**

Eventual AVF failure, typically due to neointimal hyperplasia or stenosis, is thought to be associated with complex hemodynamics in the venous segment of the AVF [102]–[105]. Carroll et al. [74] sought to offer more quantitative evidence in support of this claim in their 2010 study. MRI was done on healthy vein geometry and a fully mature, fully functional radiocephalic AVF. Three-dimensional models of the vasculature were recreated in Mimics and meshed in Gambit. The model of the control vein was created with an unstructured grid containing 583,000 elements, whereas the AVF model was meshed with a multi-block structured hexahedral grid composed of 1.64 million elements [74]. Both models underwent a mesh independence test using WSS as the monitored parameter and an independence threshold of 2%. While most other studies utilized MR data to create patient-specific inlet boundary conditions, Carroll et al. [74] used flow waveforms obtained from echocardiography, which has been shown to have good agreement with flow rate information from phase-contract MRI [107], to provide inlet conditions for each model's arterial inlet. The modelled fluid was assumed to be Newtonian, incompressible, and homogenous and pulsatile flow was simulated for a single cardiac cycle. It was found that the mean WSS in the AVF was 3.31 Pa, which was notably larger than the healthy vein's mean WSS of 0.14 Pa. Much like results reported by Pike et al. [102], an increase in the AVF's cross-sectional area was also observed. Carroll et al. [74] also reported excessively high WSS gradients more than 100 times greater than the 80 Pa/m threshold reported in earlier studies that linked increased WSS gradients to impaired endothelial function and pathological changes in local vasculature [108], [109].

In a similar 2013 study, Sigovan et al. [110] used MRI to recreate CFD models for three patients requiring surgical fistula creation. Unstructured meshes with a nominal resolution of 0.3 mm and an average mesh size of 250,000 elements were created in Hypermesh and tested for independence using average wall shear stress and a threshold of 5%. Fluid velocity and a mass flow rate were used as inlet boundary conditions. At the distal artery outlet and the proximal vein outlet, targeted mass flow rate was used as a boundary condition. Walls were assumed to be rigid and no-slip conditions were specified. Pulsatile flow simulations based on MR data were done for three cardiac cycles at three distinct points in time for each patient: (1) within five days of AVF creation, (2) one month after AVF creation, and (3) three months after AVF creation [110]. After the three-month time interval, this group reported that, in the venous segment of the AVF, Patient 1 (Figure 2.12) exhibited a 71% decrease in mean WSS, Patient 2 underwent a 78% decrease, and Patient 3 actually experienced a 2% *increase* in mean WSS levels; however, Patient 3's kidney remained functional at a high enough level where dialysis via an AVF was not required. This group concluded that blood flow rates through a patient's AVF change most notably during the first month following AVF creation and then leveled off, suggesting potential for flow measurements taken 4-8 weeks after creation to be used for AVF outcome prediction. If connections between AVF flow rates and the development of PH are found in future work, these results imply physicians could know whether AVFs require preventative measures or further surgical intervention as early as one month after they are created. Additionally, Sigovan et al. [110] observed levels of recirculation in low-WSS regions. This particular finding is in agreement with those reported by Pike et al. [102] and Bozzetto et al. [106] and may be used to monitor fistulas suspected of stenosis development.

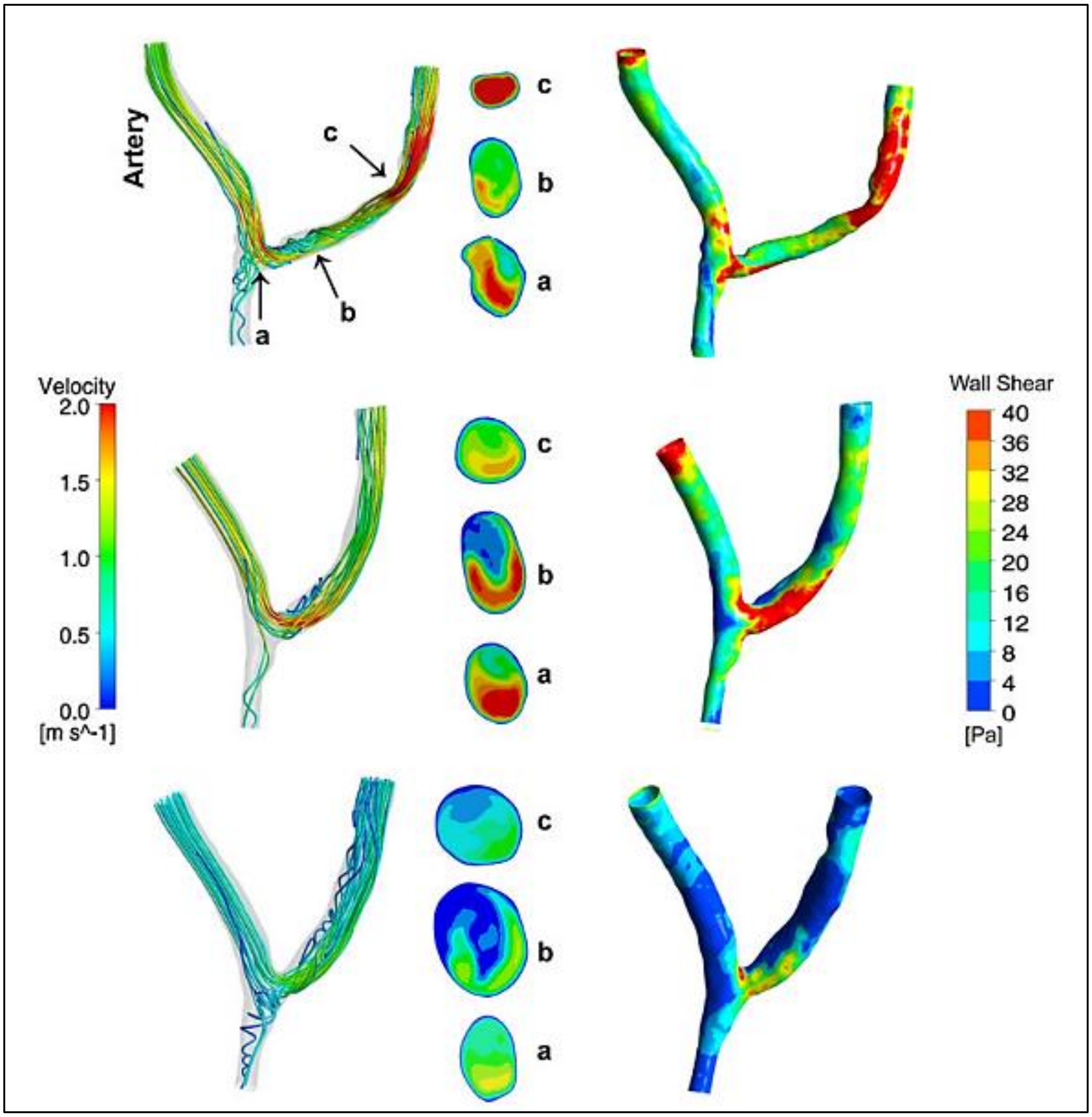

Figure 2.12. Decreasing WSS in AVFs post-creation.

The surgically created AVF in Patient 1 from Sigovan et al.'s 2013 study [110]**. (Top) AVF within five days of creation. (Middle) AVF one month after creation. (Bottom) AVF three months after creation. Reprinted by permission from Springer Nature: Springer, *Annals of Biomedical Engineering*, Sigovan et al. (2013). Copyright 2012, Published 2013. No changes were made to this image.**

None of the preceding studies included effects of wall deformation in their studies. Decorato et al. [77] presented a case study of an FSI analysis on a mature radiocephalic fistula using images acquired during CT-scan angiography. A hybrid mesh made of prismatic cells in the boundary layer and tetrahedral cells in the vessel core was used to discretize the fluid domain. The solid domain was modelled as a single layer of discrete-Kirchoff theory-based shell finite elements with varying thicknesses based on whether they were located in the arterial (1/10th of inlet diameter or 0.6 mm) or venous (0.4 mm) segment of the AVF [77]. A maximum mesh element size of 4×10^{-3} mm corresponded to an error less than 1% for the magnitude of the maximum velocity and WSS, resulting in a fluid mesh composed of 784,000 elements and a solid mesh composed of 89,000 elements. Blood was modelled as an isotropic, homogenous, non-Newtonian fluid that followed the Casson model and wall elasticity was modelled using a 3rd-order Yeoh model [77]. The proximal arterial inlet boundary condition was based on a patient-specific velocity waveform acquired during Doppler echocardiography on the same day as the CT scan and a two-element (RC) Windkessel model was applied to both the distal arterial and proximal venous outlet using the flow split between outlets and the time-averaged inlet pressure. All inlets and outlets were treated as fixed, not allowing for any translation or rotation during deformation, and the model walls were assumed to be at atmospheric pressure.

Similar to other studies [74], [102], [106], [110], a decreased level of WSS and an elevated OSI was found in the venous segment of the AVF. The FSI analysis included in this study revealed notable wall deformation in the proximal arterial segment of the AVF (as great as 0.62 mm) and minimal deformation (as low 2.1×10^{-3} mm) at the proximal venous outlet [77]. More importantly, this group reported that their non-Newtonian assumption for blood led to a mean difference of -13% in the spatially-averaged WSS in the venous segment; that failing to differentiate wall properties in the arterial and venous segments led to a 14% overestimation of the WSS in the stenosis region of the AVF; and that failure to include the FSI effects resulted in a global overestimation of local velocity and WSS values [77]. The advantages and disadvantages of the assumptions made in this study are highlighted below (Figure 2.13). The authors did note that an FSI analysis could be omitted if the primary goal of the model is to provide a computationally inexpensive and qualitative picture of the prevailing hemodynamic conditions in the vasculature of interest [77].

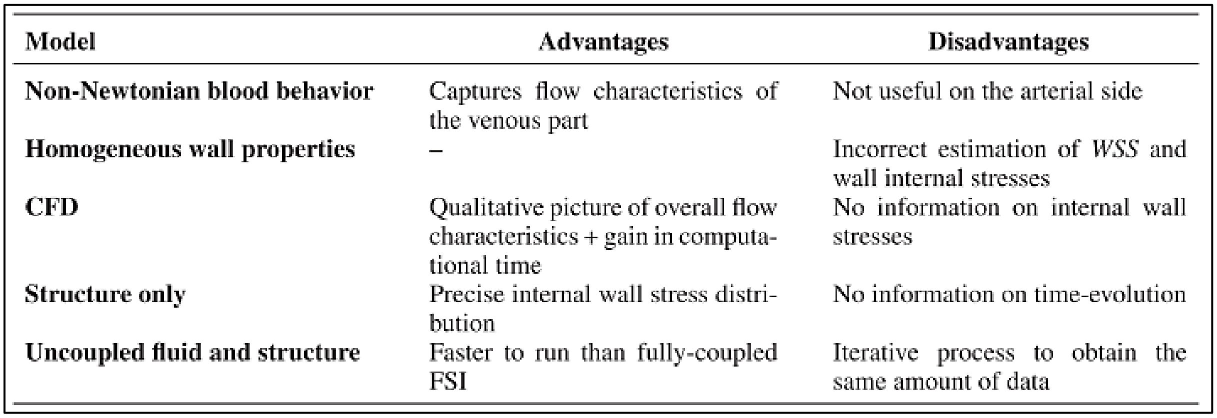

Model	Advantages	Disadvantages
Non-Newtonian blood behavior	Captures flow characteristics of the venous part	Not useful on the arterial side
Homogeneous wall properties	–	Incorrect estimation of *WSS* and wall internal stresses
CFD	Qualitative picture of overall flow characteristics + gain in computational time	No information on internal wall stresses
Structure only	Precise internal wall stress distribution	No information on time-evolution
Uncoupled fluid and structure	Faster to run than fully-coupled FSI	Iterative process to obtain the same amount of data

Figure 2.13. Advantages and disadvantages of assumptions made by Decorato et al. [77]**.**

Advantages and disadvantages of the various assumptions made by Decorato et al. [77] **in their 2014 study. Reprinted with permission from Wiley Publishing: John Wiley and Sons, *International Journal for Numerical Methods in Biomedical Engineering*, Decorato et al. (2014). Copyright 2013, Published 2014. No changes were made to this table.**

Guess et al. [67] built upon this work in a more recent study outlining protocol for running an FSI simulation that combined a blood flow model based on the finite volume method and a wall model based on the finite element method. Meshlab, SolidWorks, and ANSYS DesignModeler were used to reconstruct a single patient-specific AVF model and generate a mesh with an average element size of 0.316 mm. Guess et al. [67] chose to omit the non-Newtonian assumption for the fluid model and instead opted for a constant fluid and viscosity; this group did, however, use mechanical properties and wall thicknesses for the arterial and venous segments similar to those used by Decorato et al. [77] with the exception of a constant wall stiffness (0.01 N/mm^3) being assigned in this study rather than using a 3rd-Order Yeoh model. A mass flow rate boundary condition was assigned to the proximal arterial inlet while a three-element (RCR) Windkessel model was assigned to the distal arterial outlet and proximal venous outlet. This model was intended to mimic influences of upstream vessel resistance, downstream vessel resistance, and downstream vessel compliance [67]. The FSI model was then compared to a standard CFD model and, not surprisingly, the results were comparable to those reported by Decorato et al. [77]. It was found that the maximum velocity was lower in the FSI model and that peak WSS was overestimated by roughly 12% when considering only fluid dynamics, a value very close to that reported in the Decorato et al. [77] study. This methodology was later used in a follow-up study done by De Villiers et al. [111], who reported similar results.

Work done to characterize blood flow alone in AVFs (Table 2.3) has allowed THREE main conclusions to be drawn. The first conclusion, supported by Pike et al. [102] and Carroll et al. [74], is that patients undergoing dialysis exhibit increased cross-sectional areas of the fistula’s venous segment during maturation and dialysis. This increased cross-sectional area contributes to the second conclusion; it appears that blood flow velocity and WSS decrease in the venous segments of AVFs following creation [77], [110]. This slower moving blood is also subjected to increased blood recirculation and vortex formation, which is the third conclusion and may lead to impaired endothelial function and pathological changes in local vasculature [74], [102], [106].

Together, studies by Decorato et al. [77] and Guess et al. [67] both contributed notable amounts of information pertaining to the inclusion of FSI analyses when modelling AVFs (Table 2.3). Specifically, Decorato et al. [77] found that modelling blood as a Newtonian fluid led to a 13% overestimation in spatially-averaged WSS in the venous segment of the fistula and that the mechanical properties of the venous and arterial walls should be differentiated. Guess et al. [67] reached comparable conclusions in their study, finding that modelling fluid dynamics alone results in a global overestimation of velocity and WSS magnitudes. Based on these studies, it is evident that the vessel walls of AVFs play an important role in forming local hemodynamics and that these properties should be accounted for when possible.

Since it is suspected that high-output fistulas (defined in this study as those with flow rates greater than 1.5 L/min) may promote PH development, future work is needed to better quantify fistula hemodynamics in patients with varying flow rates. The clinical literature reviewed earlier in this document presents conflicting information about this issue. Work should also be done to determine the most clinically efficacious hemodynamic parameters for identifying problematic fistulas that may lead to the eventual development of pre-capillary PH in ESRD patients. This will allow for earlier intervention by physicians to limit the undesirable effects of problematic AVFs.

Table 2.3. Summary of Arteriovenous Fistula Models.

Group	Year	CFD or FSI?	Relevant Contribution
Carroll et al. [74]	2010	CFD	Increased cross-sectional area in AVF venous segments; High WSS gradients
Sigovan et al. [110]	2013	CFD	Decreased WSS following AVF creation; Recirculation in venous segment; Flow measurements 4-8 weeks post-creation can predict fistula outcome
Decorato et al. [77]	2014	FSI	Decreased WSS in venous segment of AVF; Lack of FSI and Newtonian assumptions lead to global overestimation of velocity and WSS
Bozzetto et al. [106]	2016	CFD	Turbulent flow and multi-directional WSS in venous segment
Pike et al. [102]	2017	CFD	Increased cross-sectional area, blood recirculation, and vortex formation in venous segment
Guess et al. [67]	2017	FSI	Lack of FSI analysis leads to global overestimation of velocity and WSS magnitudes

2.5.4.11 Limitations of Current Studies and Gaps in the Literature

While considerable amounts of work have been done to model both PAs and AVFs, there are a few limitations of current work and opportunities for improvement. The effects of including wall mechanics and non-Newtonian fluid assumptions in PA models are currently unclear. It is unlikely that Newtonian assumptions are problematic in PA models since they have a diameter larger than 0.5 mm [77], but, assuming extreme vascular hardening has not occurred, vessel wall mechanics may need to be included in these models.

As aforementioned, there are conflicting opinions in literature discussing the underlying connection between fistula flow rates and the development of PH. The most notable area for improvement in this literature is the inclusion of PA and fistula CFD models based on imaging done on the same patients within the same session. Modelling hemodynamics in these two anatomical areas of interest will allow for more convincing and quantitative conclusions to be drawn about relationships between high-output fistulas and the development of PH in ESRD patients. In order for this connection to be made, correlations must be found between the prevailing hemodynamic properties in AVFs and in the PAs of ESRD patients. Since no studies have analyzed PA hemodynamics using CFD in ESRD patients with PH, this is the first step to accomplish this improvement. Should this work be realized, physicians will be presented with parameters useful for monitoring fistulas and detecting PH development, allowing for earlier interventions to prevent the development of hypertensive conditions. This is a critical step for improving healthcare outcomes for ESRD patients as once PH is developed, patients are removed from the kidney transplant list. Earlier detection and intervention may also lead to a reduction of the health disparities associated with ESRD, a disease that has substantially higher prevalence among African-American, Hispanic, Native American, Asian, and elderly populations [9].

CHAPTER 3. METHODS

The following sections discuss the specific aims of the study and the methodology applied during the course of this project. Details are given about the steady-state rigid wall CFD model, the steady-state linear elastic FSI model, the steady-state hyperelastic FSI model, the transient rigid wall CFD model, and the transient linear elastic FSI model.

3.1 Specific Aims of Study

The primary, long-term objective of this project was to provide physicians with clinically useful parameters for monitoring AVFs so incidences of PH are kept to a minimum. Fluid-structure interaction models of PA blood flow must first be developed to better understand PA hemodynamics in this population. It is hoped this will allow ESRD patients an enhanced quality-of-life and better overall healthcare outcomes since they will not be as likely to develop PH and will not be removed from the kidney transplant list. In order for this goal to be achieved, there are three specific aims that were kept in mind throughout this study. These specific aims are as follows:

1. Further advance protocol for the computational modelling of the pulmonary artery with linear and hyperelastic FSI models;
2. Quantify the effects of vessel wall material models on pulmonary hemodynamics; and
3. Correlate AVF and PA hemodynamics so parameters of interest can be identified for patient monitoring.

These specific aims were chosen to build directly upon one another, contribute to the completion of this project, and promote the advancement of literature pertaining to this topic. The protocol for modeling PA blood flow will be advanced by employing advance material models in FSI simulation. The effects of wall material models on PA blood flow will be demonstrated by comparing rigid wall CFD models and FSI models. Utilizing both a retrospective and prospective approach, correlations between hemodialysis and PA hemodynamics will be found by analyzing fistula flow, length of time on dialysis, PA blood flow, and PA pressures.

3.2 Ethical Considerations

This study was approved by the East Carolina University Internal Review Board (IRB) (UMCIRB 19-000708). Safeguards were put into place to protect individuals at risk and to ensure patients were presented with no more than minimal risk. All files generated during this study were securely stored and de-identified on a password protected desktop. A patient key and discs containing imaging sets were stored in a locked desk in a locked office on campus. An IRB approval form is given in Appendix B.

3.3 Subject Selection

All of the above aims require the use of human subject data. General inclusion criteria for this study were as follows: all patients should be 18 years of age or older, have an arteriovenous fistula being used for dialysis, have PH confirmed via RHC, have no contraindications for MRI, have no diagnosed connective tissue disease, and have no advanced left heart disease. All prospective subjects were required to give their informed consent before beginning the study and were allowed to back out of the study at any time should they become concerned. The target prospective recruitment was five (*n* = 5) patients. Prospective subjects were used for computational modeling in Aims 1 and 2. To offer more opportunities for a larger sample size, retrospective patients were identified using the same inclusion criteria above and who had a cardiac MRI as part of their standard of care. To address Aim 3, the combined prospective and retrospective patients' data were used to find correlations between clinical measures and compare with PH population data from the literature.

3.4 Image Acquisition

The prospective subjects underwent MR imaging on a Siemens Aera 1.5 T scanner utilizing a gradient eco (GR) imaging sequence. This type of sequence is helpful when fast imaging of the anatomy of interest is necessary [60]. No contrast agent was used during this imaging session. To obtain imaging sets intended to be used in the reconstruction of the pulmonary artery geometry, the subject underwent a short axis cine scan. A sample image is given below in Figure 3.1. During this procedure, the subject was asked to lie in the supine position and hold their breath while imaging was conducted. Slice thickness was 8 mm with no gaps between slices. This allowed 22 slices to be collected while imaging this patient. An echo time of 1.34 ms was used, as was a repetition time of 289.5 ms. Pixel spacing was given as 1.61 mm.

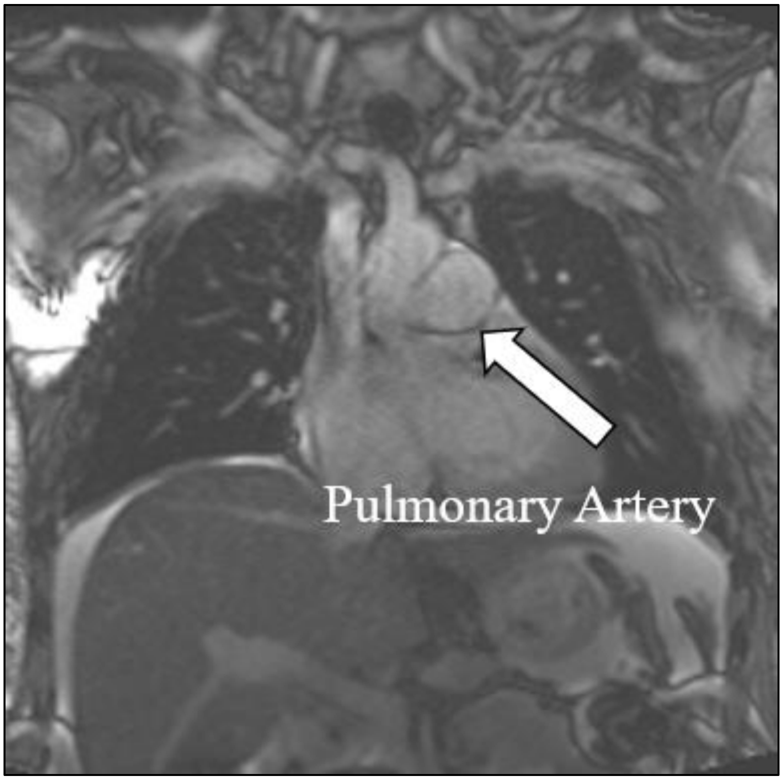

Figure 3.1. Example of the MR images used to recreate patient geometry.

To obtain imaging sets useful for the calculation of a transient velocity waveform throughout the cardiac cycle, the patient underwent phase-contrast MR imaging (PCMRI). PCMRI is an imaging technique used to visualize moving fluids [60]. When using this imaging technique, one is able to determine fluid velocity by quantifying the phase shift of a moving spin. This measure is proportional to fluid velocity [60]. In the same imaging session, data was collected in the PA just past the leaflets, RPA, and LPA. Images with a slice thickness of 6 mm were obtained at each location at 30 different time points during the cardiac cycle. Additionally, echo time was 3.01 ms, repetition time was 42.96 ms, pixel spacing was given as 1.77 mm, and the velocity encoding number used for this session was 100 cm/s. This value is representative of the maximum velocity expected to be encountered in the vessel and is necessary for the conversion of image intensity to velocity [60]. It is important to note the velocity being measured here is the thruplane velocity.

The patient also underwent phase-contrast imaging to capture fistula flow (Figure 3.2). Thirty timepoints were captured of blood flowing through the midplane of the AVF throughout the cardiac cycle. The echo time of the imaging set was 3.01 ms and the repetition time was 42.96 ms. Pixel spacing was given as 1.77 mm. The patient was supine during imaging so that the fistula was visible. This is the first study to acquire both PA and fistula flow during the same imaging session.

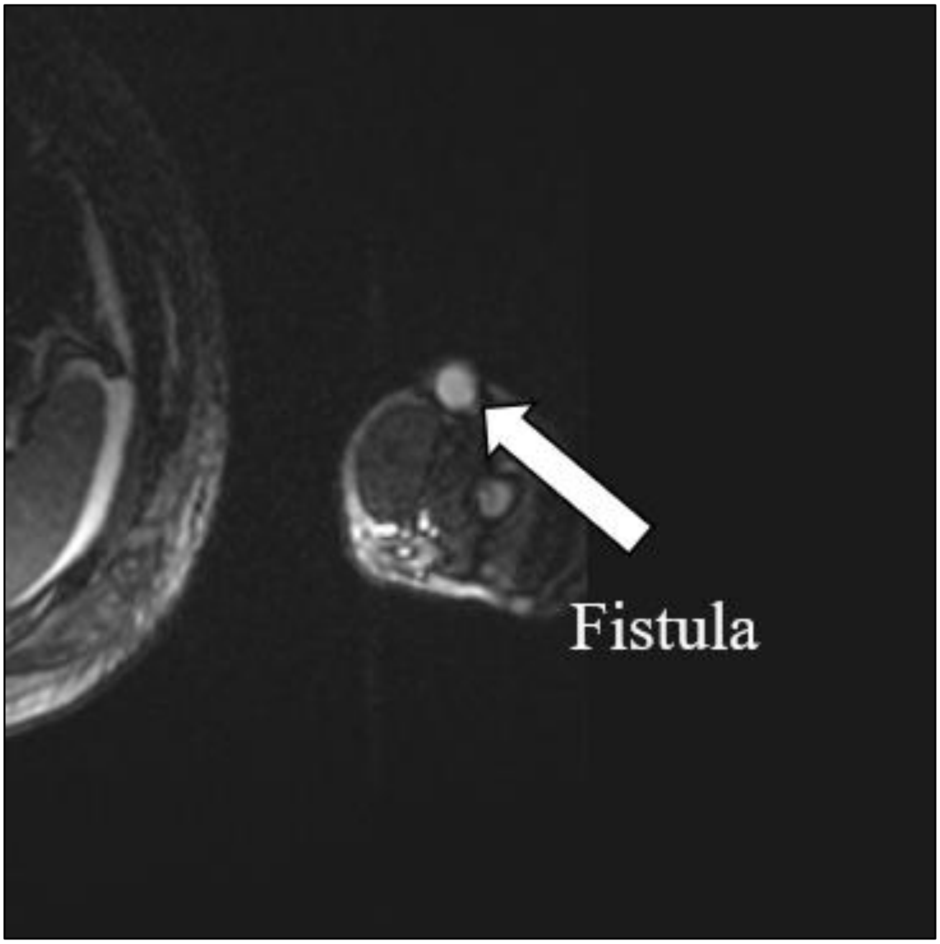

Figure 3.2. Example of the MR images done to capture fistula flow.

3.5 Computational Models Employed

To successfully accomplish the three aims, multiple models were run and are summarized in Table 3.1. The goal of Aim 1 is to develop a protocol for the linear transient FSI model (Simulation 5). The inclusion of steady-state models (Simulations 1-3) allowed for troubleshooting the coupling mechanisms prior to starting the more difficult transient FSI models. Running the rigid transient model (Simulation 4) allowed for troubleshooting of the transient boundary conditions. The simulation results were compared to determine the impact of wall model and time on PA hemodynamics (Aim 2). To investigate the clinical utility, the simulation results were correlated with clinical parameters of PH and compared to computational results from previous studies (Aim 3). It is worth noting that steady simulations require less time and computational power, which may provide greater clinical utility.

Table 3.1. Summary of simulations.

Simulation	Wall Model	Coupling	Time
1	Rigid	None (CFD)	Steady
2	Linear elastic (2 MPa)	Two way (FSI)	Steady
3	Hyperelastic (Yeoh Model)	Two way (FSI)	Steady
4	Rigid	None (CFD)	Transient
5	Linear elastic (2 MPa)	Two way (FSI)	Transient

The above simulations have several steps in common: 1) segmentation and 3D modeling of the PA; 2) domain meshing; 3) establishing boundary conditions and fluid/wall properties; 4) setting solver preferences; and 4) post-processing.

3.6 MRI Transient Velocity Waveform Creation

Inlet boundary conditions for both the steady and transient simulations were based on analysis of the PCMR data just past the leaflets in the PA. The generation of a transient velocity waveform emulating three full cardiac cycles was done using a previously developed code [112]. As discussed previously by Rabidou and George [60], a MATLAB file was used to manually crop and isolate the PA from each MR image. Another MATLAB file was used to segment the PA images using a region-growing method; manual corrections to segmented images were used when necessary. The PA cross-sectional area was segmented for each of the 30 timesteps collected throughout the cardiac cycle, allowing for a visualization of area change over time. Finally, another MATLAB file was used to multiply the segmented PA images with the phase portion of the image to calculate fluid velocity based on the phase shift of spinning particles. This provided velocity values across the region of interest. Relevant outputs from this process included the fluid flow rate (Figure 3.3), mass flow rate, artery diameter, and artery area for the inlet of the PA at 30 points throughout the cardiac cycle. The maximum velocity was used as the inlet condition for the steady cases; while further processing was needed for the transient cases. Since this process could be done for the other imaging sets obtained from the RPA and LPA, this process was also used for validation of the model, which is discussed in more detail at the end of this chapter. WSS was estimated at each timepoint using a modified Poiseuille’s equation (Equation 7), which was defined as:

$$WSS = \frac{4\mu Q}{\pi r^3} \tag{7}$$

where μ is the fluid's viscosity, Q is the volumetric flow rate, and r is the vessel radius.

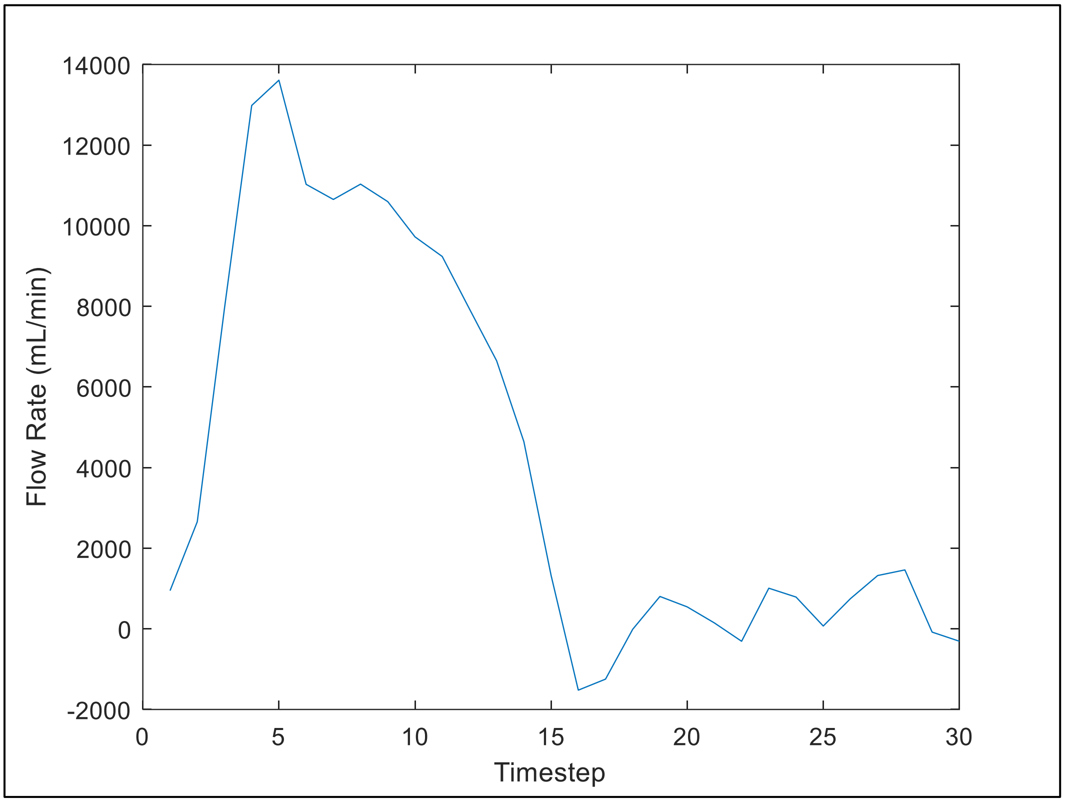

Figure 3.3. Sample fluid flow rate waveform calculated using MRI data.

These 30 volumetric flow rate values were divided by the cross-sectional area of the PA captured during MR imaging and imported into another MATLAB file that linearly interpolated a specified number of velocity values between each of the 30 points to create a velocity profile consisting of three cardiac cycles with many more velocity values in between each MRI velocity value. Three cardiac cycles were simulated to limit any start-up effects on model results. These values create smaller timesteps for the CFD and FSI analysis, which aids in model convergence, stability, and timestep independence. It should also be noted that this waveform was formatted as a .C file, enabling it to be interpreted and compiled as a user-defined boundary condition function in ANSYS FLUENT. The general workflow of this process is demonstrated below in Figure 3.4.

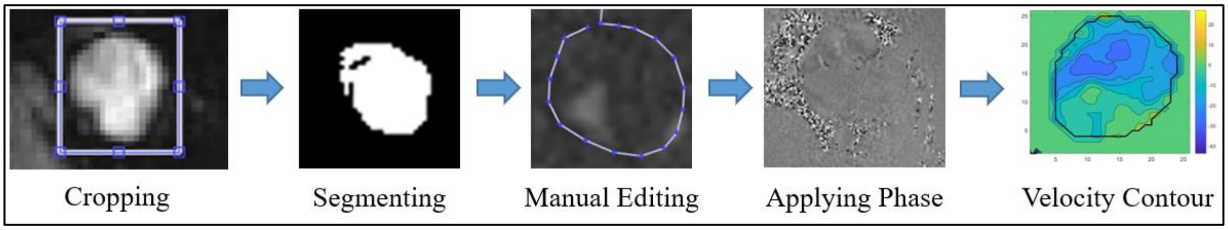

Figure 3.4. Steps for calculating a transient velocity profile and velocity contours.

3.7 Segmentation and Geometry Reconstruction

MR imaging sets were imported into Mimics 20.0 (Materialise, Belgium) for image segmentation and model reconstruction (Figure 3.5). A thresholding routine in Mimics was used to isolate the anatomical geometry captured in each MR slice and a “Calculate 3D” function was used to create a three-dimensional model (Figure 3.6) of the geometry highlighted in each image slice.

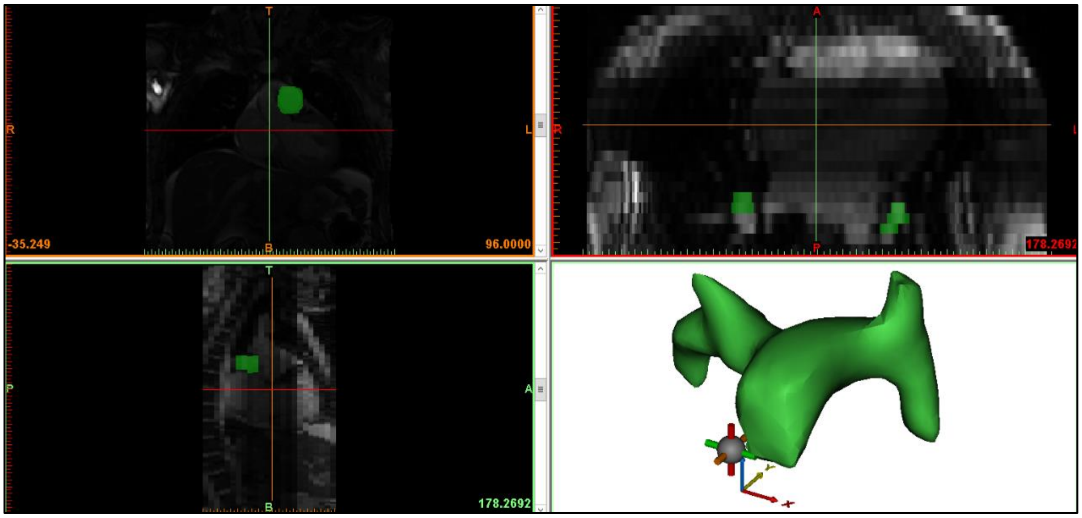

Figure 3.5. Anatomy segmentation of a pulmonary artery done in Mimics 20.0.

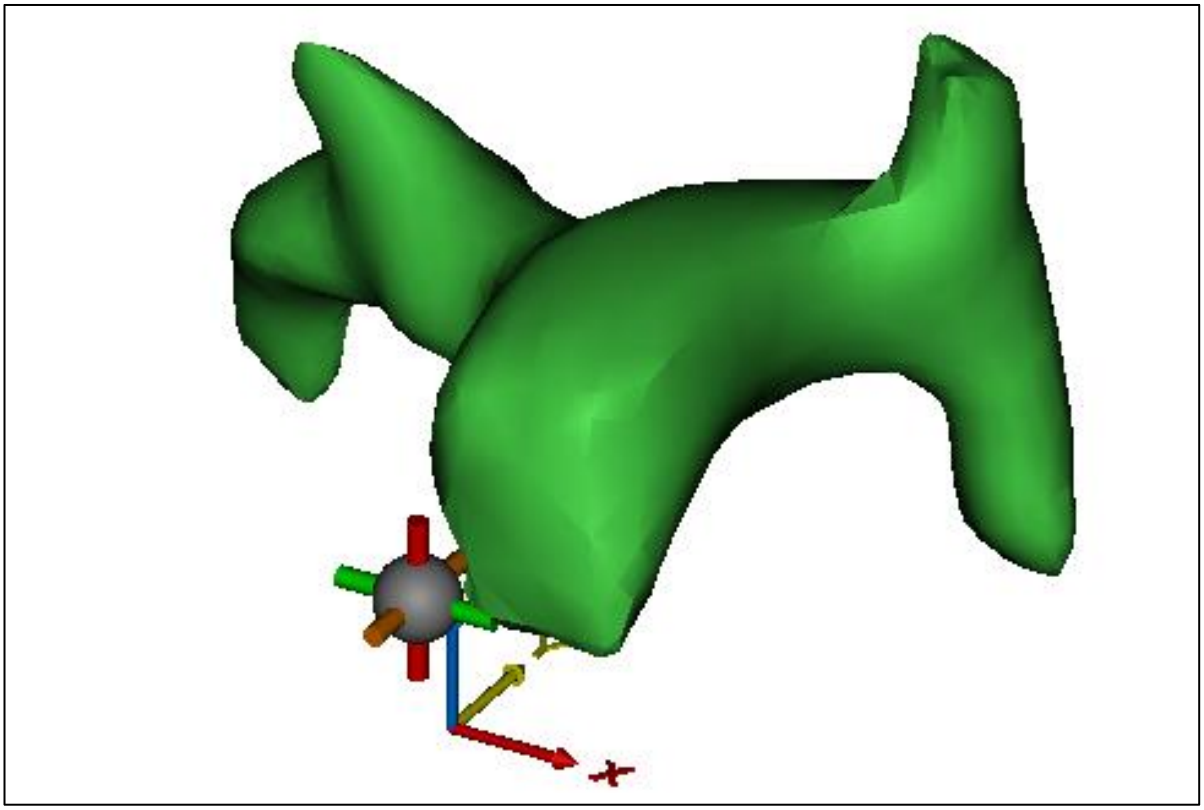

Figure 3.6. A smoothed, three-dimensional pulmonary artery model created in Mimics 20.0.

The three-dimensional model was smoothed in Mimics 20.0 to create a smooth model with no jagged edges or sudden geometry changes, exported as an .STL file, and imported into 3-Matic (Materialise, Belgium). The model was assigned an offset layer with an offset distance of 1.5 mm, which was meant to mimic the thickness of the pulmonary artery wall based on data from Azadani et al. [113]. This .STL file was then opened in SolidWorks 2017 (Dassault Systems, France), where the model was trimmed to create appropriate inlets and outlets that allowed simulated flow to enter and leave the model perpendicularly to the vessel. The "Combine" feature in SolidWorks 2017 was used to subtract the inner volume from the outer layer, rendering a solid shell representative of the pulmonary artery walls, or, more simply, the solid domain of the model. Cuts were made as far out from the geometry of interest as possible to ensure as much of the PA was modeled as possible. Additionally, these cuts were made perpendicular to the cross-section of the model (Figure 3.7). Modified geometries were saved as .SLDPRT files to ensure they could be uploaded into ANSYS Workbench for further analysis.

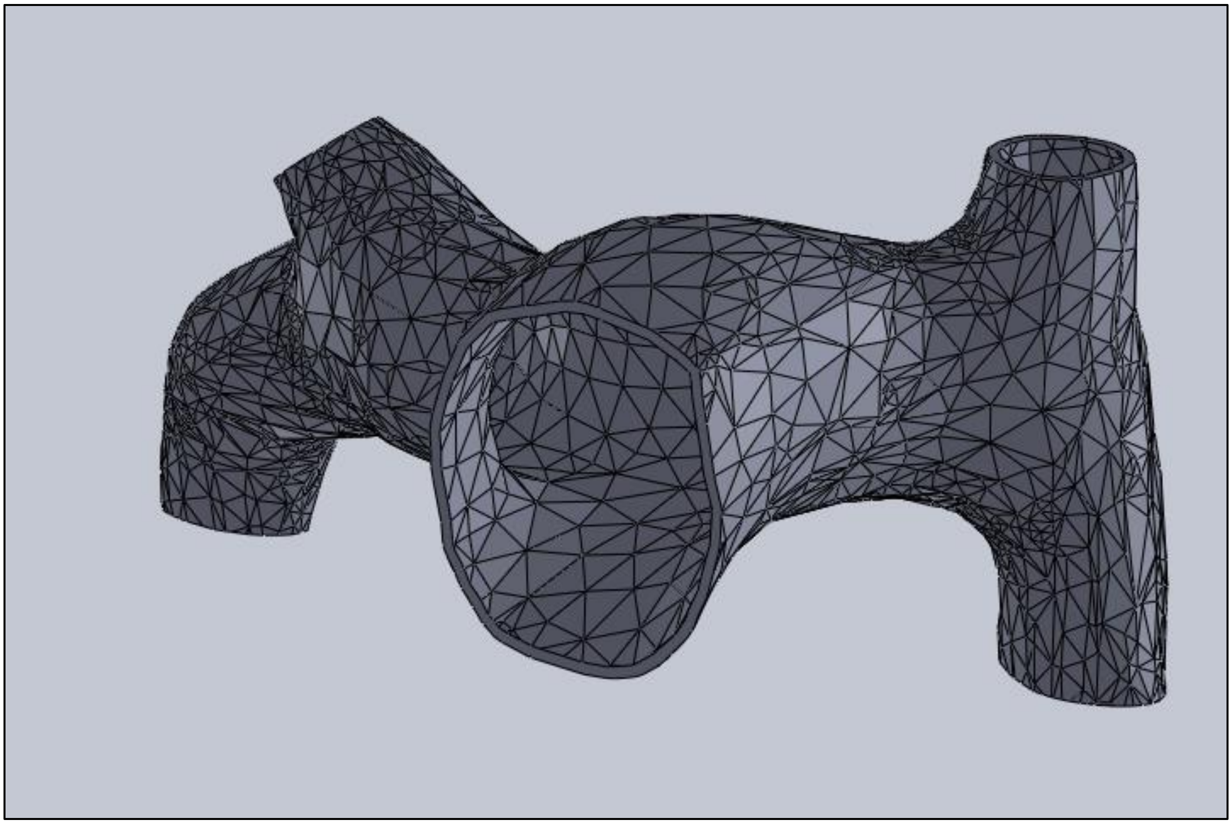

Figure 3.7. Pulmonary artery model trimmed in SolidWorks.

The trimmed model was then uploaded into SpaceClaim 19.1 (ANSYS, Inc., USA), where the “Volume Extract” feature was used to create a separate geometry based on the volume contained by the solid shell. This extracted volume, which is representative of the fluid domain of the model and the blood contained within the pulmonary artery, can be seen below in orange in Figure 3.8.

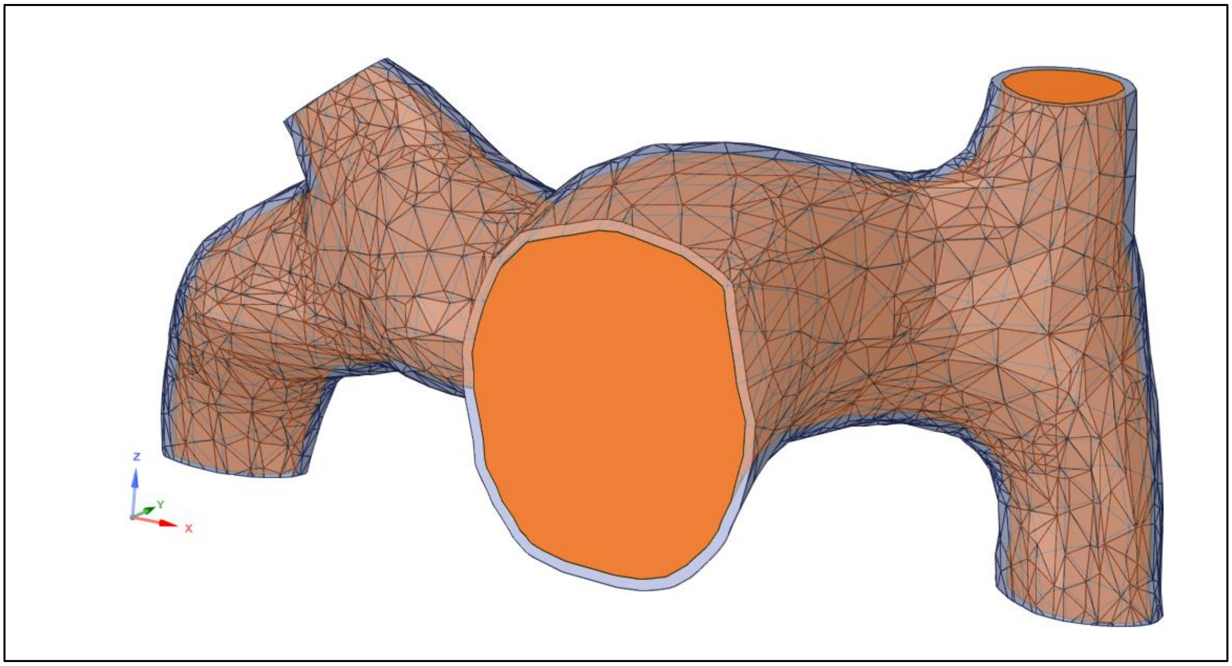

Figure 3.8. The fluid domain created using SpaceClaim.

3.8 Fluid Domain Meshing

The fluid volume was imported into ANSYS Meshing, where it was then discretized. A coarse mesh was applied initially and refined incrementally until the transient CFD model results were independent of mesh quality and changed by less than 1% with further mesh improvements. The details of this mesh independence test are given in Appendix A (Table 8.1). After conducting the mesh independence test, an element size of 1 mm was applied to the fluid domain using a Body Sizing function. Linear tetrahedral (Tet4) and wedge (Wed6) elements were used and nine inflation layers were added at the geometry wall to allow for better understanding of stresses occurring there. This resulted in a mesh comprised of 1,730,384 elements and 453,107 nodes. Based on earlier studies using between 1.2 and 1.6 million tetrahedral and polyhedral elements [60], [64], [94], this mesh size was not surprising. Metrics such as element quality, orthogonal quality, and skewness were used to assess mesh quality [59], [60]. The generated mesh had an average element quality of 0.693 ± 0.28, an average skewness of 0.205 ± 0.11, and an average orthogonal quality of 0.794 ± 0.11. Figure 3.9, given below, is a display of the finalized mesh used during this study.

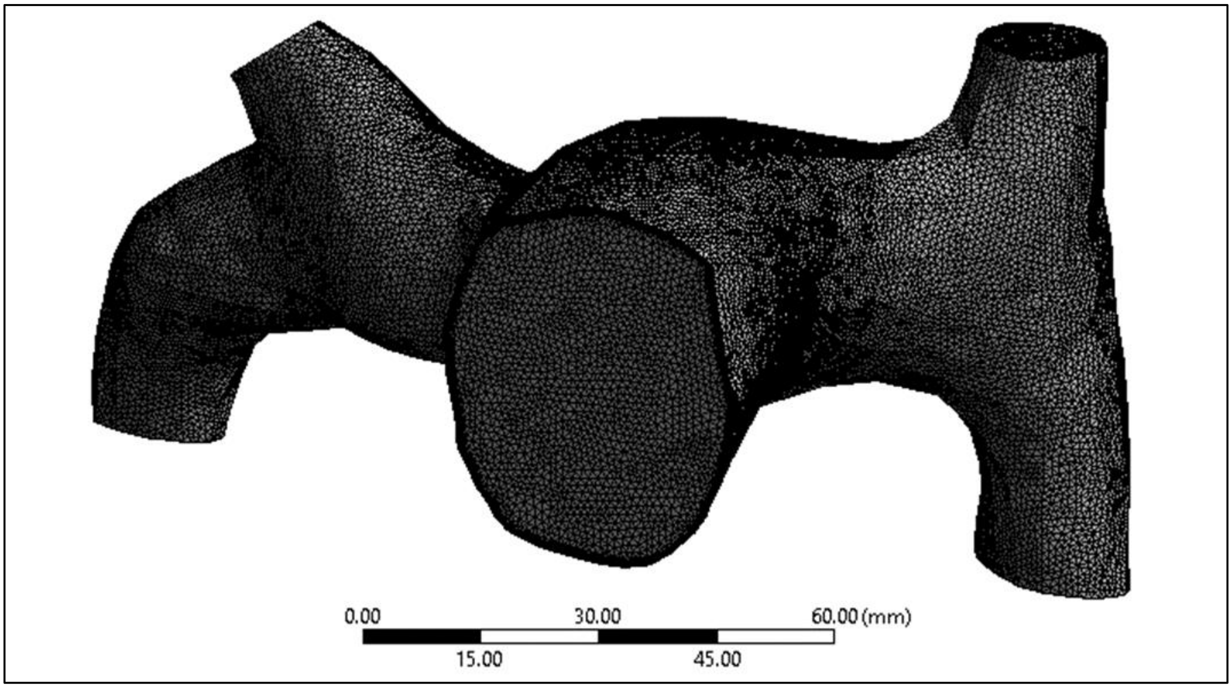

Figure 3.9. The discretized fluid domain after reaching mesh independence.

3.9 Solid Domain Meshing

The solid shell was imported into ANSYS Mechanical and meshed using methods similar to those described in Section 3.8. Using the maximum pressure exerted on the walls of the vessel during the transient CFD model at peak systole, which was approximately 200 Pa, a steady-state structural simulation was first run using a hyperelastic material model and then a linear elastic material model (E = 2 MPa, ν = 0.45) to determine mesh independence. A coarse mesh was applied and slowly refined until the maximum deformation of the geometry changed by less than 1% with further mesh improvements. The details of this mesh independence test are given in Appendix A (Table 8.2). Using a Body Sizing function and 1.6 mm elements, the mesh was then further refined to yield higher quality elements and to aid in model stability and convergence. This resulted in a solid domain comprised of 116,013 quadratic tetrahedral (Tet10) elements and 212,246 nodes. The average element quality was 0.724 ± 0.13, the average skewness was 0.385 ± 0.17, and the average orthogonal quality was 0.614 ± 0.17. To include multiple layers of elements in the vessel wall, the mesh element size was further decreased and another mesh independence test (Table 8.3 in Appendix A) was done; this finer mesh, however, was not used for modeling and may offer improved results if included in future studies. Figure 3.10 depicts the final mesh applied to the solid domain for this study.

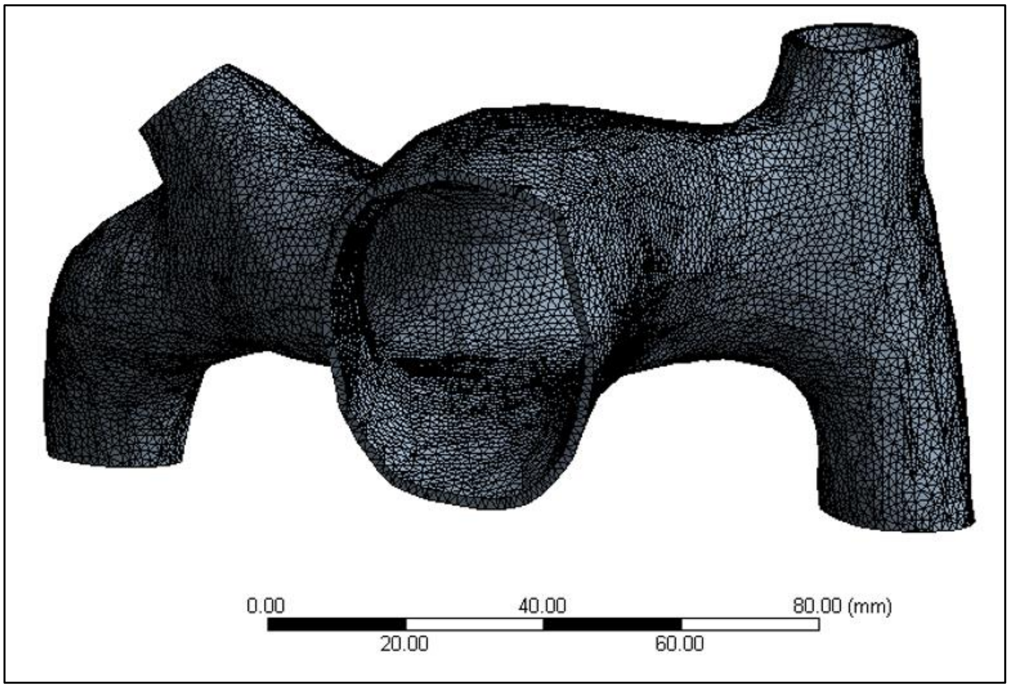

Figure 3.10. The discretized solid domain.

3.10 Fluid Properties

For this project, all simulations used the same fluid model. Using FLUENT 19.1, blood was modeled as a non-Newtonian fluid with a varying viscosity governed by a Carreau model, which is given below in Equation 8. This model is defined as:

$$\mu_{eff} = \mu_{\infty} + (\mu_o - \mu_{\infty})\left[1 + (\lambda\dot{\gamma})^2\right]^{\frac{n-1}{2}} \tag{8}$$

where μ_{eff} is the viscosity at any given time, μ_{∞} is the viscosity at an infinite shear rate, μ_o is the viscosity when the shear rate is zero, λ is a time constant in seconds, $\dot{\gamma}$ is the shear rate, and n is an experimental coefficient. For this model, properties from Cho and Kensey [68] were used; specifically, λ = 3.313 s, n = 0.3568, μ_o = 0.56 Poise, and μ_{∞} = 0.0345 Poise. A constant density value of 1060 kg/m^3 was applied.

3.11 Fluid Boundary Conditions and Solver Preferences

3.11.1 Steady State Simulations

For all steady-state models, the maximum velocity calculated from the MR-derived PA waveform was applied as a blunt profile to the PA inlet. The maximum velocity offered the best option for visualizing flow since the average and minimum velocities were both close to 0 m/s. All outlets were set as zero gauge pressure outlets, meaning that the geometry of the model governed how fluid flow was split between the RPA and LPA. For steady-state models, all simulations were simply permitted to run until convergence was reached. For all steady-state simulations, a viscous laminar model with a SIMPLE pressure-velocity coupling scheme was used, which included a second order pressure scheme and a second order upwind momentum scheme.

3.11.2 Transient Simulations

The model inlet was assigned a transient velocity waveform, described in Section 3.6, with a blunt profile. The waveform was repeated such that three cardiac cycles were simulated. The total simulation time was 2.385 s, with a single cardiac cycle time of 0.795 s and a single timestep duration of 0.0038221 s. A timestep independence test was conducted and is detailed in Appendix A (Table 8.4). In previous work [60], a waveform comprised of 180 timesteps was used for models to simulate all three cardiac cycles. In this study, solutions were found to be independent of timestep size when 446 timesteps were used in this study; however, increased stability was needed for the FSI simulation, so 624 timesteps were applied to the inlet to simulate all three cardiac cycles. Appendix A includes results from the timestep independence study, as stated above, and the velocity waveform used to create the 624 timesteps (Table 8.5). All outlets were set as zero gauge pressure outlets. These boundary conditions and their general locations on the models are shown below in Figure 3.11. For all transient simulations, a viscous laminar model with a SIMPLE pressure-velocity coupling scheme was used. This coupling scheme included a second order scheme for pressure and a second order upwind scheme for momentum. An implicit first order scheme was used for transient formulation.

3.11.3 System Coupling Settings for FLUENT

Residual levels for the fluid simulation were set to 10^{-3} and up to 25 FLUENT iterations were permitted during each System Coupling iteration for the FSI model, meaning that 25 FLUENT iterations could occur during each of the 8-15 System Coupling iterations that were permitted during each timestep of the simulation. For the transient rigid wall CFD model, up to 35 FLUENT iterations were allowed at each of the 624 timesteps.

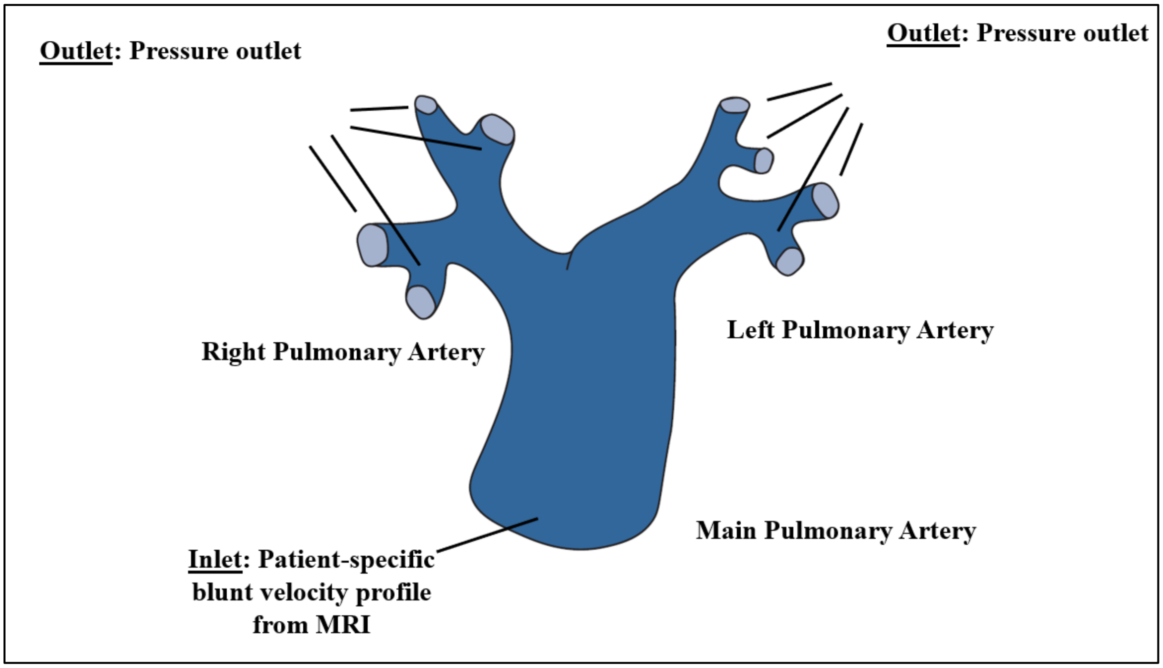

Figure 3.11. Fluid boundary conditions for pulmonary artery models.

3.12 Solid Boundary Conditions and Solver Preferences

For this project, FSI models were run under both steady-state and transient conditions using the following properties and settings. Rigid models were implemented within the CFD framework and thus no additional conditions for the solid boundary were needed.

The solid domain was assigned boundary conditions similar to those used in earlier studies [95], [97]. This setup was most similar to Zambrano et al. [95], where the more proximal portions of the PA (MPA, RPA, and LPA) were modeled. The model inlet was fixed, model outlets were fixed, and the vessel walls were allowed to freely deform throughout the simulation of the cardiac cycles. These boundary conditions are shown below in Figure 3.12. Like work done by Zambrano et al. [97], Hunter et al. [114], and Kong et al. [95], a linear modulus of 2 MPa, a Poisson's ratio (v) of 0.45, and a vessel wall density of 1200 kg/m^3 was used for the linear elastic FSI model. A hyperelastic model for wall deformation was also developed using a curve fitting algorithm in MCalibration (Veryst Engineering, Needham, MA) and experimental mechanical testing data done on samples of human pulmonary artery tissue from Azadani et al. [113].

A 3rd order Yeoh model was used to model hyperelasticity due to the improved numerical stability of this model and its ability to accurately predict both small and large strains [72]. This model is shown below in Equation 9 and is defined as:

$$W = \sum_{i=1}^{n} c_{i0}(\bar{I}_1 - 3)^i + \sum_{k=1}^{n} \frac{1}{d_k}(J-1)^{2k} \tag{9}$$

where W is the strain energy potential, I_1 is the first invariant of the Cauchy-Green strain tensor, J is the volumetric strain, and c_{i0}, d_k, and n are all constants [115]. For this particular model, the vessel was assumed to be nearly incompressible and coefficients were: c_{10} = 0.02986 MPa; c_{20} = -0.095128 MPa; c_{30} = 0.622106 MPa; $d_{1\text{-}3}$ = 0.0005 MPa^{-1}; and n = 3. These values were determined using a curve fitting algorithm that modeled stress-strain curves. The hyperelastic material model was used only for the steady-state hyperelastic FSI model. A total of three material models (rigid wall for CFD, linear elastic for FSI, and hyperelastic for FSI) were used to compare and better quantify effects of the mechanical properties of PA walls on model results.

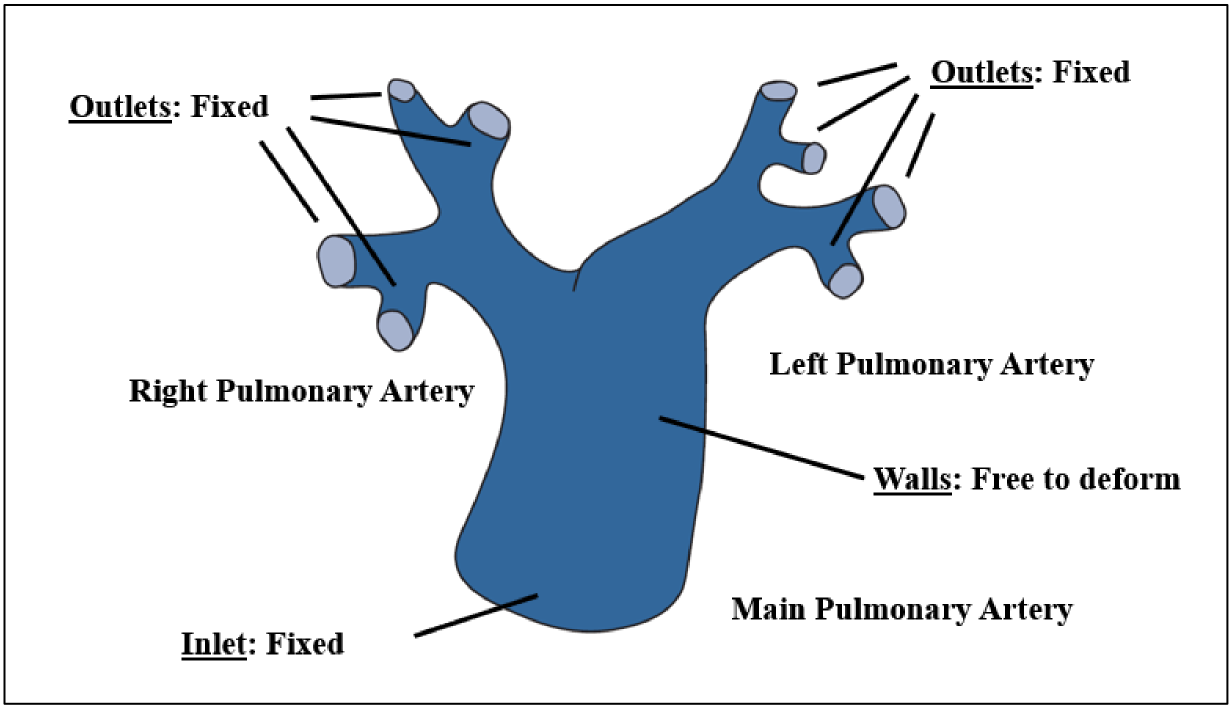

Figure 3.12. Solid boundary conditions for pulmonary artery models.

3.13 System Coupling and Fluid-Structure Interaction Boundary Conditions

The System Coupling module in ANSYS Workbench 19.1 was used to set up a fully coupled, two-way, steady-state FSI model (linear and hyperelastic material properties) and a fully coupled, two-way, transient FSI model (linear material properties).

For the steady-state models, a single timestep was applied. A minimum of 150 and a maximum of 300 coupling iterations were applied, as was linear ramping up to the minimum iteration, to allow the models to slowly and steadily converge without causing element distortion. This setting allowed for the pressure contour from the FLUENT analysis to be slowly applied to the solid domain, which improved model stability and convergence. The Data Transfer that governed transferal of pressure values from FLUENT to the static structural model was set up with an under-relaxation factor of 0.2 and a convergence target of 10^{-2}. The Data Transfer governing displacement values to the fluid model was set up using a standard under-relaxation factor of 1 and a convergence target of 10^{-2}. These models were allowed to run until full convergence was reached.

For the transient model, a transient velocity profile consisting of three cardiac cycles that lasted a total of 2.385 s was used as a boundary condition. In the System Coupling module, this profile was defined by 624 coupling steps that were each 0.0038221 s in length. A minimum of eight and a maximum of 15 coupling iterations were defined for this model, meaning that both FLUENT and Mechanical could run through their solving process and the data transferal process a maximum of 15 times for each step to ensure that both fluid and mechanical solutions were converged and stable. Linear ramping was used to incrementally apply the FLUENT pressure load to the solid domain. The FLUENT data transfer was prescribed an under-relaxation factor of 0.55 and a convergence target of 10^{-2}, whereas the transient structural data transfer was given an under-relaxation factor of 1 and a convergence target of 10^{-2}. The model was allowed to run until either convergence or the maximum number of coupling iterations was reached for each of the 624 coupling steps. All models were run on a Dell Optiplex 9020 desktop with an Intel i7-4770 3.40 GHz CPU with four cores, eight logical processors, and 16 GB of RAM. These models were all partitioned across these eight processors to decrease computation time.

3.14 Post-Processing and Data Analysis

Post-processing procedures for the fluid domain was done in CFD-Post 19.1. These procedures including the creation of velocity streamline plots, velocity volume renderings, WSS contours, and pressure contours visualized in CFD-Post for timesteps throughout the cardiac cycle. Post-processing for the solid domain was handled in ANSYS Mechanical. Contours for total deformation, equivalent elastic strain, and equivalent von Mises stress were created for every timestep of the simulation. Videos of fluid flow and vessel deformation were also created and are available upon request.

3.15 Model Validation

The fluid model was validated at the mid main RPA using the transient linear elastic FSI model. The cross-sectional velocity contours throughout the cardiac cycle calculated using the MATLAB codes discussed in Section 3.6 were compared to the cross-sectional velocity contours generated in CFD-Post at a similar location in the mid main RPA using the transient linear elastic FSI model. This was done to ensure that the CFD simulation produced velocity values were similar to those determined in the cardiac MRI imaging sets. There were limited options for validating the pulmonary artery wall deformation values predicted in ANSYS Mechanical. These values were compared to those discussed in other studies, like those done by Kong et al. [95] and Zambrano et al. [97].

3.16 Statistical Analysis

Percent differences were calculated between the maximum velocities and WSS of the three steady-state models and between the two transient models. For retrospective patients, average values were calculated for clinically relevant parameters from RHC and a one-tailed Student's T-Test was used to compare groups of retrospective patients based on the amount of time they had been on hemodialysis. This comparison was made in an attempt to find correlations between time on hemodialysis and pulmonary artery pressures and this particular test was chosen to see if either hemodialysis group had significantly greater or lesser PA pressures. Since it is expected that patients that had been on hemodialysis for a longer amount of time would have higher PA pressures than patients that had been on hemodialysis for a shorter amount of time, a one-tailed test was selected to determine if there was an increase in PA pressures.

CHAPTER 4. RESULTS

This chapter of the thesis details results found using the methodology in the preceding chapter. MR imaging velocity analysis results are discussed first, then model validation, then results from steady-state models, and, lastly, findings from the transient CFD model and FSI model.

4.1 Patient Recruitment

Due to the COVID-19 pandemic, patient recruitment was limited to one ($n = 1$) prospective patient. This individual was an African American male, was 41 years of age at the time of imaging, had been diagnosed with PH via RHC several months before the time of imaging and had an arteriovenous fistula being used in dialysis. Upon RHC, this patient had an mPAP of 54 mmHg, a PCWP of 35 mmHg, a PVR of 2.07 Wood Units, and a cardiac output of 8.2 L/min. At the time of MR imaging, the patient was still undergoing hemodialysis using the fistula imaged during this session. The patient was not undergoing hemodialysis while inside of the MR machine.

For retrospective patients, a total of eight ($n = 8$) subjects were identified. These individuals had all been on dialysis and had PH confirmed via RHC. Clinical data from these patients is given below in Table 4.1. These eight patients had an average mPAP of 42.9 ± 5.74 mmHg. This average mPAP value is comparable to the average mPAP found for PH patients in earlier work [60]. The three PH patients analyzed by Rabidou and George [60] all had pre-capillary PH and had an average mPAP of 40.3 ± 4.04 mmHg. One of these pre-capillary PH patients did have sickle cell disease, so their expression of PH may have been slightly different from traditional pre-capillary PH patients.

Table 4.1. Summary of retrospective patient's clinical results.

Patient #	Ethnicity	Sex	PH WHO Class	Time on Dialysis	mPAP (mmHg)	PCWP (mmHg)
1	African American	Female	Group Va (Multifactorial)	3-5 years	46.52	19
2	African American	Female	Group Va (Multifactorial)	7-10 years	39.9	26
3	African American	Female	Group Va (Multifactorial)	7-10 years	36.5	14
4	African American	Male	Group Va (Multifactorial)	3-5 years	36.91	10
5	African American	Female	Group Va (Multifactorial)	3-5 years	45.57	28
6	African American	Male	Group Va (Multifactorial)	3-5 years	51.5	20
7	African American	Female	Group Va (Multifactorial)	7-10 years	38.5	12
8	African American	Male	Group Va (Multifactorial)	7-10 years	48.51	35

4.2 Retrospective Patient Analysis

Using data from Table 4.1, a Student's T-Test was used to compare mean values for mPAP and PCWP based on time of dialysis (3-5 years vs. 7-10 years). For mPAP, the 3-5 year group had an average mPAP of 45.1 ± 6.06 mmHg. The 7-10 year group had an average mPAP of 40.8 ± 5.29 mmHg. A one-tailed T-Test returned no statistical difference between these two groups (p = 0.165). For PCWP, the 3-5 year group had an average PCWP of 19.3 ± 7.37 mmHg and the 7-10 year group had an average PCWP of 21.8 ± 10.8 mmHg. No statistical difference was found between groups for this variable either (*p* = 0.357). All individuals in this cohort were African American and five of the eight individuals were female.

4.3 MRI Velocity Analysis Results

The following results were used to create the velocity waveform used as an inlet boundary condition in FLUENT. During PCMRI, an average RR interval of 0.795 ± 0.173 seconds was recorded over 22 heartbeats. Imaging data were collected just past the leaflets of the pulmonary artery. Appendix A includes a table with results for each of the 30 timesteps throughout the patient's cardiac cycle (Table 8.5). Table 4.2, given here, includes patient averages for vessel area, velocity, volumetric flow rate, vessel diameter, and WSS for these 30 points. For this data set, the maximum WSS estimated using Equation 7 was 1.694 dyn/cm^2.

Table 4.2. Mean PA values for MATLAB output variables throughout a single cardiac cycle.

Vessel Area (cm^2)	**Velocity (cm/s)**	**Flow Rate (mL/min)**	**Diameter (cm)**	**WSS (dyn/cm^2)**
10.243	6.756	4146.751	3.611	0.570

Figure 4.1 shows the velocity waveform calculated using the patient's MR imaging set. Red markers denote points where MR velocity values were captured throughout the patient's cardiac cycle.

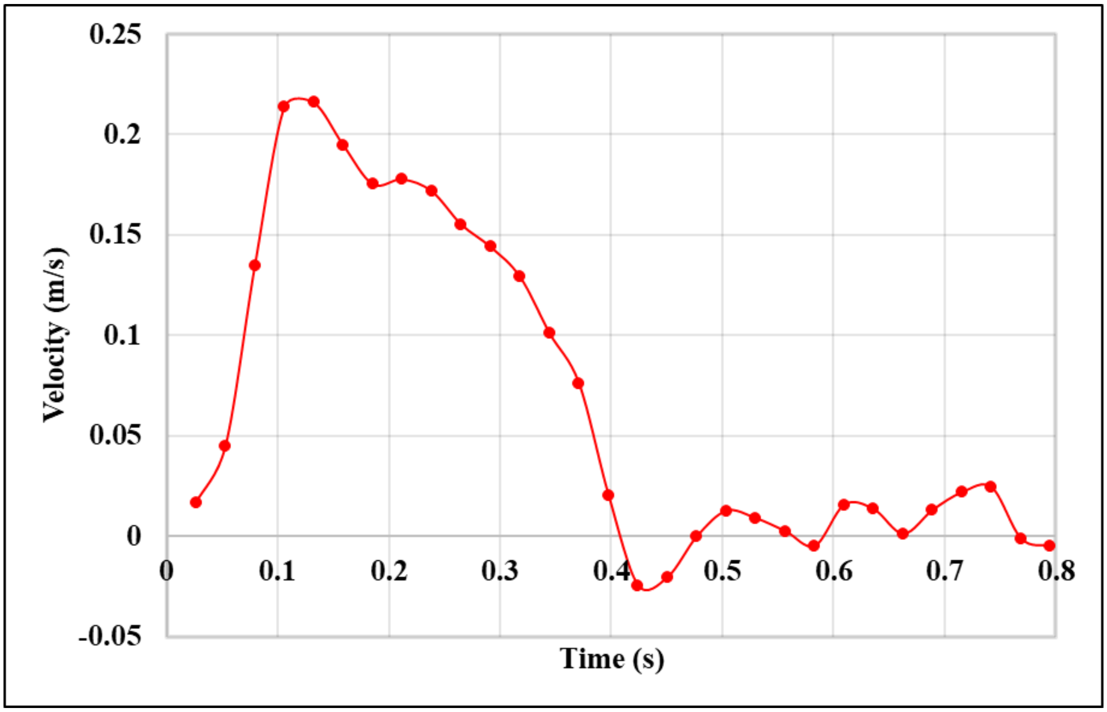

Figure 4.1. Velocity waveform obtained through MATLAB analysis of the MRI set.

For imaging of the fistula, the patient was supine in the MR machine. This allowed for the brachial AVF to be captured in the images. An average RR interval of 0.781 ± 0.005 seconds was recorded over 22 heartbeats. The patient had an average flowrate of 1.96 L/min upon analysis of the PCMRI set. The volumetric flow rate through the fistula cross-section throughout a cardiac cycle is shown below in Figure 4.2.

Table 4.3. Mean AVF values for MATLAB output variables throughout a single cardiac cycle.

Vessel Area (cm^2)	Velocity (cm/s)	Flow Rate (mL/min)	Diameter (cm)	WSS (dyn/cm^2)
1.87	17.6	1972.4	1.54	3.27

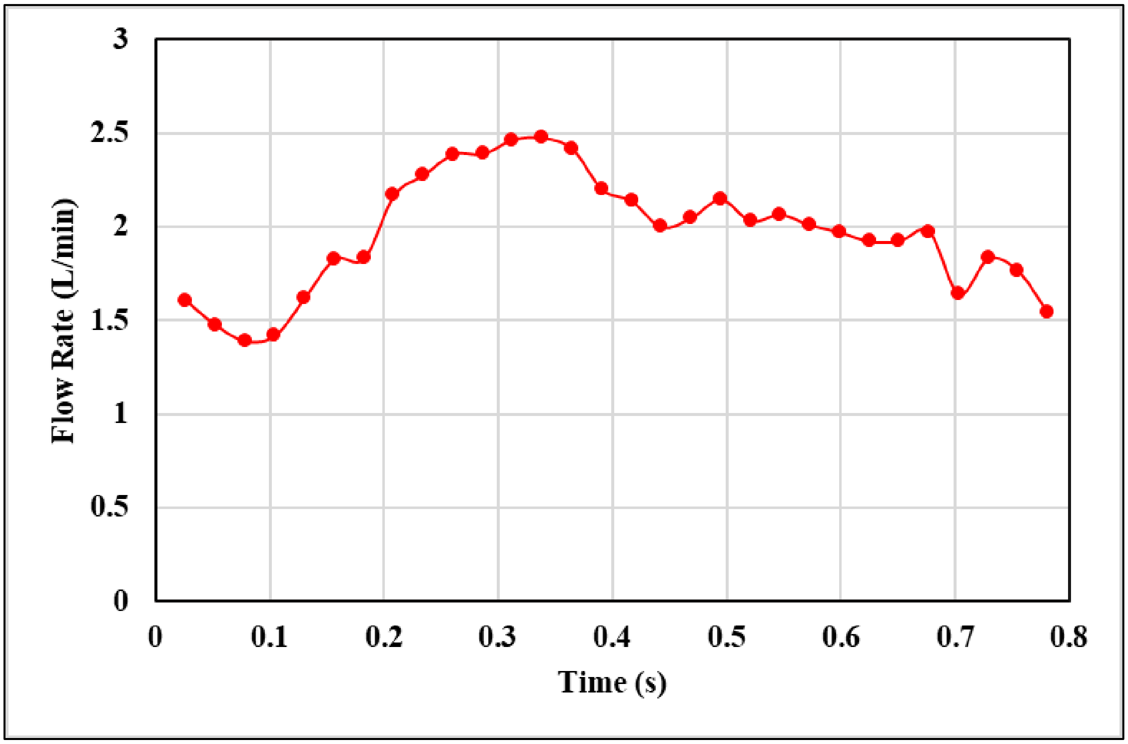

Figure 4.2 Mass flow rate waveform through the AVF for a single cardiac cycle.

4.4 Transient Model Validation

Before analyzing results from any simulations, the transient FSI model was validated to ensure reasonable results. Figure 4.4, given below, shows validation results for the transient FSI model.

Three different points throughout the cardiac cycle, including early systole (A), peak systole (B), and early diastole (C), were selected. Planar cross-sections with velocity contours were created in FLUENT (Figure 4.3) using the transient linear FSI model and compared to cross-sectional contours from a MATLAB analysis using PCMRI scans taken from the midplane of the right PA. At Point A, both MATLAB and FLUENT calculated relatively intermediate velocities throughout the PA. The MATLAB calculations returned an average velocity of 15.8 cm/s located on the left-hand side of the cross-sections shown in Figure 4.4. FLUENT estimated similar velocity distributions; however, FLUENT results revealed an average velocity of about 13.2 cm/s at Point A. MATLAB analysis at Point B revealed an average velocity of 28.4 cm/s on the left-hand side of the cross-section, whereas FLUENT estimated a maximum velocity of only 19.5 cm/s. Based on the images shown for Point B in Figure 4.4, it appeared as though fluid flow was developing congruently and in relatively similar areas for both cross-sections. Finally, at Point C, similar velocity distributions were seen across the cross-sections analyzed in both MATLAB and FLUENT. Lower velocities ranging between 10 and -10 cm/s dominated both cross-sections; the MATLAB velocity contour had an average velocity of -0.002 cm/s and the FLUENT velocity contour had an average velocity of 0.05 cm/s. Additionally, maximum velocities for both cross-sections appeared on the right-hand side of the cross-sections. Overall, a comparison of the MATLAB analysis of the MRI set and FLUENT results revealed a general underestimation of fluid flow velocities. Qualitatively, however, similar trends in fluid flow development and velocity distributions across the varying cross-sections were seen and do not appear too different.

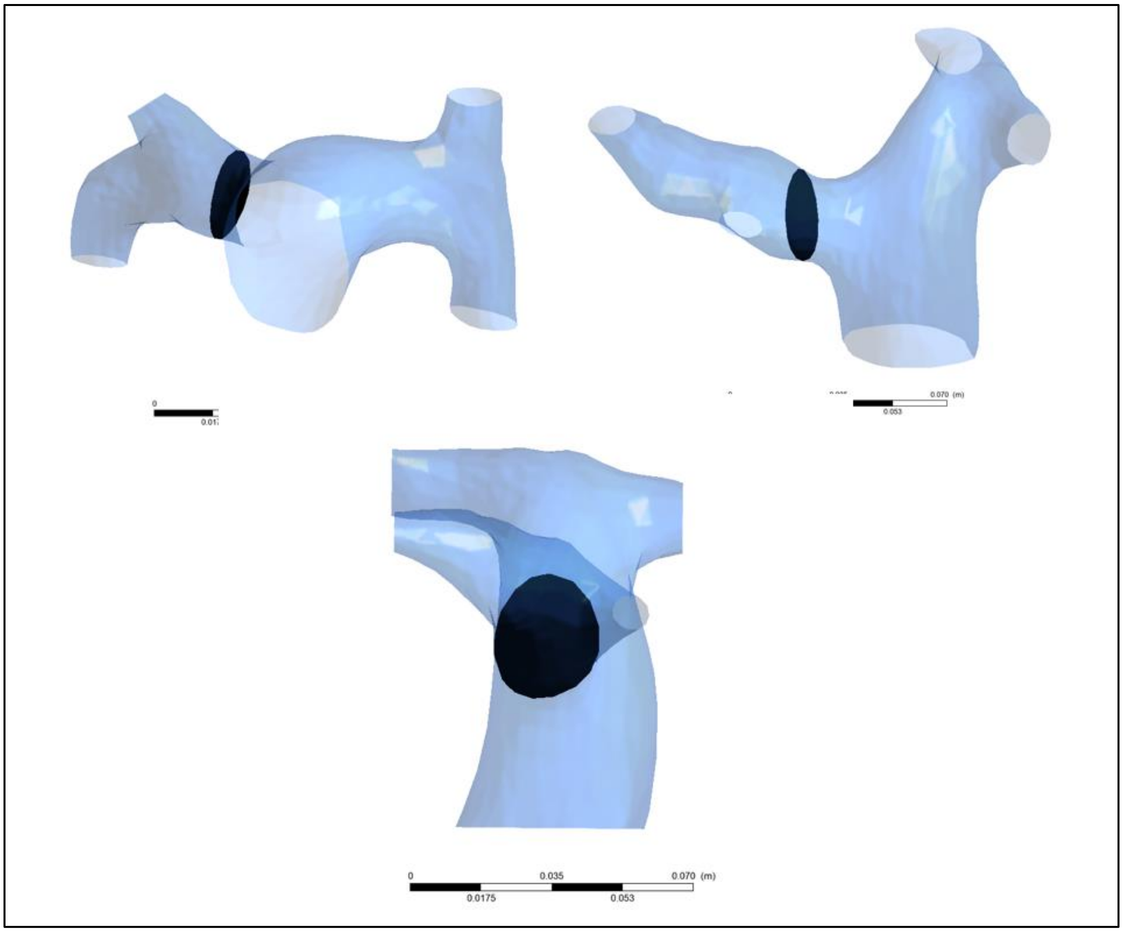

Figure 4.3. Location of FLUENT cross-sections analyzed for model validation.

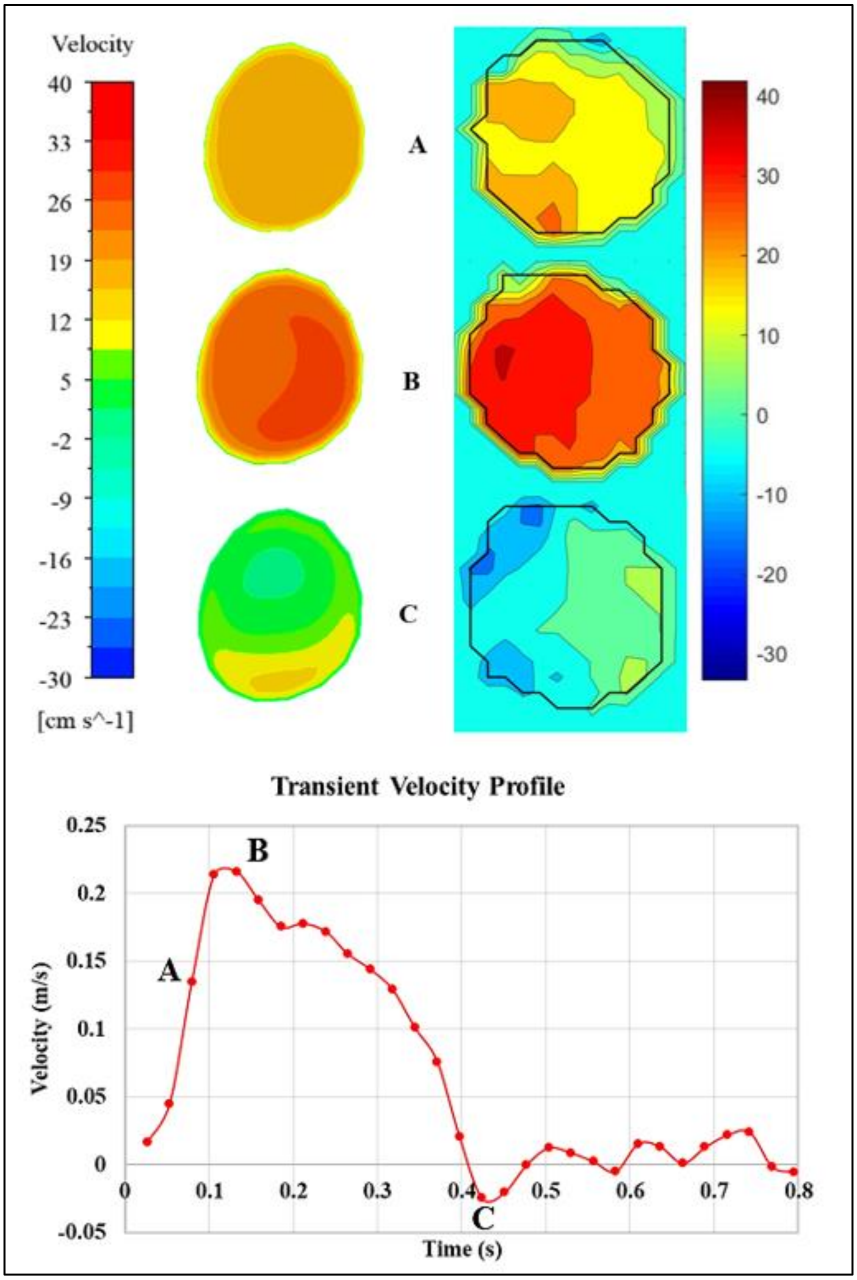

Figure 4.4. A comparison of MATLAB and FLUENT cross-sections used for model validation.

For both FLUENT (top left) and MATLAB (top right), midplane cross-sections from the right PA were analyzed at three different time points throughout the cardiac cycle (bottom). The velocity profile shown is the same as that in Figure 4.1 and is only used to depict time.

4.5 Steady-State Models

The following section states results obtained from the two steady-state FSI models and the steady-state rigid wall CFD model run in ANSYS Workbench. Fluid results are discussed first and followed by results from ANSYS Mechanical.

4.5.1 Steady-State Fluid Results

Given below, Figure 4.5 includes velocity streamlines for the steady-state rigid wall CFD model run using a constant inlet velocity of 0.2159 m/s. A maximum velocity of 0.650 m/s and a minimum velocity of 0 m/s were calculated for this model. The volume weighted average velocity for this model was 0.224 m/s.

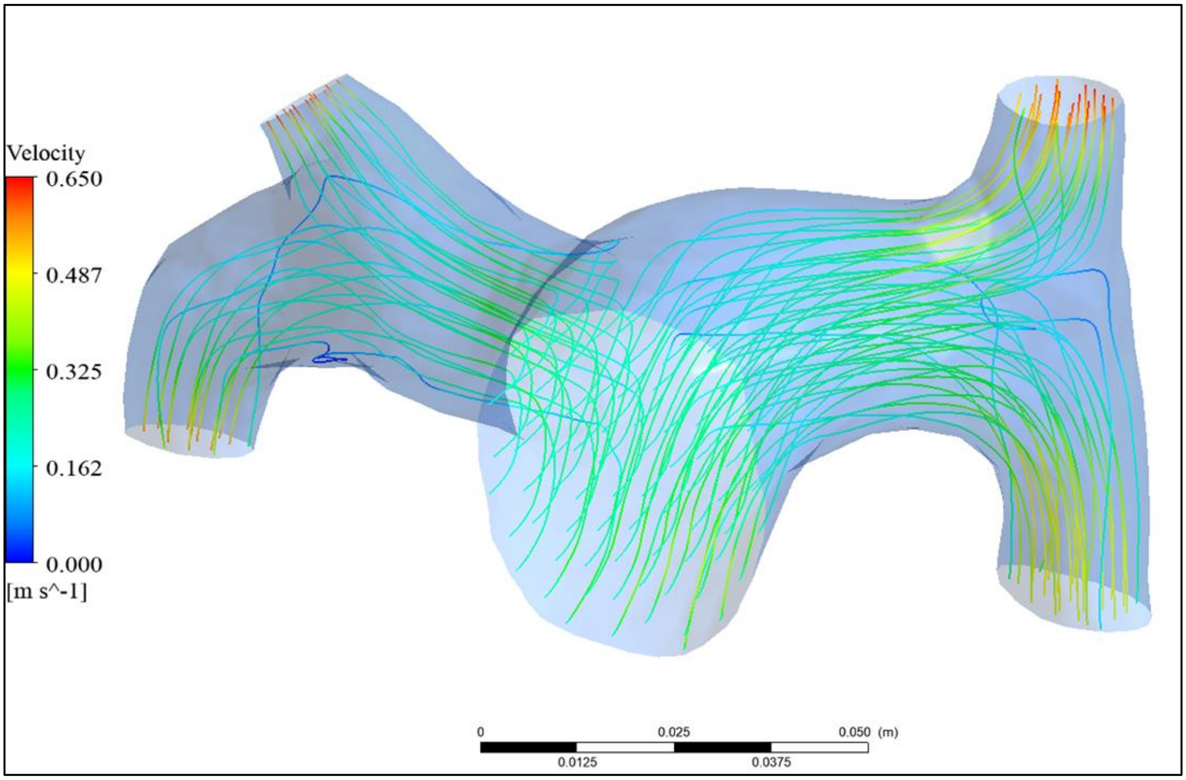

Figure 4.5. Velocity magnitude streamlines for the steady-state rigid wall CFD model.

Figure 4.6 shows a volume rendering for the fluid velocity in the steady-state rigid wall CFD model. As mentioned above, a maximum velocity of 0.650 m/s were found for this model.

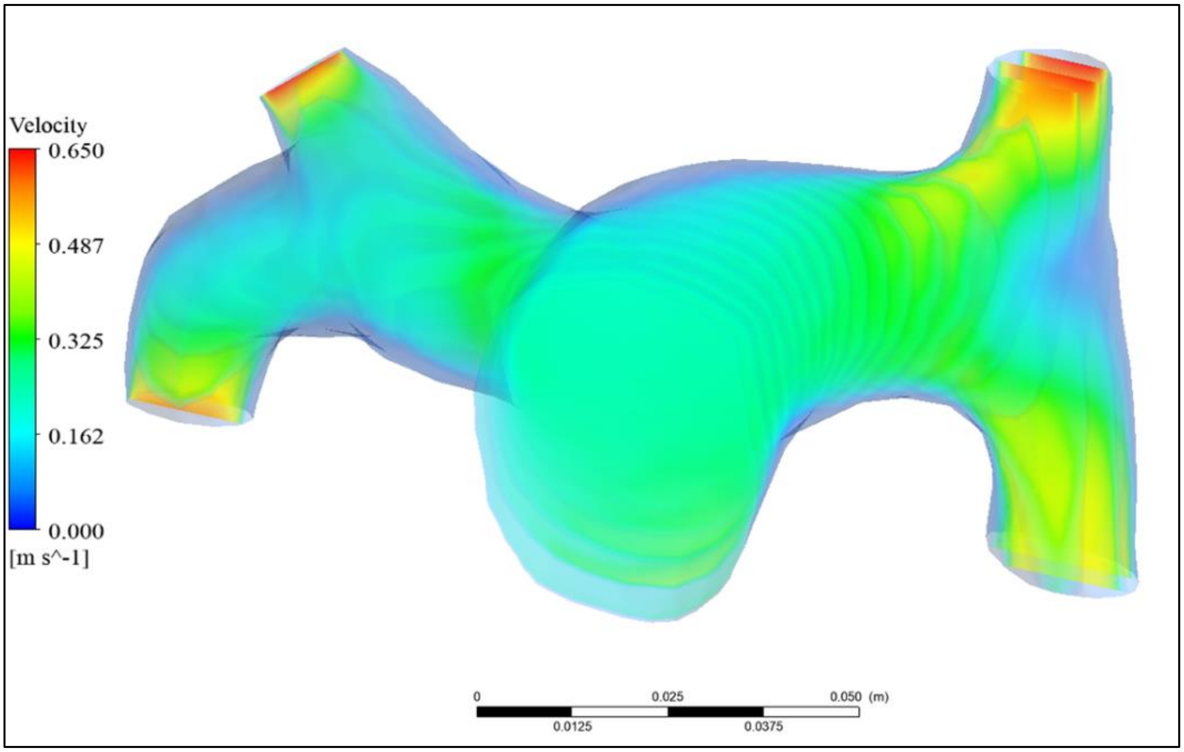

Figure 4.6. Velocity volume rendering for the steady-state rigid wall CFD model.

Figure 4.7 depicts, given below, portrays the wall shear stresses experienced in the steady-state rigid wall CFD model. For this model, a maximum WSS of 30.9 Pa, a minimum WSS of 0.0835 Pa, and an average WSS of 2.64 Pa were calculated. The maximum WSS occurred at the inlet and the minimum WSS occurred in the right and left branches of the PA.

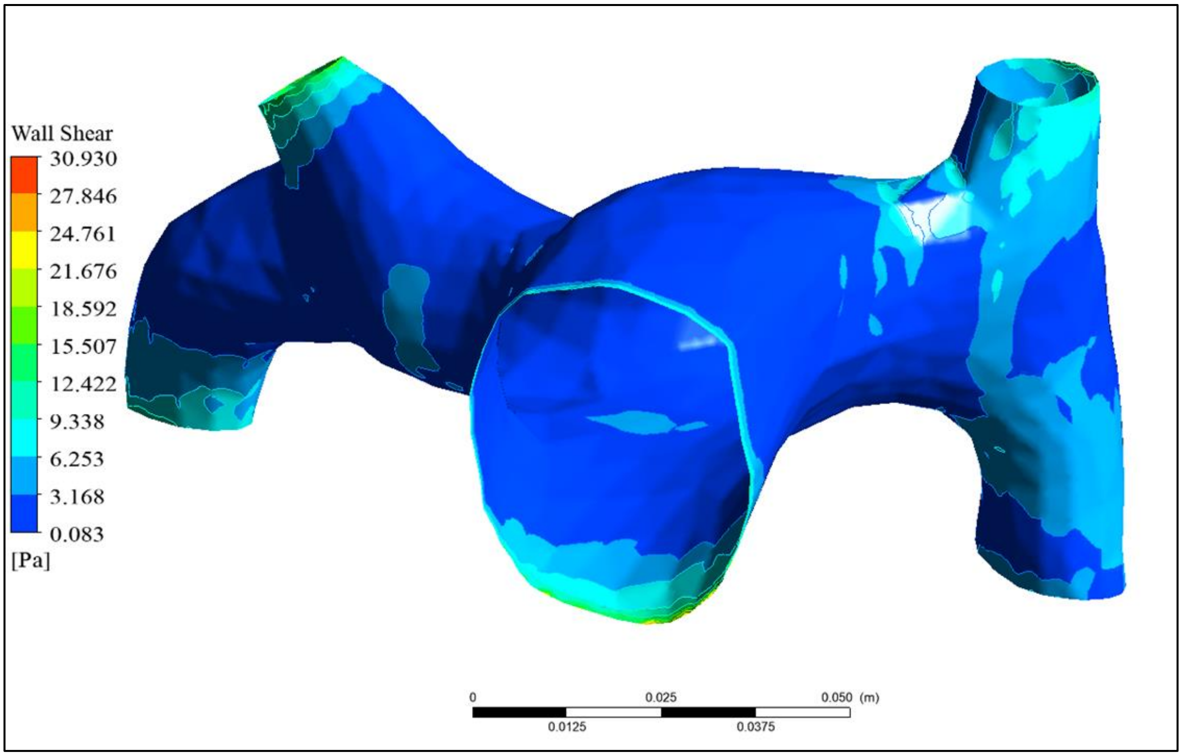

Figure 4.7 Wall shear stress contour for the steady-state rigid wall CFD model.

Figure 4.8, Figure 4.9, and Figure 4.10 contain velocity streamlines, velocity volume renderings, and the WSS contour for the steady-state linear elastic FSI model. In this model, the maximum and minimum velocities were 0.855 m/s and 0 m/s, respectively. This was a 31.5% increase in maximum velocity when compared to the steady-state CFD model that ignored vessel wall deformation. This model had a volume weighed average velocity (velocity normalized by the volume of the fluid element it was calculated for) of 0.231 m/s. The maximum WSS experienced in the steady-state linear elastic FSI model was 30.8 Pa, the minimum WSS was 0.0686 Pa, and the average was 3.74 Pa. The maximum WSS occurred at the model inlet and the minimum value occurred throughout the main PA, the RPA, and the LPA. With respect to the steady-state rigid wall CFD model, the linear elastic FSI model returned a maximum WSS that was only 0.325% smaller.

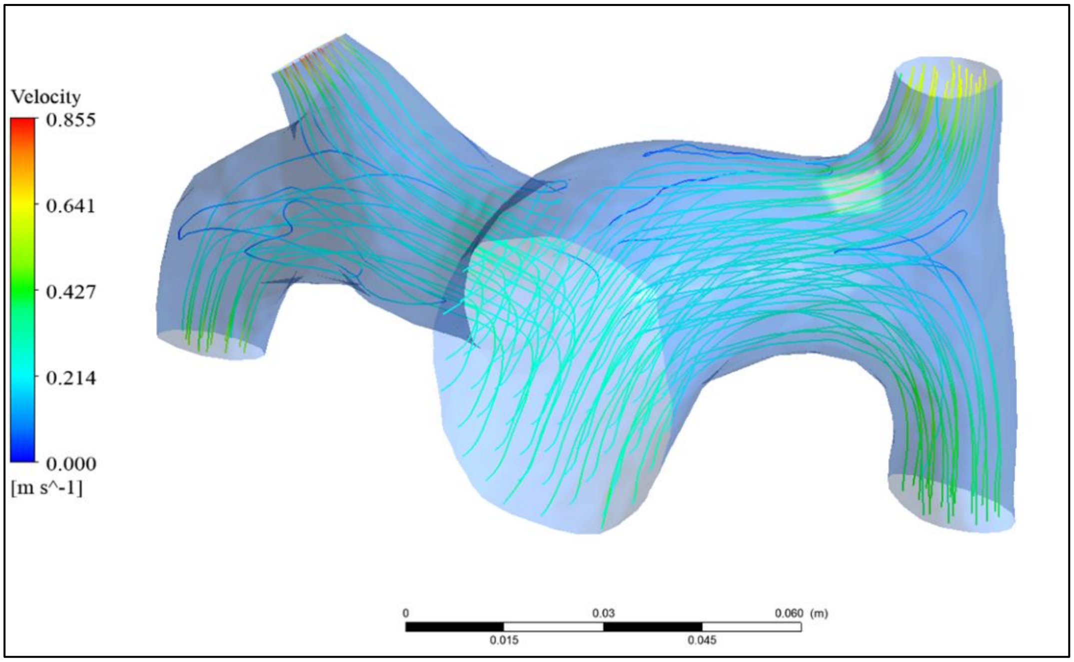

Figure 4.8. Velocity magnitude streamlines for the steady-state linear elastic (2 MPa) FSI model.

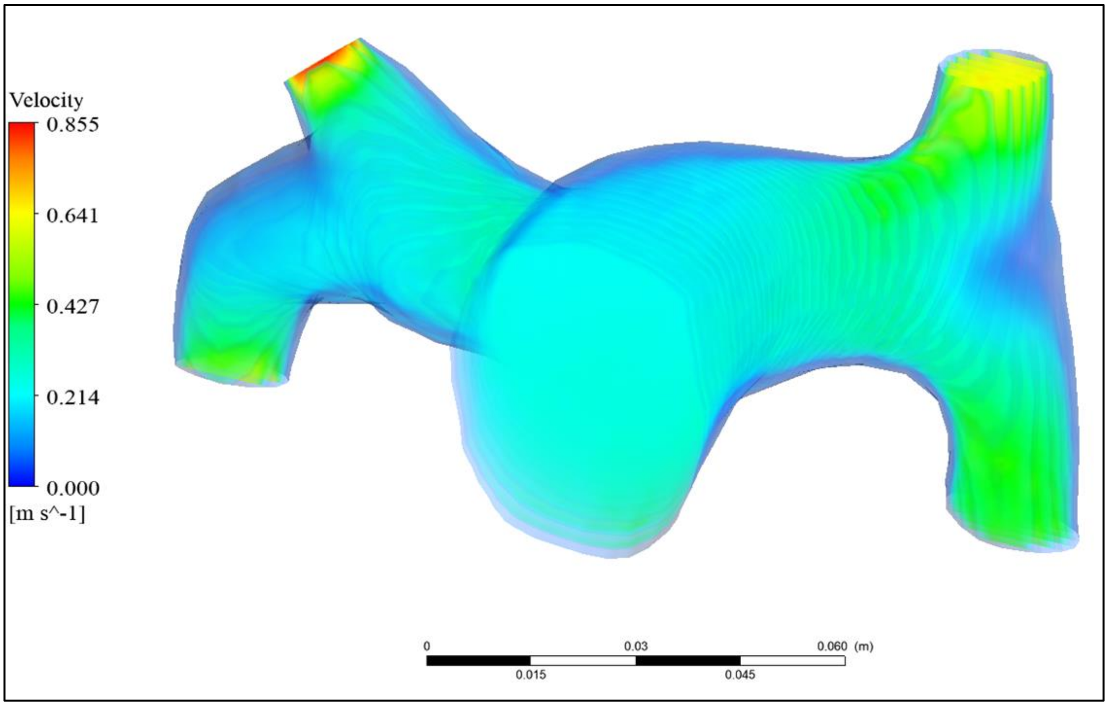

Figure 4.9. Velocity volume rendering for the steady-state linear elastic (2 MPa) FSI model.

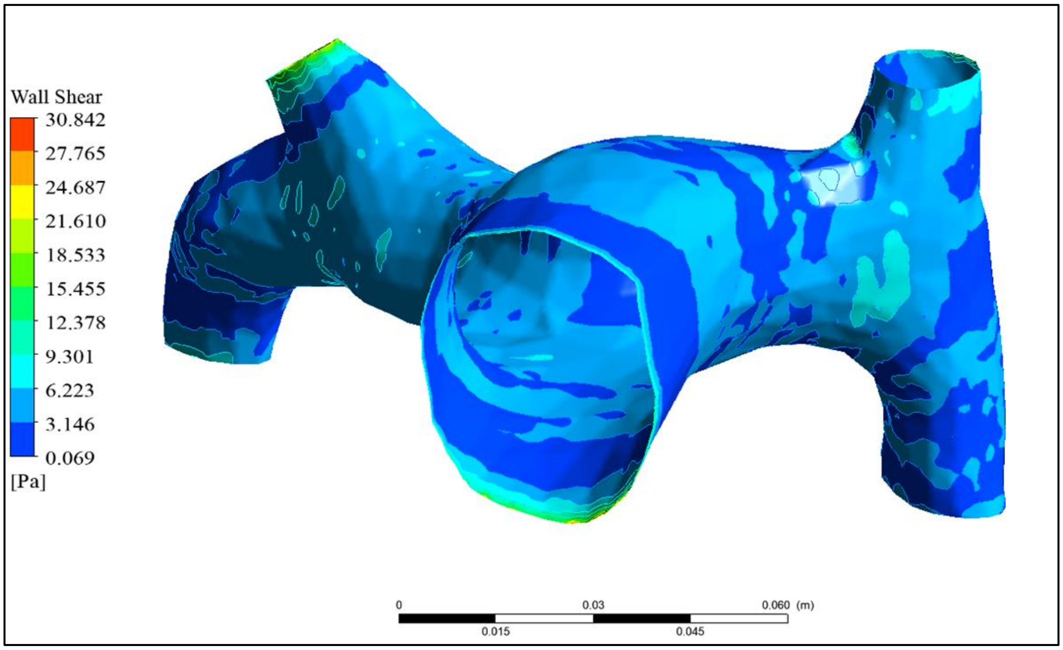

Figure 4.10. Wall shear stress contour for the steady-state linear elastic (2MPa) FSI model.

For the steady-state model using hyperelastic wall properties from Azadani et al. [113], a maximum velocity of 0.763 m/s, a minimum velocity of 0 m/s, and a volume weighted average velocity of 0.223 m/s were found. Compared to the maximum velocities for the rigid wall CFD model and the linear elastic FSI model, this was a 17.4% increase and a 10.7% decrease, respectively. The maximum and minimum WSS experienced at the walls of the steady-state hyperelastic FSI model were 30.3 Pa and 0.0990 Pa. This was a 1.94% and 1.62% decrease compared to the rigid wall CFD model and the linear elastic FSI model. As with the other models, the maximum WSS value occurred at the model inlet and the minimum values occurred throughout the trunk of the main PA, the RPA, and the LPA. An average WSS of 3.07 Pa was found. These results are shown below in Figure 4.11 (velocity streamlines), Figure 4.12 (velocity volume rendering), and Figure 4.13 (WSS contour.)

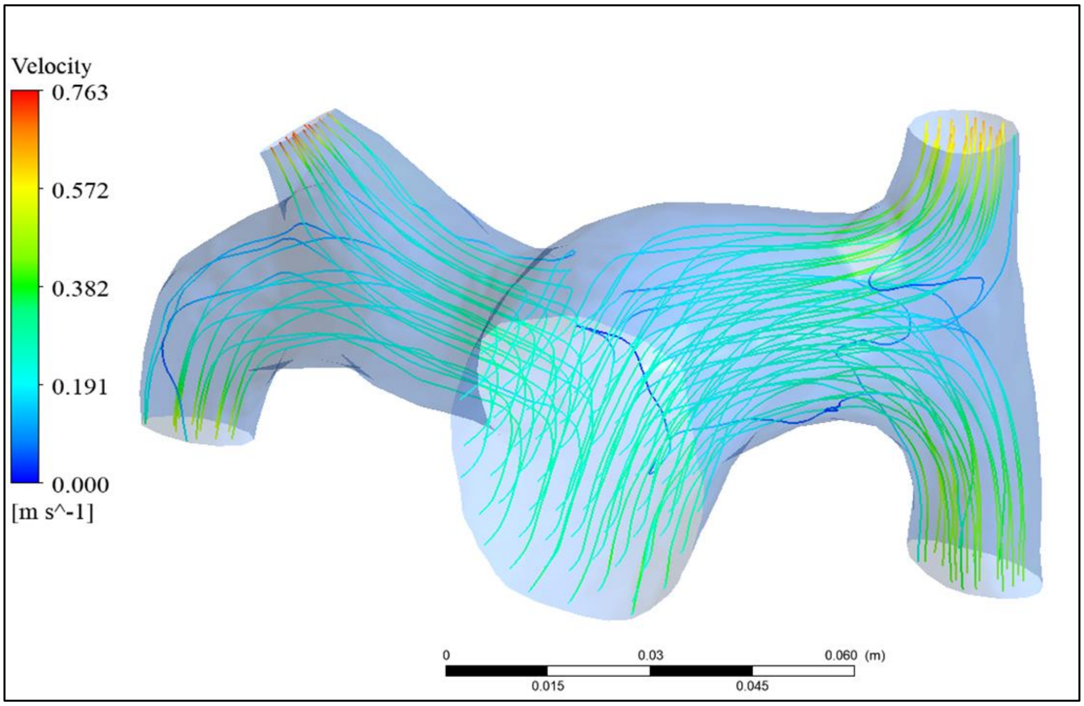

Figure 4.11. Velocity magnitude streamlines for the steady-state hyperelastic FSI model.

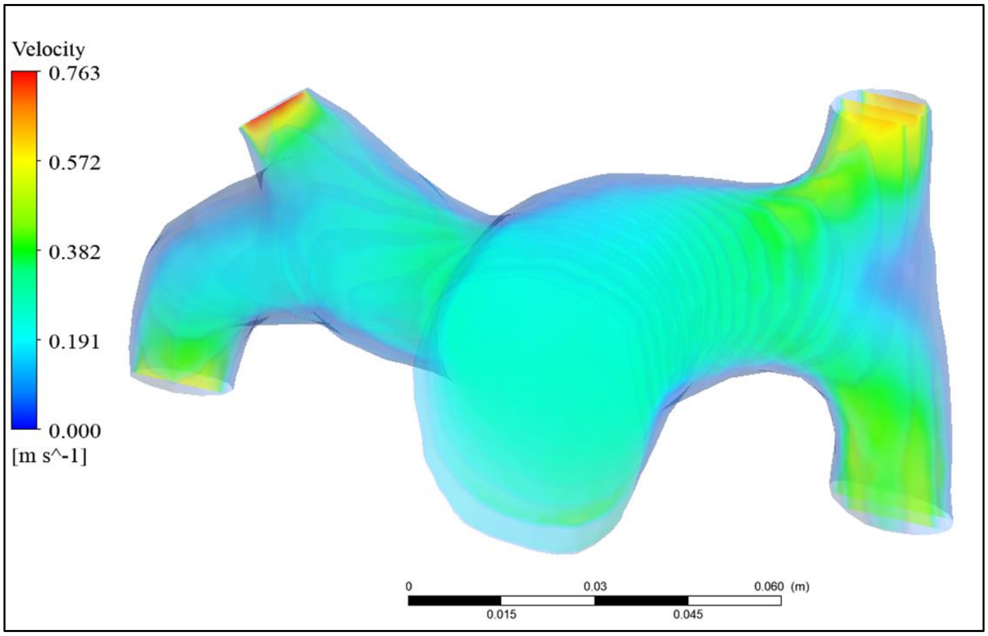

Figure 4.12. Velocity volume rendering for the steady-state hyperelastic FSI model.

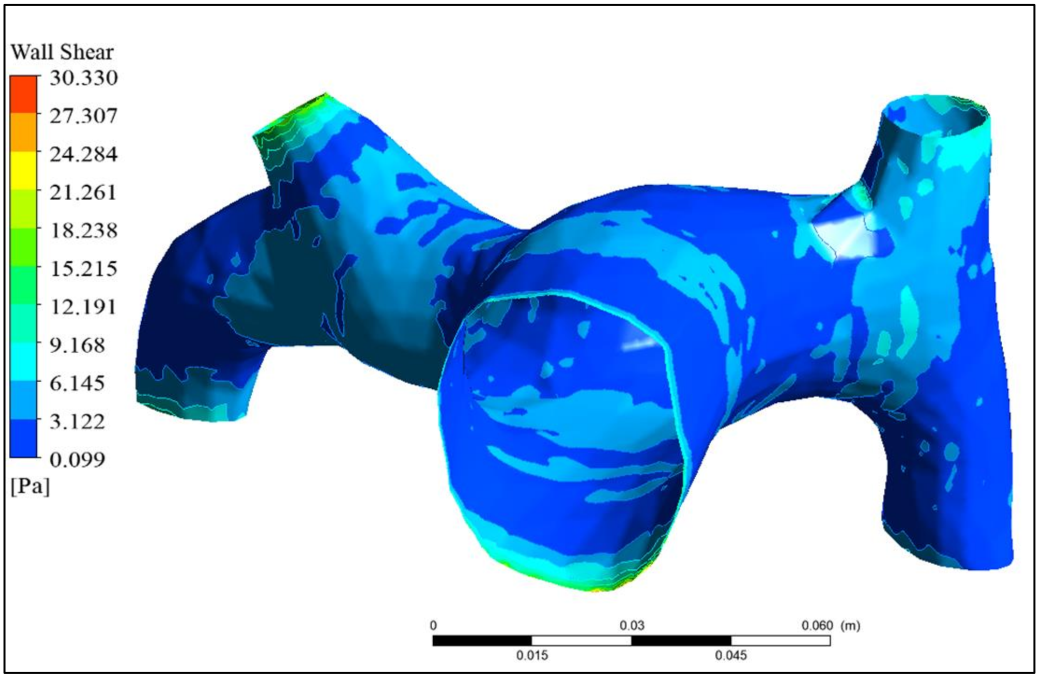

Figure 4.13. Wall shear stress contour for the steady-state hyperelastic FSI model.

For comparison of the fluid results for each steady-state model, velocity contours (Figure 4.14) at the midplane of the RPA, LPA, and MPA were created for each model. It is worth pointing out the lower velocities at the walls of the rigid wall CFD model.

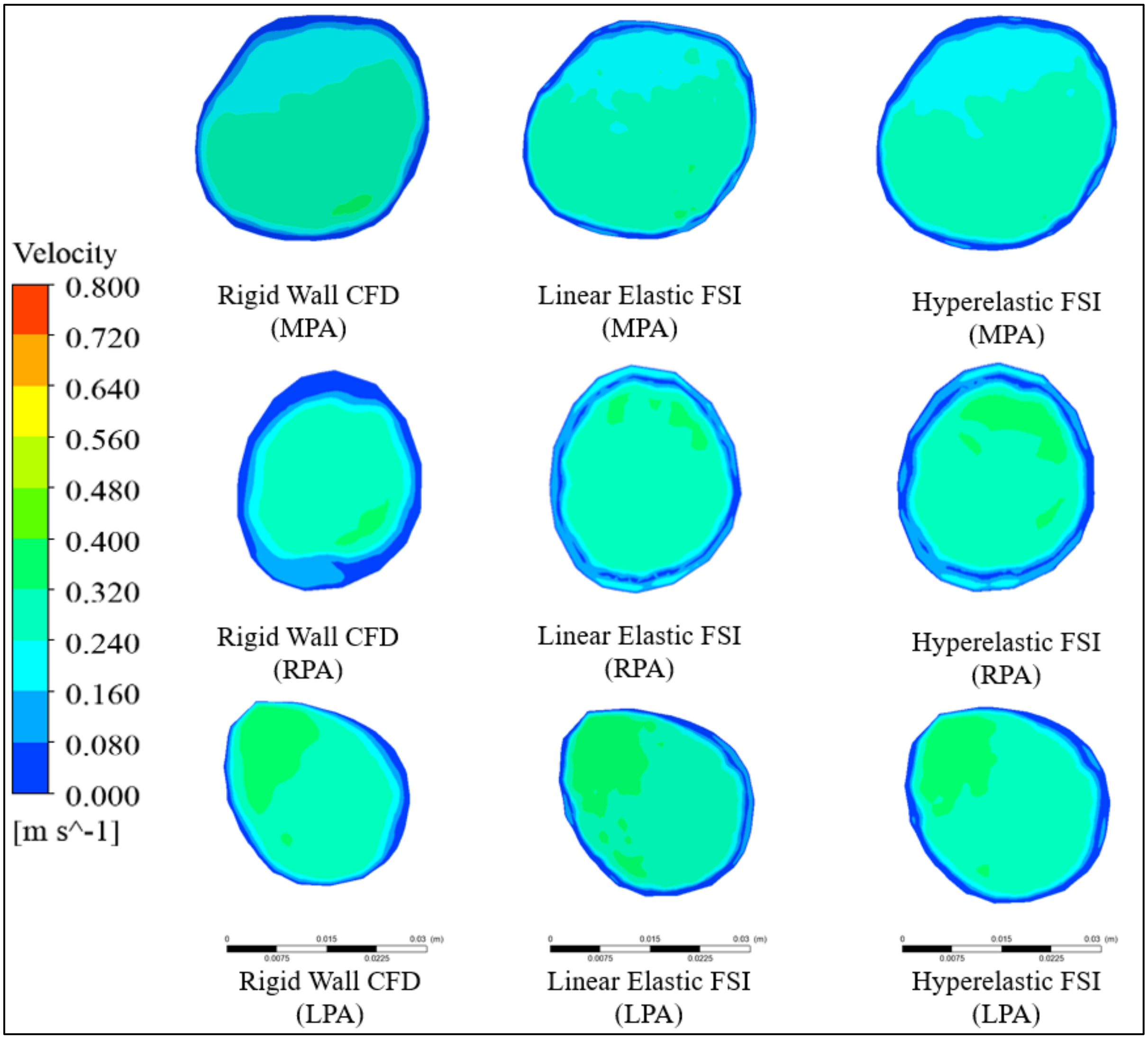

Figure 4.14. Midplane velocity contours for the steady-state rigid wall CFD model, linear elastic FSI model, and the hyperelastic FSI model.

4.5.2 Steady-State Solid Results

For the rigid wall CFD model, infinite wall stiffness was assumed. Therefore, total deformations, equivalent stresses, and equivalent strains are all unaccounted for throughout the model. In this model, walls were assumed to resist all ranges of pressure and stress.

For the steady-state linear elastic FSI model, a maximum deformation (Figure 4.15) of 0.27 mm was found. This deformation occurred on the inferior wall of the main PA. A maximum stress (von Mises; Figure 4.16) of 0.0117 MPa and a maximum strain (Figure 4.17) of 0.006 were also reported. These values also occurred on the inferior wall of the main PA; however, they were located in areas around the site of maximum deformation.

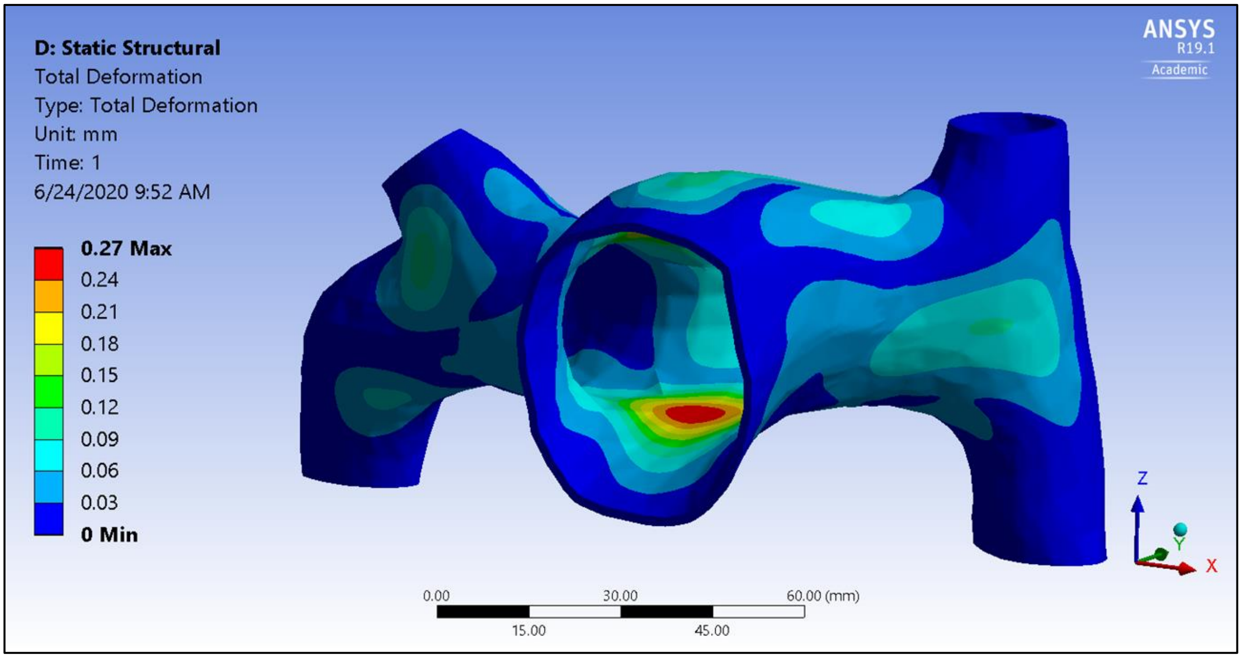

Figure 4.15. The deformation contour for the steady-state linear elastic FSI model.

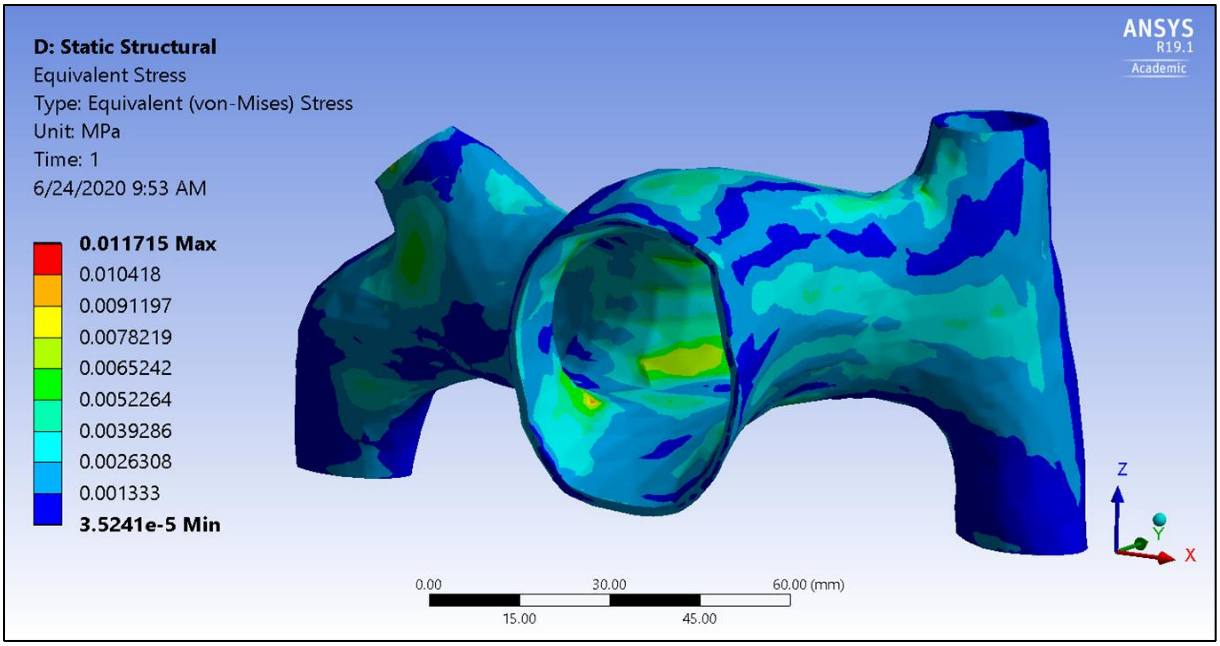

Figure 4.16. The equivalent stress (von Mises) contour for the steady-state linear elastic FSI model.

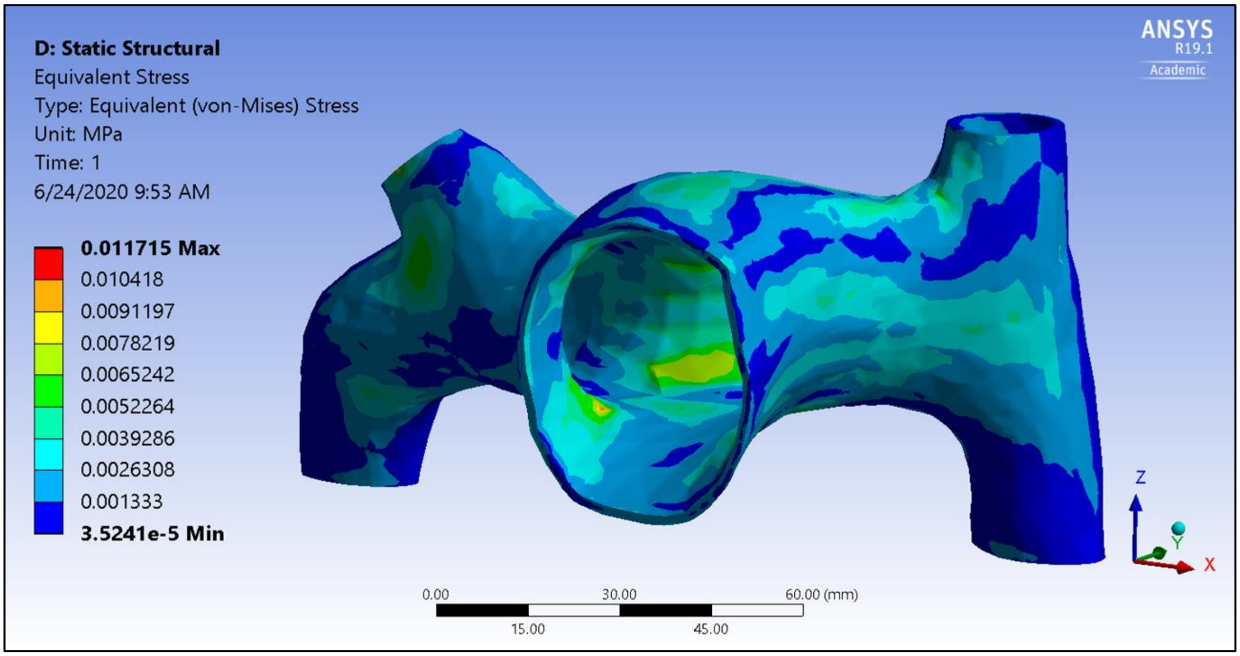

Figure 4.17. The strain contour for the steady-state linear elastic FSI model.

When the linear elastic wall modulus was changed to a hyperelastic material, a maximum deformation (Figure 4.18) of 1.62 mm, a maximum stress (Figure 4.19) of 0.00736 MPa, and a maximum strain (Figure 4.20) of 0.0448 were found. These contours are all given in figures on the subsequent pages. With respect to the linear elastic FSI model, the hyperelastic model predicted 500% more deformation, 37% less stress, and 640% more strain. These extrema still occurred at similar locations in each model.

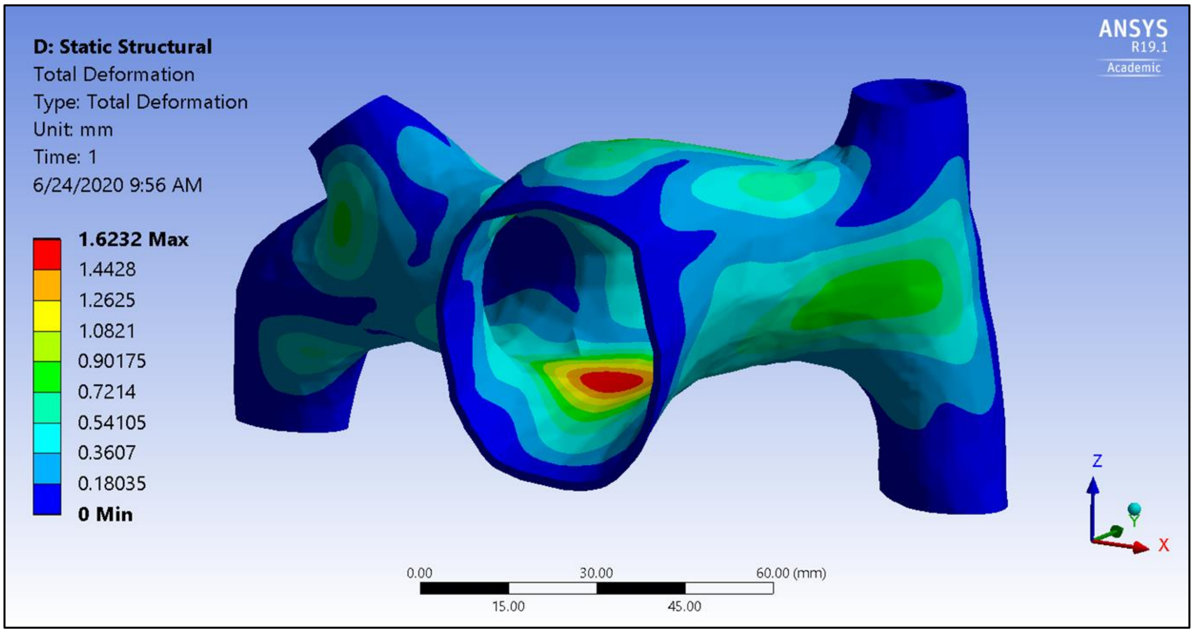

Figure 4.18. The deformation contour for the steady-state hyperelastic FSI model.

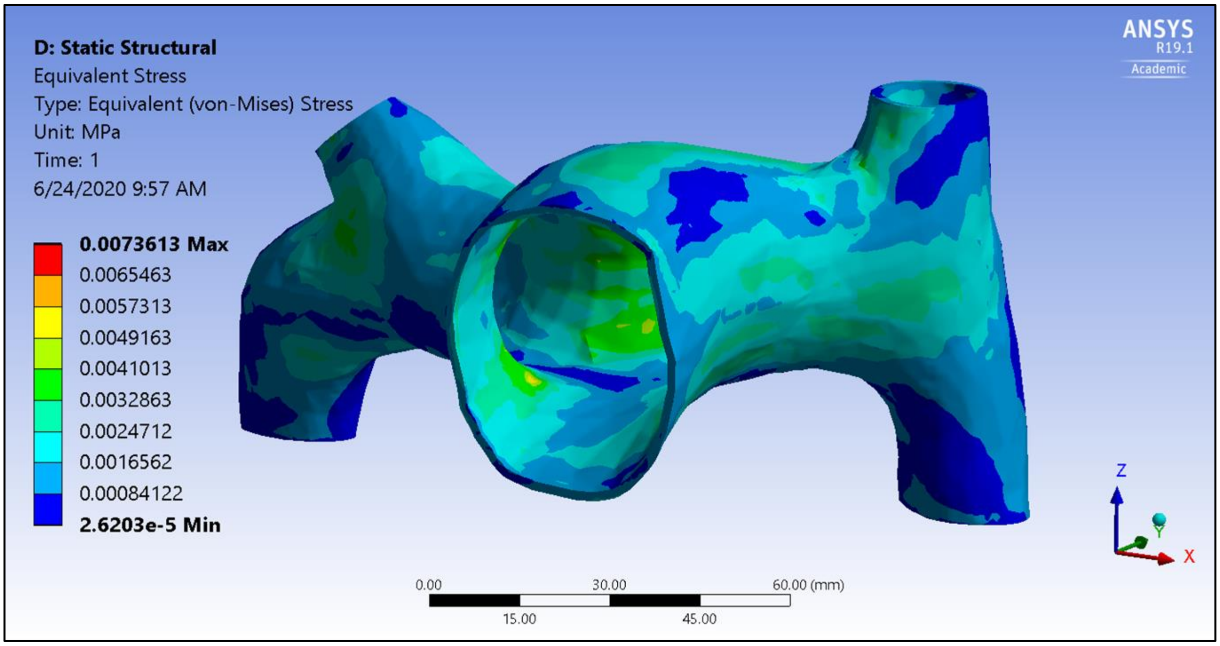

Figure 4.19. The equivalent stress (von Mises) contour for the steady-state hyperelastic FSI model.

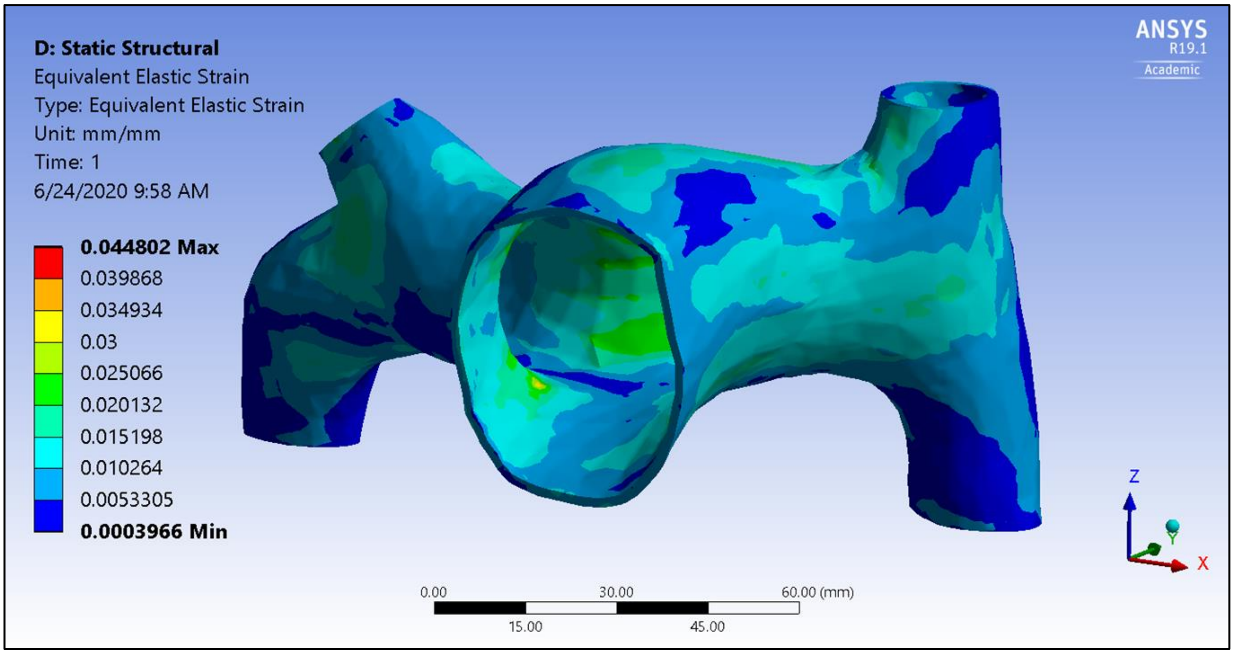

Figure 4.20. The strain contour for the steady-state hyperelastic FSI model.

4.6 Comparison of Steady-State Models

Given below, Table 4.4 provides a summary of significant results from all steady-state models run during the course of this project. Results include items discussed above, such as maximum velocities, wall shear stresses, and deformations, and other items that may be of interest to readers, such as the time taken to run each model until convergence was reached. It is worth noting how even though the maximum velocities varied in each steady-state model, maximum WSS values varied minimally. The differences in run time for each model, which varied from 27 minutes for the steady-state rigid wall CFD model up to 18 hours and four minutes for the steady-state hyperelastic FSI model, is also worth pointing out here. This run time was calculated using elapsed wall clock time, not CPU time, so as to provide a more realistic idea of the resources required to run the simulation to completion.

Table 4.4. Summary of steady-state model results.

	Steady-State CFD	Steady-State Linear FSI	Steady-State Hyperelastic FSI
Run Time (hh:mm)	0:27	2:40	18:04
Maximum Velocity (m/s)	0.650	0.855	0.763
Volume Weighted Average Velocity (m/s)	0.224	0.231	0.223
Maximum WSS (Pa)	30.930	30.842	30.330
Average WSS (Pa)	2.64301	3.74086	3.06821
Maximum Deformation (mm)	-	0.270	1.623
Average Deformation (mm)	-	0.0395	0.32913
Maximum Stress (MPa)	-	0.0117	0.00736
Average Stress (MPa)	-	0.00194	0.00163
Maximum Strain	-	0.00605	0.0448
Average Strain	-	0.00105	0.00942

4.7 Transient Models

This section contains results obtained from the transient FSI model and transient rigid wall CFD model run in ANSYS Workbench. Fluid results from FLUENT are discussed first, followed by results from ANSYS Mechanical. Since three cardiac cycles were simulated for each model and to limit redundancy of results, all figures were created using the second cardiac cycle for this patient. Average values across all cardiac cycles are given at the end of this chapter in Table 4.6.

4.7.1 Transient Fluid Results

The maximum velocity for the transient rigid wall CFD model was 0.725 m/s. This can be seen in Figure 4.21, given below. Although not entirely comparable to the steady-state results, this maximum value fell in between the maximum velocity values for the steady-state rigid wall CFD model and the steady-state linear elastic FSI model and was only 5% less than the maximum velocity of the steady-state hyperelastic FSI model. This difference is not surprising since the steady-state models were prescribed inlet velocities (0.2156 m/s) slightly lower than the maximum inlet velocity in the velocity waveforms utilized for the transient models (approximately 0.22 m/s). Across all three cardiac cycles, this model had an average maximum velocity of 0.731 m/s at peak systole and a volume weighted average velocity of 0.223 m/s at peak systole.

At peak systole, the maximum WSS in the transient rigid wall CFD model was 33.8 Pa. This maximum value was higher than the other extreme values found in the steady-state models. At the start of diastole, very small WSS values dominated the majority of the model. The minimum WSS found for this model was 0.0262 Pa. Across all three cardiac cycles, this model had an average maximum WSS value of 33.8 Pa and an average WSS value of 3.714 Pa. These results can be seen below in Figure 4.23.

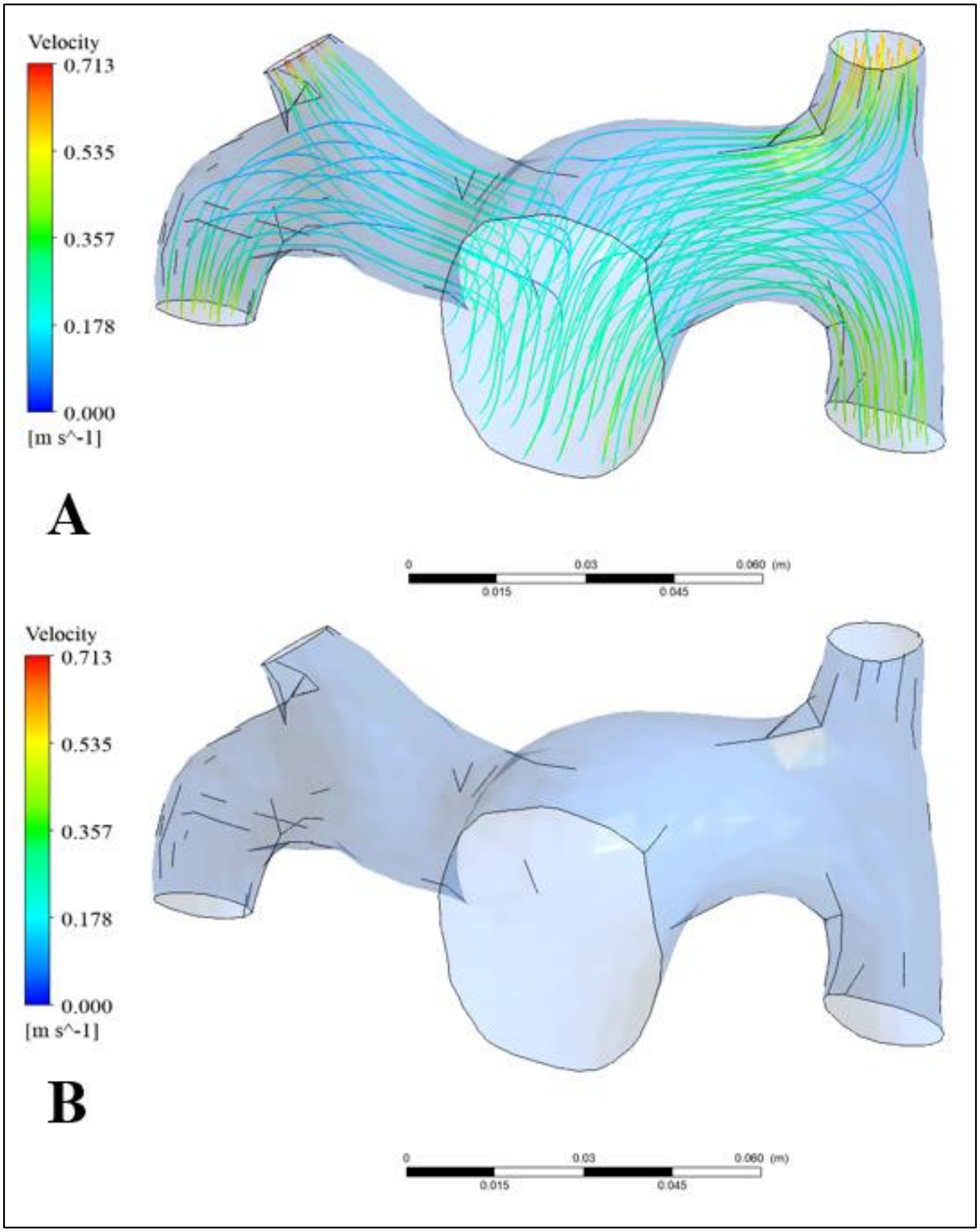

Figure 4.21. Velocity magnitude streamlines for the transient rigid wall CFD model at (A) peak systole and (B) the start of diastole.

Almost no flow occurred at the start of diastole, resulting in no streamlines.

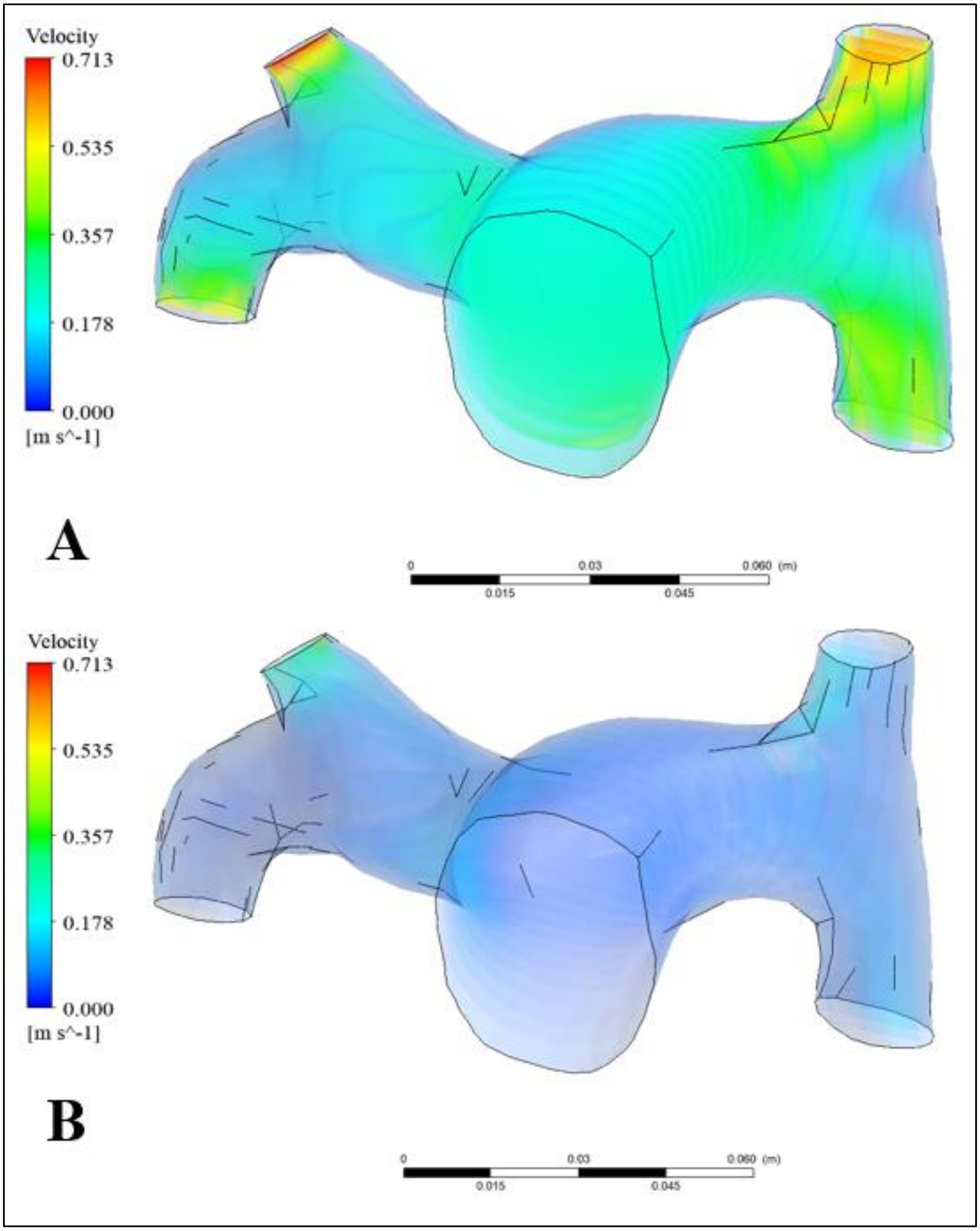

Figure 4.22. Velocity volume renderings for the transient rigid wall CFD model at (A) peak systole and (B) the start of diastole.

Almost no flow was occurring at the start of diastole, hence the lack of faster moving fluid throughout the majority of the PA.

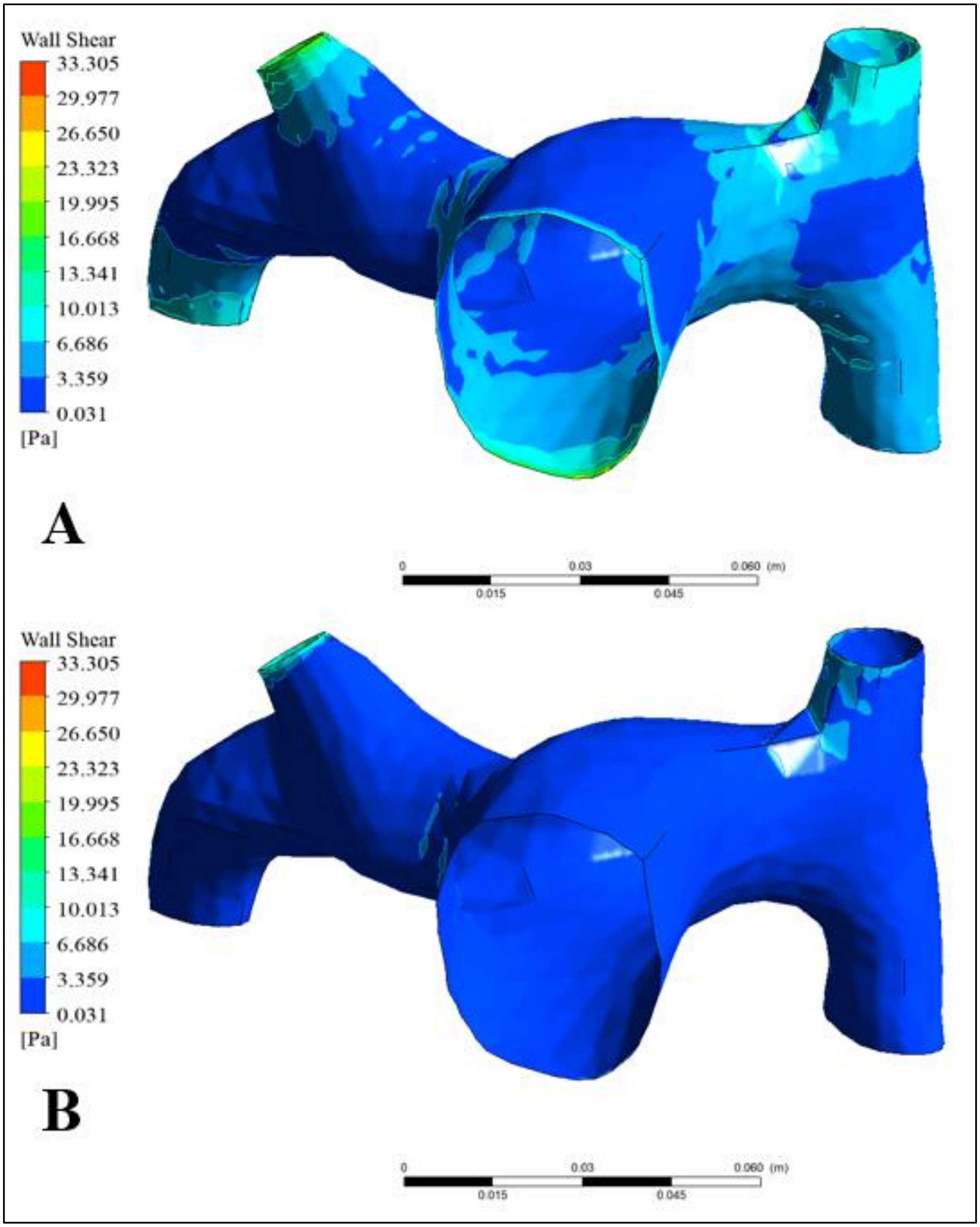

Figure 4.23. Wall shear stress contours for the transient rigid wall CFD model at (A) peak systole and (B) the start of diastole.

For the transient linear elastic FSI model, a maximum velocity (Figure 4.24 and Figure 4.25) of 0.733 m/s was found. This maximum value is only 1% larger than the maximum velocity in the transient rigid wall CFD model. Likewise, the maximum WSS at peak systole for the linear elastic FSI model was 33.9 Pa and was nearly identical to the maximum value at peak systole for the rigid wall CFD model. The WSS contours for the transient linear elastic FSI model can be seen below in Figure 4.26. Across all three cardiac cycles, this model had an average peak systolic maximum velocity of 0.736 m/s, a peak systolic volume weighted average velocity of 0.226 m/s, a peak systolic average maximum WSS value of 33.9 Pa, and an average WSS value of 3.62 Pa. The majority of these values were less than 1% different than the values found in the transient CFD model. The only value that had a percent different greater than 1% between the two models was the volume weighted average velocity; the transient linear elastic FSI model had a peak systolic volume weighted average velocity that was 1.3% larger than the transient CFD model across the simulated cardiac cycles.

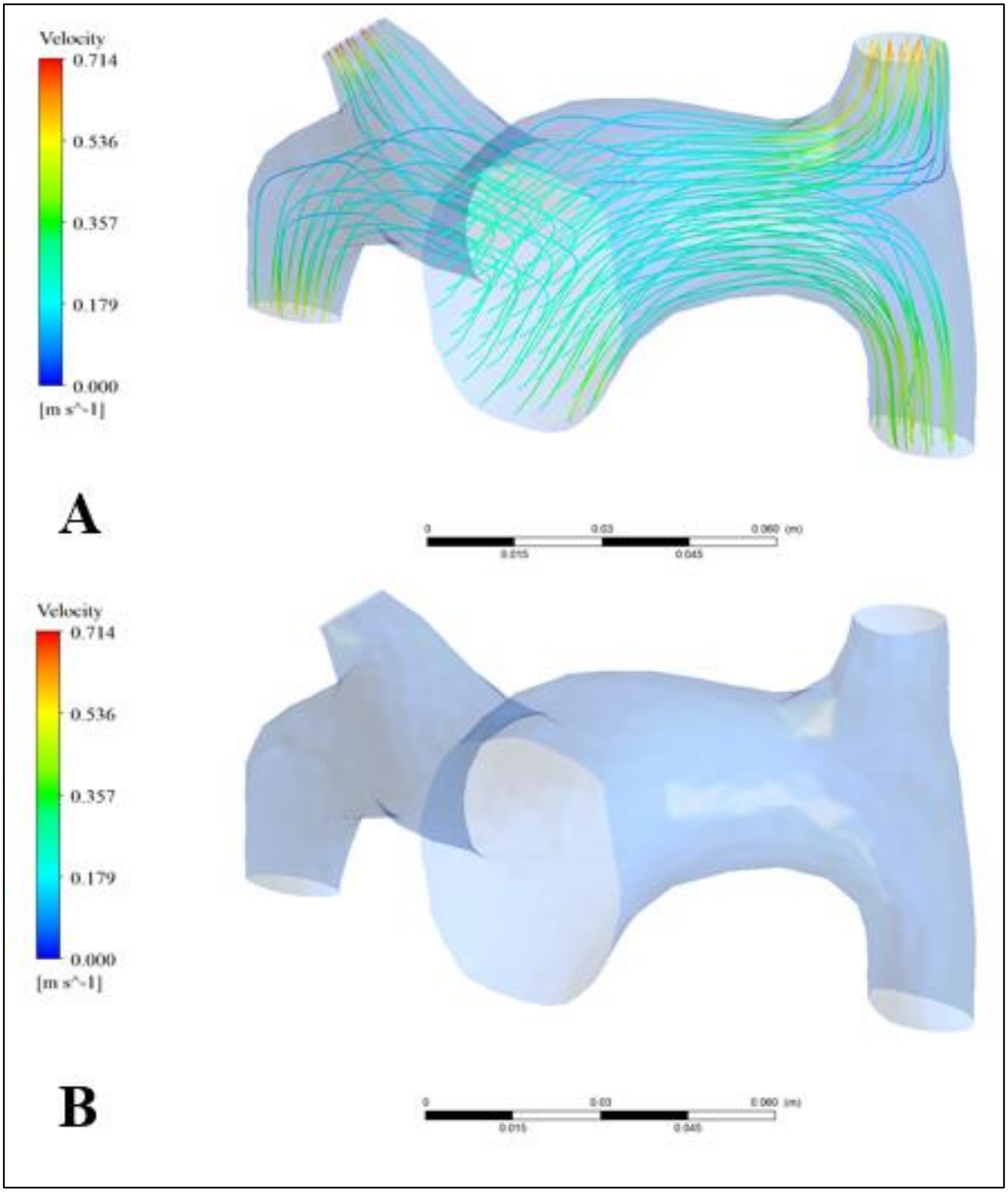

Figure 4.24. Velocity magnitude streamlines for the transient linear elastic FSI model at (A) peak systole and (B) the start of diastole.

Almost no flow was occurring at the start of diastole, hence the lack of streamlines.

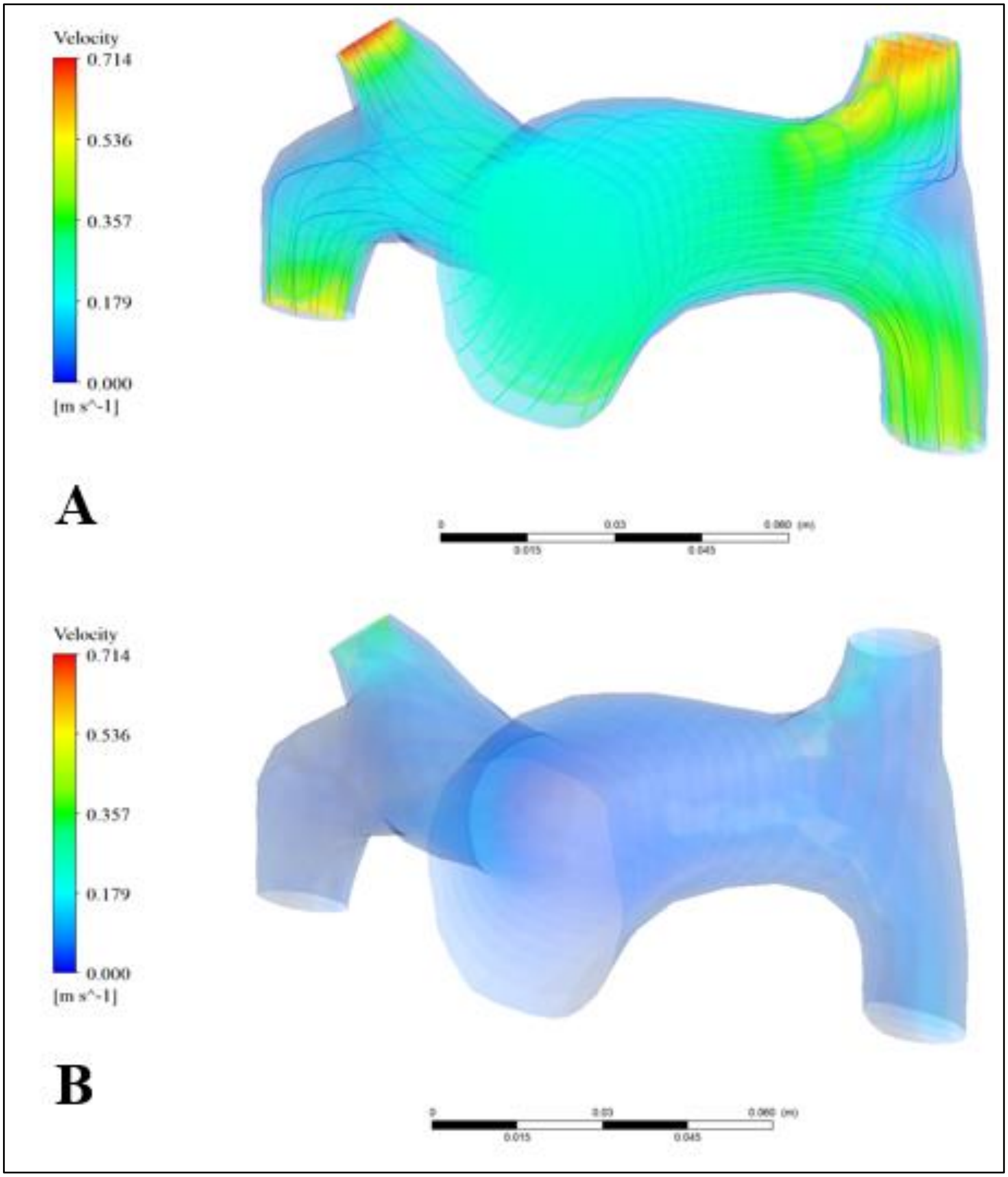

Figure 4.25. Velocity volume renderings for the transient linear elastic FSI model at (A) peak systole and (B) the start of diastole.

Almost no flow was occurring at the start of diastole, hence the lack of faster moving fluid throughout the majority of the PA.

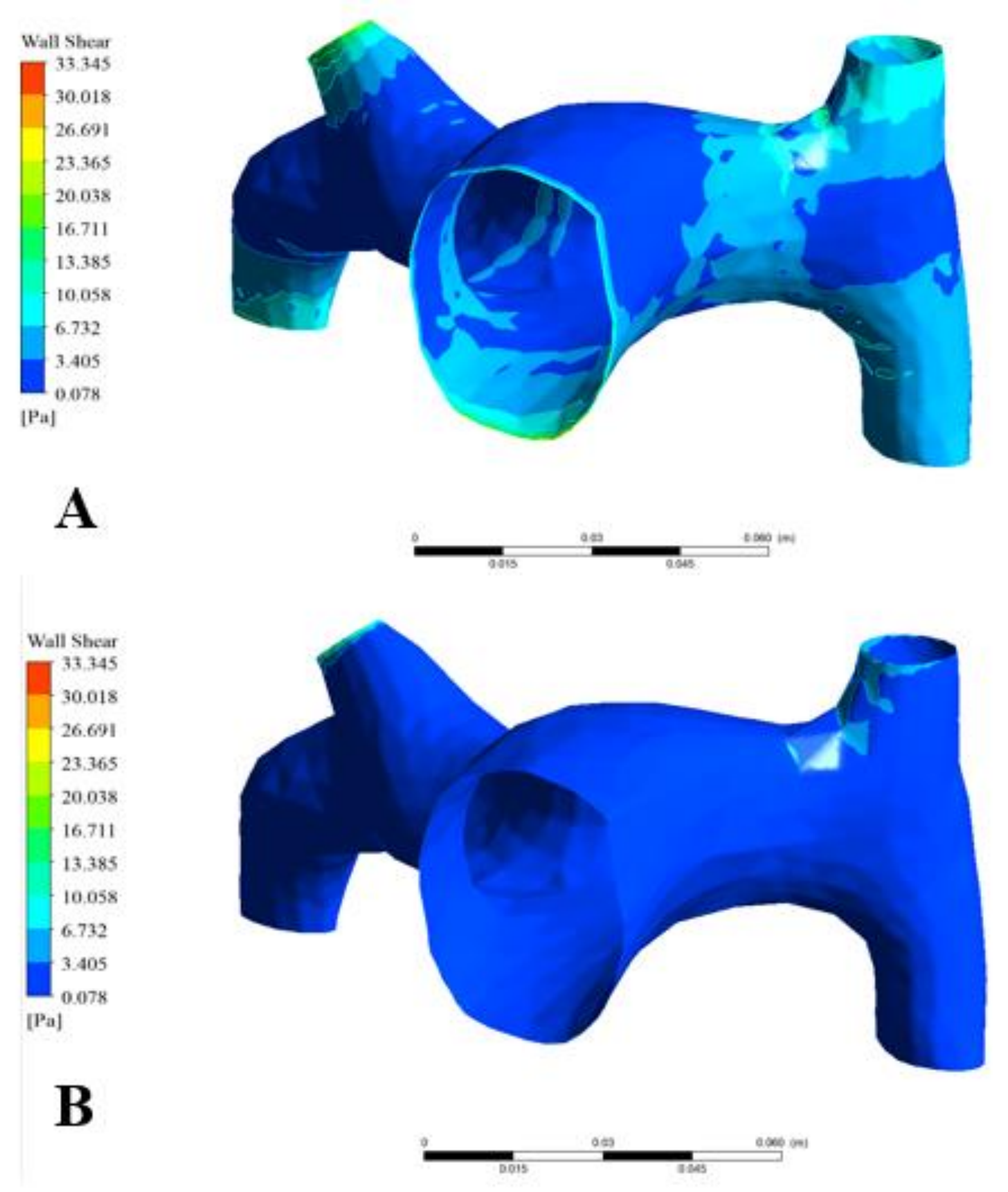

Figure 4.26. Wall shear stress contours for the transient linear elastic FSI model at (A) peak systole and (B) the start of diastole.

Given below, Figure 4.27 compares cross-sectional velocity contours at the midplane of the RPA, LPA, and MPA for the two transient models run in this study. This velocity contours were created using the velocity results at peak systole. Additionally, Figure 4.28 and Figure 4.29 highlight the differences between the maximum WSS values and the average WSS values for the transient rigid wall CFD model and the transient linear elastic FSI model. The transient CFD model returned an average time-averaged WSS value of 1.48 Pa (14.78 dyn/cm^2) throughout the third cardiac cycle, whereas the transient FSI model returned a time-averaged WSS value of 1.44 Pa (14.4 dyn/cm^2). These time-averaged WSS values are close to those presented in earlier studies, such as Rabidou and George [60] and Tang et al. [64]; however, the values calculated here are slightly higher than both studies. They are most similar to Tang et al. [64], who found their PH patients had time-averaged WSS values of 4.3 ± 2.8 dyn/cm^2.

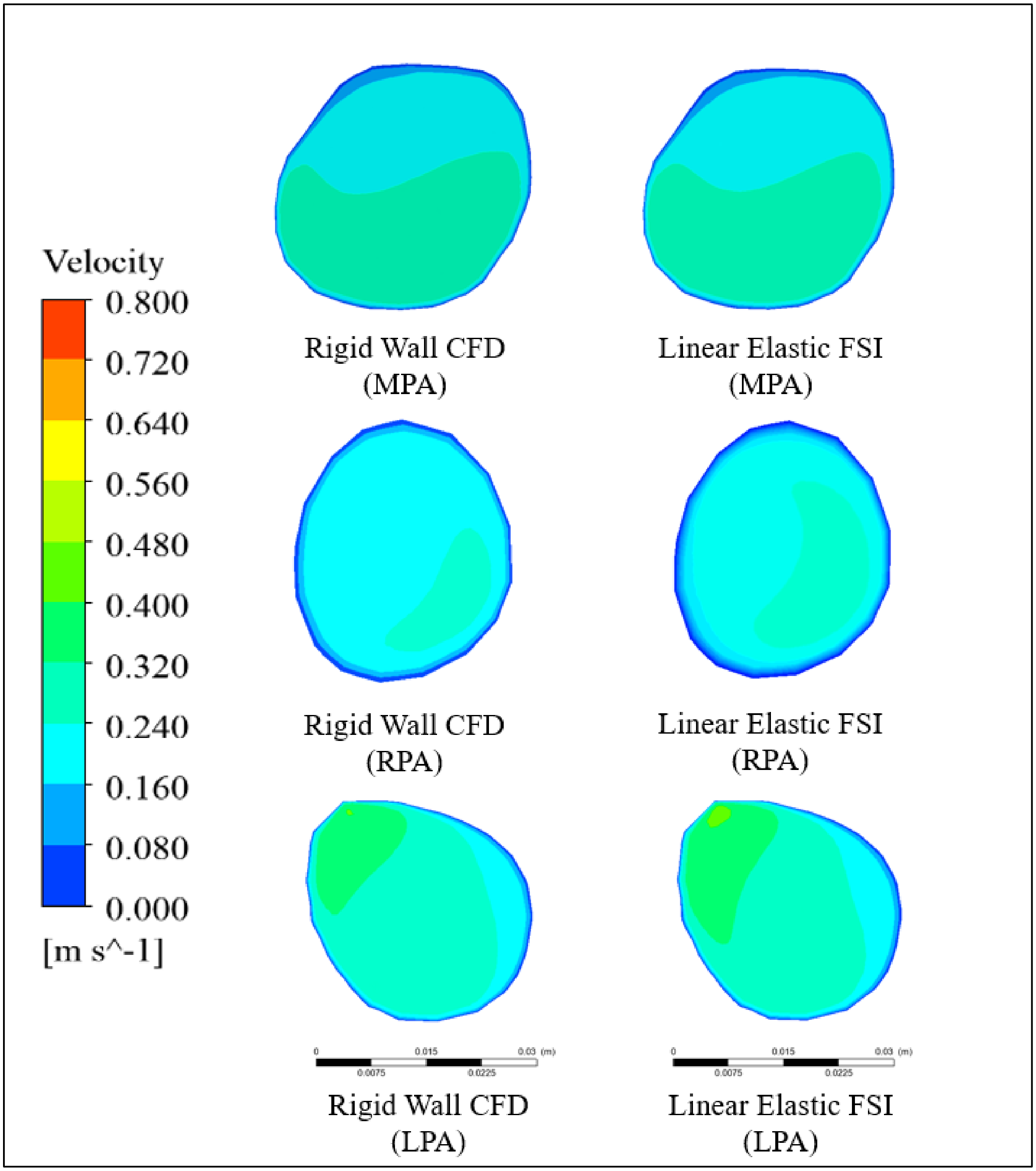

Figure 4.27. Midplane velocity contours for the transient rigid wall CFD and linear elastic FSI model.

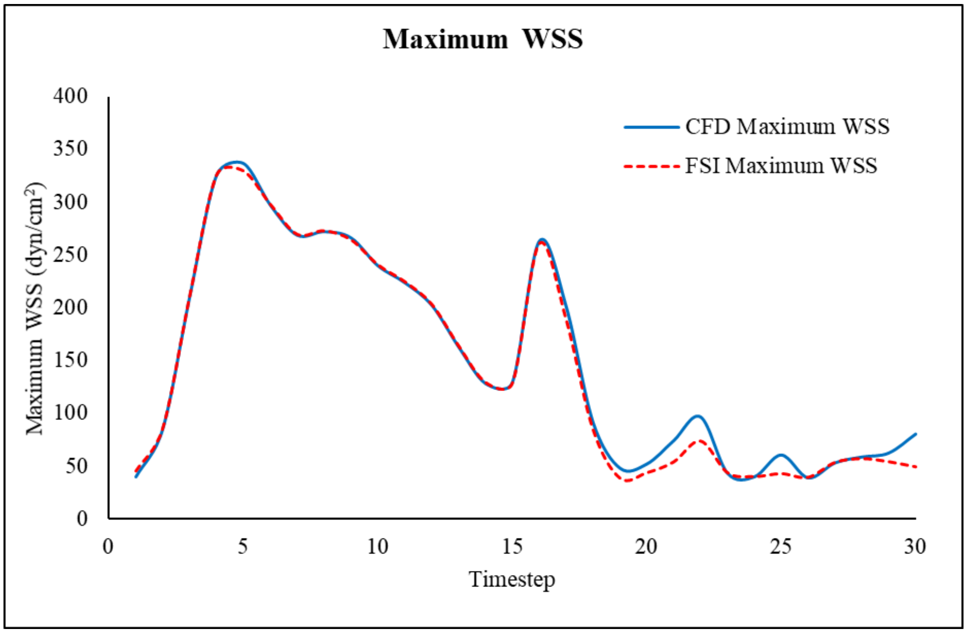

Figure 4.28. Maximum WSS values throughout the fluid domain for one cardiac cycle.

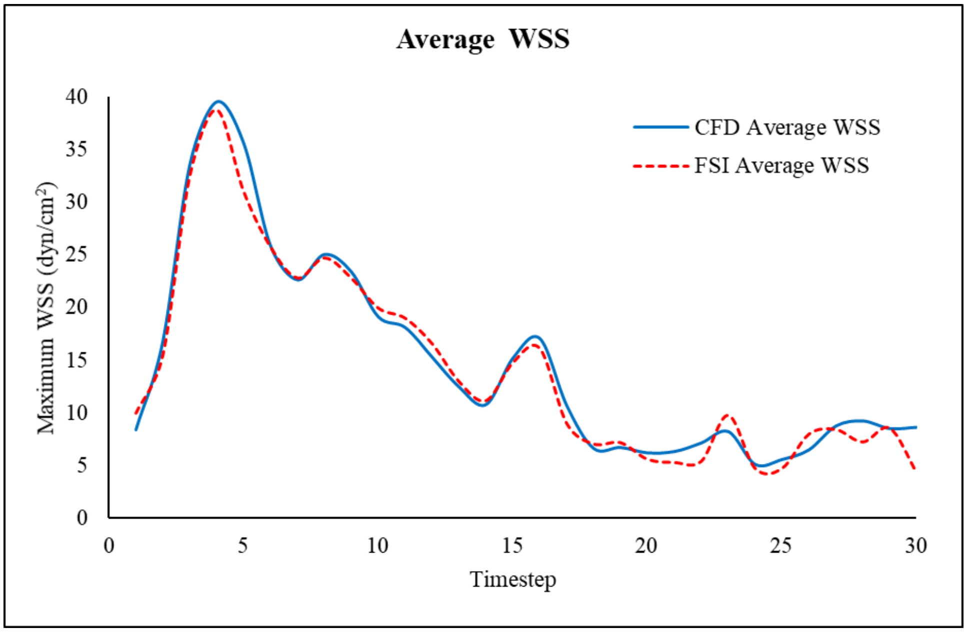

Figure 4.29. Average WSS values throughout the fluid domain for one cardiac cycle.

4.7.2 Transient Solid Results

As aforementioned, the rigid wall CFD model assumed an infinite stiffness for the walls of the pulmonary. No deformation, stress, and strain values were available to present for this model. For the transient linear elastic model, a maximum deformation of 0.05 mm was calculated at peak systole. At the start of diastole, a maximum deformation of 0.03 mm was calculated. These deformations both occurred at the same spot; however, the deformations occurred in different directions. This can be seen in Figure 4.30, where the deformation at peak systole takes place in the inferior direction and the deformation at the start of diastole occurs in the superior direction. At peak systole, the PA model experienced a maximum stress (von Mises) of 0.03 MPa and a maximum strain of 0.0013. At the start of diastole, the model experienced a maximum stress of 0.013 MPa and a maximum strain of 0.0007. Stress and strain contours are given below in Figure 4.31 and Figure 4.32. These are relatively low deformations, stresses, and strains given that the model was roughly 140 mm wide when measured from the lateral wall of RPA to the lateral wall of LPA and had a consistent wall thickness of 1.5 mm [113]. Interestingly enough, the maximum deformation experienced throughout the simulated cardiac cycles occurred slightly before peak systole. For thoroughness, this deformation contour is shown in Figure 4.33.

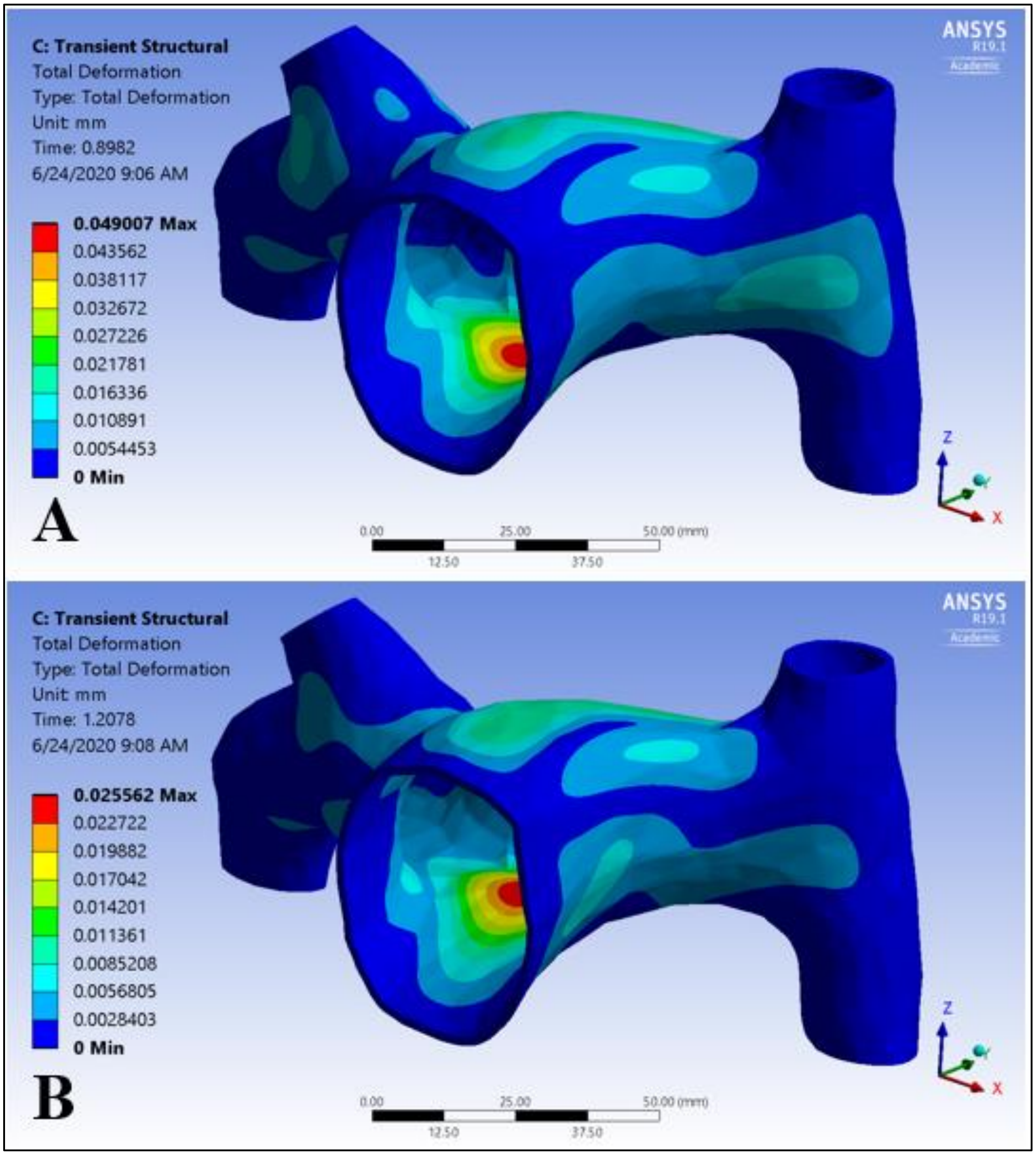

Figure 4.30. Deformation contours for the transient linear elastic FSI model at (A) peak systole and (B) the start of diastole.

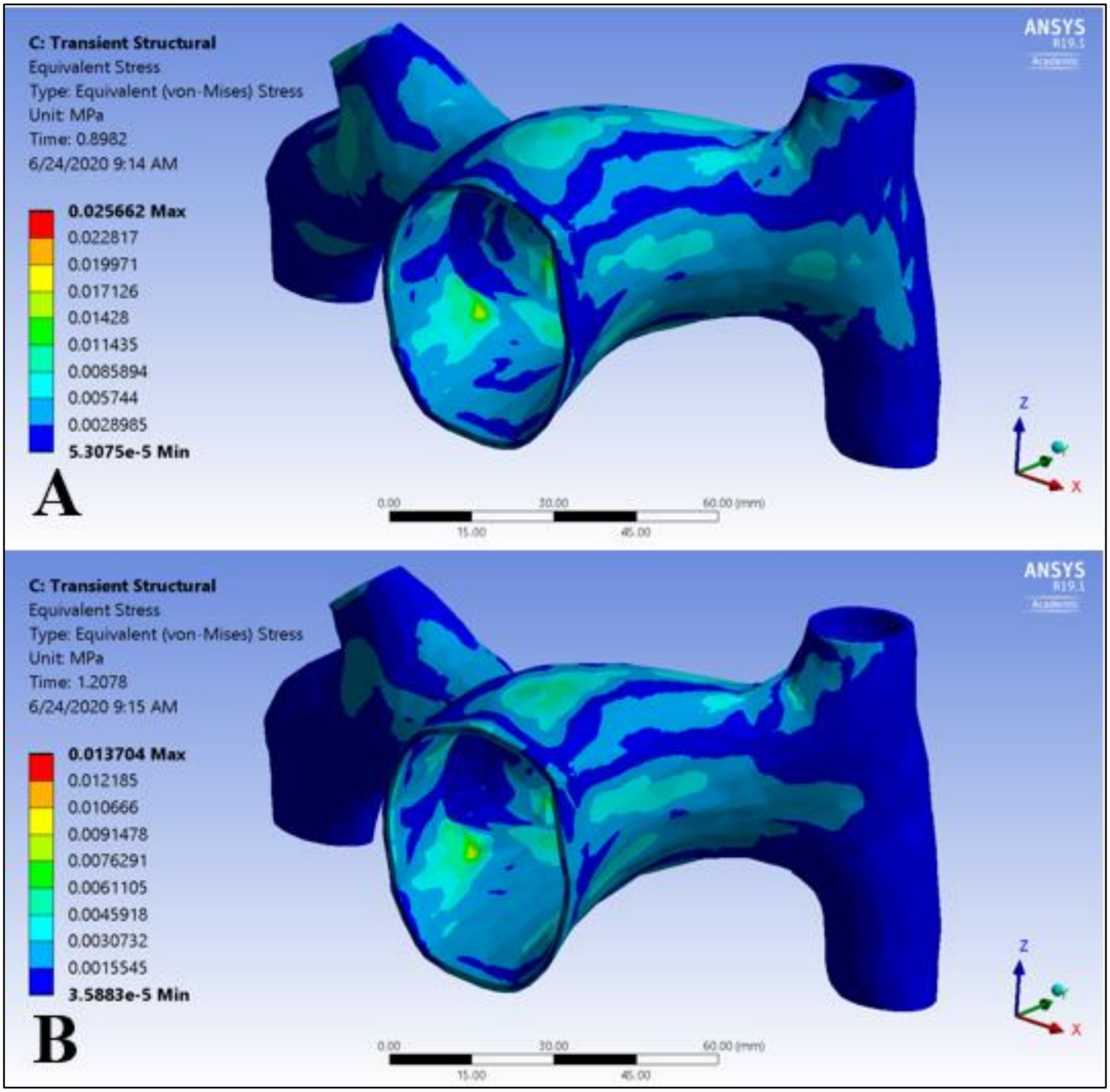

Figure 4.31. The equivalent stress (von Mises) contours for the transient linear elastic FSI model at (A) peak systole and (B) the start of diastole.

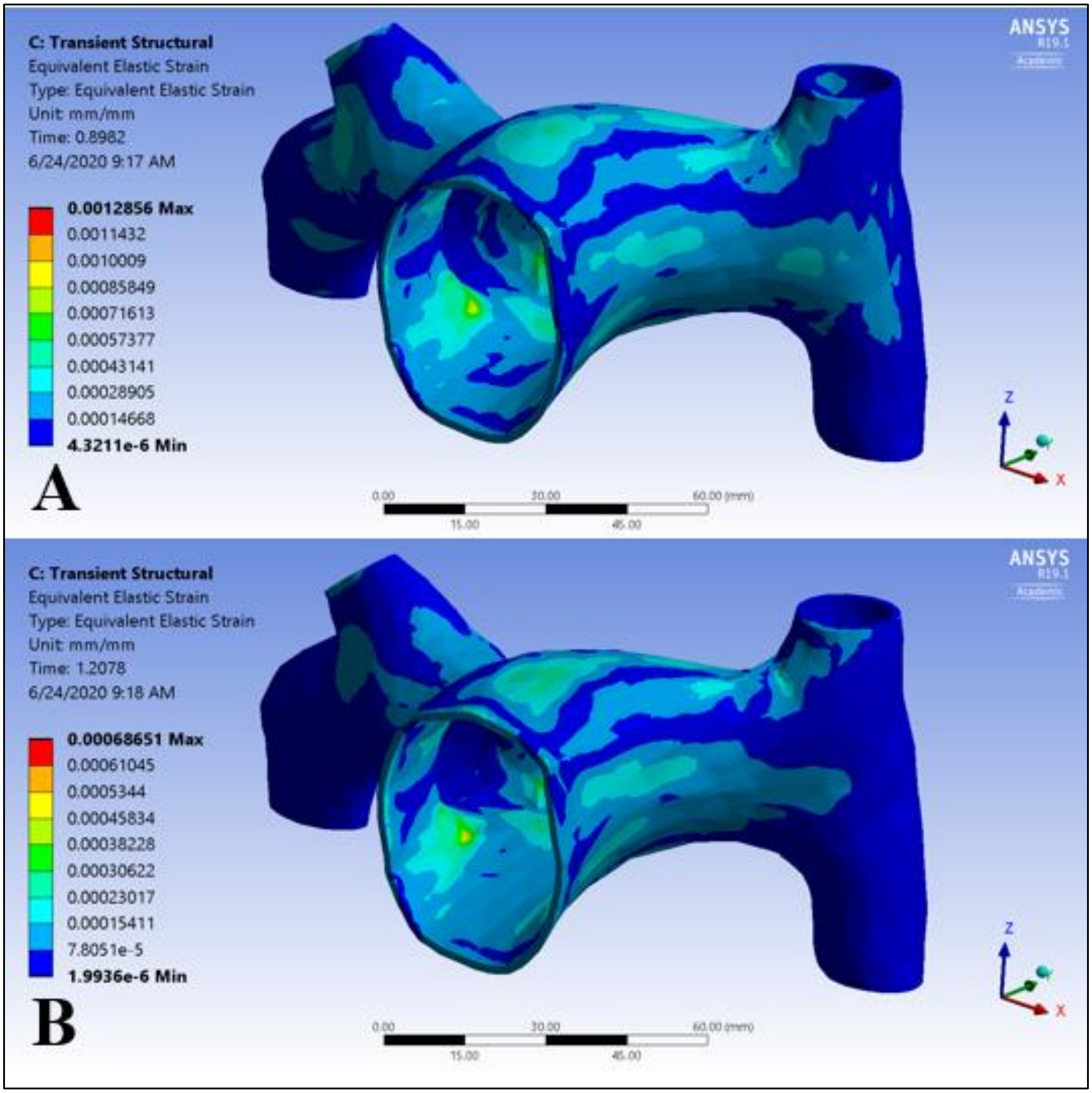

Figure 4.32. The strain contours for the transient linear elastic FSI model at (A) peak systole and (B) the start of diastole.

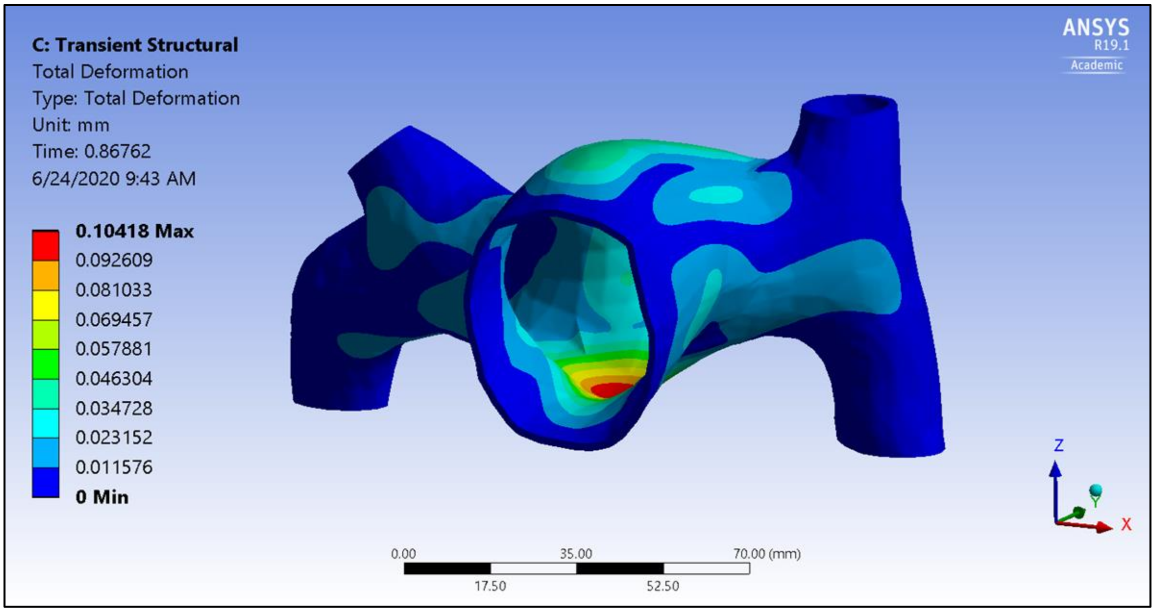

Figure 4.33. Maximum deformation experienced throughout the simulated cardiac cycles for the transient linear elastic FSI model. This deformation occurred slightly before peak systole.

4.8 Comparison of Transient Models

Table 4.5 (FLUENT) and Table 4.6 (Mechanical) include results from all transient models run during the course of this project. Minimal differences in maximum velocity and maximum WSS at peak systole were found between the two different transient models discussed here. Additionally, the difference in run time between the two models was surprising given the resemblance of the final results. It took over 16 times longer to run the transient linear FSI model using the resources mentioned in Section 3.13.

Table 4.5. Summary of transient model fluid results. Results taken at peak systole.

	Cardiac Cycle	Maximum Velocity (m/s)	Volume Weighted Average Velocity (m/s)	Maximum WSS (Pa)	Average WSS (Pa)
Transient CFD (Run Time: 6:18)	1	0.743	0.222	33.842	3.747
	2	0.725	0.223	33.815	3.690
	3	0.726	0.223	33.821	3.706
	Average	**0.731**	**0.223**	**33.826**	**3.714**
Transient Linear FSI (Run Time: 102:39)	1	0.742	0.226	33.882	3.631
	2	0.733	0.226	33.860	3.613
	3	0.733	0.226	33.860	3.614
	Average	**0.736**	**0.226**	**33.867**	**3.619**

As stated above, Table 4.6 includes a summary of relevant mechanical results from the transient linear elastic FSI model. Run time for this model is given above. Since the transient CFD model ignored deformation of the vessel wall, it has been omitted from this table.

Table 4.6. Summary of transient model mechanical results. Results taken at peak systole.

	Cardiac Cycle	Maximum Deformation (mm)	Average Deformation (mm)	Maximum Stress (MPa)	Average Stress (MPa)	Maximum Strain	Average Strain
Transient Linear FSI	1	0.0498	0.00651	0.0261	0.00301	0.00131	0.000161
	2	0.0490	0.00640	0.0257	0.00296	0.00129	0.000159
	3	0.0492	0.00643	0.0258	0.00297	0.00129	0.000159
	Average	**0.0493**	**0.00645**	**0.0258**	**0.00298**	**0.00129**	**0.00016**

CHAPTER 5. DISCUSSION

Chronic kidney disease affects over 15% of the adult US population and can progress to ESRD if not properly managed and addressed [1]. While hemodialysis via a surgically-created arteriovenous fistula effectively filters impure blood and helps compensate for renal failure, evidence has recently suggested connections between hemodialysis, increased pressures on the right side of the heart and in the pulmonary artery, and the subsequent development of PH [3]–[6]. Once PH develops, ESRD patients suffer a continual decrease in their quality of life and are removed from kidney transplant lists, leaving them with hemodialysis, severe lifestyle changes, and palliative care as their only clinical options. Increasing prevalence of ESRD cases have been reported in recent years and, unfortunately, have disproportionately affected African Americans, Hispanics, and the elderly at disparate rates [2].

Numerous studies have been conducted to improve screening and monitoring options for patients with PH. Studies by Tang et al. [64], [94] and Rabidou and George [60] utilized CFD to non-invasively quantify blood flow through the PAs of both normotensive and hypertensive patients. Both groups found decreased levels of WSS in PH patients. Other studies, such as Kong et al. [95] and Zambrano et al. [97], have accounted for deformation of the PA walls in their models. Unfortunately, Kong et al. [95] analyzed only one normotensive in their study, which was primarily aimed at constructing a monolithic fully-coupled two-way FSI, and used a linear elastic modulus of 4×10^6 g/cm.s^2. Zambrano et al. [97] compared a hypertensive and normotensive patient in their study, but also used a linear elastic modulus of 2 MPa for the walls of the PA. Given that human arteries do tend to deform in a non-linear manner, it was unclear whether or not a hyperelastic wall model would provide more accurate and clinically relevant results. It was also unclear if wall interactions play a significant role in fluid flow patterns in the PA. Since FSI modeling requires more computational resources and time, CFD modeling alone could be preferable if similar results are found with decreased computational cost.

Before comparing models, model validation was done. As mentioned in Section 2.5.4.8, computational modeling is limited in its ability as a predictive tool. To offer evidence against the deleterious effects of some of these limitations, model validation was sought using PCMRI taken from the midplane of the RPA. These data were not used in the set-up of the simulation. The PCMR imaging set was analyzed in MATLAB and velocity contours were then compared to those found in FLUENT using the transient linear elastic FSI model. Figure 4.4 shows a comparison of these velocity contours at three different points throughout the patient's cardiac cycle. It is clear in this figure that there are some existing discrepancies between the model results and the blood flow that realistically occurred in this patient. At Point A, which occurred mid-systole, the two velocity contours were similar qualitatively and quantitatively, but the FLUENT model predicted slightly lower velocities. This was also true for Point B, which represented peak systole. Point C was similar for both models, which were both dominated by slower moving fluids at the start of diastole. These results suggest similarities between the CFD models and realistic blood flow through the PA of this patient, but there are certainly differences. As always, all computational results should be weighed against the assumptions applied to the model and other miscellaneous limitations of the study. It is important to note that PCMR measures thruplane velocity and the FLUENT contours illustrate velocity magnitude at the contour slice. The thruplane velocity is the velocity of the fluid flowing perpendicular to a specific cross-section, while the velocity magnitude incorporates all three (*x*, *y*, and *z*) components.

In addition to model validation, MR imaging allowed for the determination of the prospective patient's AVF flow rate. Work done by Yigla et al. [4] and Dagli et al. [5] had previously found connections between hemodialysis, AVF flow rates, and the development of PH in their patients. Most specifically, Dagli et al. [5] found a mean AVF flow rate of 1.55 ± 0.207 L/min in their PH patients. The patient analyzed in the present study had a mean AVF flow rate of 1.97 L/min. This flow rate is higher than the hypothesized limit for an AVF flow rate that is both effective for dialysis and does not overload the heart, which is currently believed to be approximately 1.5 L/min. It is important to note this is not an exact value or threshold for what might be deemed a safe AVF flow rate. A recent study by Tudoran et al. [116] found significantly higher average AVF flow rates (roughly 1.2 L/min) in PH patients when compared to normotensive patients (< 1 L/min). This study also found a strong correlation between sPAP and the amount of time spent on dialysis ($r = 0.702$, $p < 0.001$) as well as AVF flow rates ($r = 0.583$, $p < 0.001$). Similar correlations were found by Abdelghany et al. [117], who reported moderate connections ($r = 0.529$, $p < 0.05$) between sPAP and AVF flow rate for a variety of patients on hemodialysis. Since the patient analyzed in this study did have PH, the evidence from this study roughly aligns with that from these other studies. This finding would be better supported and made more conclusive with the inclusion of a larger sample size. This would enable correlations and comparisons to be made like those reported by Yigla et al. [4], Dagli et al. [5], Tudoran et al. [116], and Abdelghany et al. [117].

The steady-state models run in this study offered a variety of results, helped troubleshoot FSI issues, and highlighted differences between various PA wall material models.. While there were obvious differences in maximum velocities between the steady-state CFD model (0.650 m/s) , the steady-state linear FSI model (0.855 m/s), and the steady-state hyperelastic FSI model (0.763 m/s), there was not much difference between the volume weighted average velocities for each model.

As with the maximum velocities, the steady-state linear FSI model had the highest volume weighted average velocity (0.231 m/s), whereas the steady-state CFD model (0.224 m/s) and hyperelastic FSI model (0.223) had nearly identical average values. All three models had similar maximum WSS values as well; however, a comparison of average WSS values among the three different models revealed more difference. The steady-state linear FSI model had the highest average WSS value (3.74 Pa) while the steady-state CFD model had the lowest average WSS value (2.64 Pa). These differences are interesting since the transient models, which will be discussed more later on, had only minimal differences in maximum and average values throughout the cardiac cycle. The evidence in this study seems to suggest that steady-state models are affected by differing mechanical wall properties more so than the transient models. This difference could be because of the unrefined mesh used. Including more layers of elements in the PA wall mesh would more accurately predict vessel wall deformation and allow for better comparisons between the effects of material models on PA hemodynamics. Initially, only two layers of elements were included in the PA wall based on the preliminary mesh independence test results (Table 8.2 in Appendix A), which only included two different element sizes. Although the difference between meshes was less than 1%, the number of elements through the PA wall thickness was limited. Following the simulations, an additional mesh independence study (Table 8.3 in Appendix A) was run. This study indicated mesh dependence and a refined and independent mesh was identified, which included four to five layers of elements in the PA wall. However, due to time constraints, the above simulations could not be re-run with the new mesh. It is believed that the mesh used to run these simulations may have underestimated deformation.

Unfortunately, it is difficult to compare findings from these steady-state models to existing literature since nearly all computational studies concerning pulmonary artery blood flow (especially those discussed in this document) simulate blood flow across multiple cardiac cycles. It is worth mentioning, though, the decreased computational cost of these steady-state models. For the steady-state CFD model, convergence was reached in under half an hour. Even the steady-state linear FSI model, which was much more complicated and required more troubleshooting than the rigid wall CFD model, had completed its run in only a few hours. Conversely, reaching convergence for the steady-state hyperelastic FSI model was difficult and required extensive load ramping. This model took over 18 hours to run to completion and returned fluid results that were generally somewhere in between those of the steady-state rigid wall CFD model and the steady-state linear FSI model. The hyperelastic model did predict a maximum deformation of the pulmonary artery that was much larger than that done by the linear elastic model (1.62 mm vs. 0.27 mm), but it does not appear that this difference had much effect on the fluid velocity throughout the fluid domain. And while this hyperelastic model did predict wall deformation values similar to those presented by Zambrano et al. [97] (between 0.2 and 1.2 mm for their PH patient), it did not predict volume weighted average fluid velocities and maximum wall shear stresses notably different from those in the other models. In the future, a larger sample size, a formal statistical analysis, and the development of a hyperelastic transient model should be further pursued to offer more insight into effects of non-linear mechanical properties on FSI models of PA blood flow. It would be incredibly interesting to see if the trends observed in this set of three models would be upheld in a larger and more diverse sample.

While the steady-state models offered interesting points for discussion, the transient models present more technically and clinically relevant potential. For the fluid results throughout the three simulated cardiac cycles, nearly identical maximum velocities, volume weighted average velocities, maximum wall shear stresses, and average wall shear stresses, as evidenced in Table

4.5, were found for the transient rigid-wall CFD model and linear elastic FSI model. Both models exhibited higher maximum velocities at peak systole during the first cardiac cycle; these velocities were lowered slightly during the second and third cardiac cycles. Typically, three cardiac cycles are modeled to limit any start-up effects on the simulation.

The volume weighted average velocities for each model were nearly constant at peak systole during all three cardiac cycles, with the transient linear elastic FSI model having only 1.3% larger values than the transient CFD model. Although the transient linear elastic FSI model had higher maximum WSS values, there was less than 1% difference between the average maximum values at peak systole between the two models. The transient linear elastic FSI model did have higher average WSS values, but both models had average peak systolic values that were not only close to one another, but also close to the average value in the steady-state linear elastic FSI model.

In general, there were only slight differences between results of the transient rigid wall CFD model and the transient linear elastic FSI model; however, the steady-state linear elastic FSI model took only a fraction of the time that the transient model required to run to completion. Based on these results, there seems to be little evidence for accounting for fluid-structure interactions in models of pulmonary artery blood flow if researchers are only interested in hemodynamics and not stress-strain distributions in artery walls. The transient rigid wall CFD model offered comparable results to the transient FSI model while only requiring six hours of run time, whereas the FSI model ran for over 102 hours (4.25 days). These differences may become more prominent with the inclusion of a finer solid mesh with multiple layers of elements in the artery wall. Unless an individual or team has access to a supercomputer or similar high-performance computing hardware, the transient rigid wall CFD models of PA blood flow may be more feasible and more appealing. Despite the increased computational cost, FSI modeling still presents a wealth of information about stress-strain distributions not accessible through CFD modeling alone. In this study, it appeared that PA hemodynamics were mostly unaffected by the inclusion of arterial wall properties in transient models. If future groups are only interested in fluid velocities, fluid pressure gradients, and WSS distributions, FSI modeling may not be worth the increased effort and resources. However, if groups are primarily interested in phenomenon promoting arterial remodeling, vessel stiffening, or changes in the extracellular matrix, FSI modeling is an invaluable tool. FSI modeling allows for the studying of physical processes not easily studied or measured clinically [118]. Properties like vessel deformation and cellular stress-strain distributions can offer insight into how collagen and elastin change in diseased states. Given that collagen fibers have been shown to realign and increase in density by almost 10% as PH develops to an advanced state, it is incredibly important to understand how this reorganization of the extracellular matrix takes place, what properties contribute to the initial reorganization, and how that reorganization can be limited if deemed dangerous [119].

It is difficult to compare clinically relevant results from this study to those presented in earlier work. The consenting patient recruited for this study had been diagnosed with PH via RHC before undergoing cardiac MRI. As noted in studies by Tang et al. [64] and Rabidou and George [60], PH patients have been found to have lower velocities compared to their normotensive counterparts. From their CFD analysis, Rabidou and George [60] found an average maximum peak systolic velocity of 0.904 m/s for their PH patients. These values occurred near the outlets of the RPA and LPA. Tang et al. [64] reported peak systolic velocity values that ranged between 0.6 m/s and 1.8 m/s in the proximal PA of their PH patient and much higher velocities in the distal portions of the RPA and LPA. When referencing the transient rigid wall CFD model, the patient analyzed in this study had an average maximum peak systolic velocity of 0.731 m/s. This value is similar to those reported in these earlier studies and also occurred near the outlets of the RPA and LPA like Rabidou and George [60]. And while mean time-averaged values for WSS were higher (14.4 – 14.8 dyn/cm^2) in this study compared to others, WSS distributions throughout the MPA, RPA, and LPA are similar to those reported by Tang et al. [64] (4.3 ± 2.8 dyn/cm^2) and Rabidou and George [60] (0.758 ± 0.207 dyn/cm^2). With reference to the maximum WSS in models here, predominantly lower WSS values were found throughout the pulmonary artery; like findings from Tang et al. [64] and Rabidou and George [60], who both modeled patients with pre-capillary PH, higher values were found at vessel bifurcations and near the inlets and outlets of the model. It is worth mentioning that the time averaged WSS values for the two transient models in this study (14.4 and 14.8 dyn/cm^2) are closer to the normotensive patients analyzed by Tang et al. [64]. This could be explained by an overestimation of WSS values in this study's models because of limited spatial resolution or the use of zero gauge pressure outlets instead of Windkessel outlets used by Tang et al.[64]; however, the average time-averaged WSS values calculated in this study (CFD: 14.8 dyn/cm^2; FSI: 14.4 dyn/cm^2) are only slightly larger than the 14 dyn/cm^2 reported by Zambrano et al. [97] for their PH patient. The inclusion of CFD models for normotensive control patients could help further compare findings from this study to those presented in literature by offering a baseline or control value to compare PH models to.

Furthermore, the maximum deformation that occurred in this study's model, which took place slightly before peak systole in each cardiac cycle, fell just beneath the range of deformations reported by Zambrano et al. [97] in their FSI model. Using a linear elastic modulus of 2 MPa for the PA walls, Zambrano et al. [97] found deformations between 0.2 and 1.2 mm in their PH model. This study modeled the MPA, RPA, and LPA, assumed blood to be a Newtonian fluid, applied volumetric flow rate waveforms to model inlets, and fixed model inlets and outlets. The transient linear elastic model run in this study presented a maximum deformation of 0.104 mm. Interestingly enough, the steady-state rigid linear elastic FSI model (0.27 mm) and hyperelastic FSI model (1.62 mm) predicted deformations more like those in literature presented by Kong et al. [95] and Zambrano et al. [97]. It is currently unclear why the transient model predicted notably less deformation than the steady-state FSI model, but it could be explained by the increase run time and coupling iterations required to run the transient model. These differences could also be explained by the mesh used to run the models. A finer solid mesh with more layers of elements in the PA wall could lead to more similar deformations among models. Due to complications with element distortion and model instability, it is still currently unknown how a transient hyperelastic FSI model of PA blood flow would measure up to the more traditionally accepted rigid wall CFD models and linear elastic FSI models. Based on the results of the steady-state models, it seems that the hyperelastic FSI model may return only moderate differences for fluid velocity, WSS, and vessel wall deformation. If these differences really are trivial and are shown to be so through a more formal statistical analysis, the computational cost of the hyperelastic FSI model may be too great to be justified in future research projects. However, these models should be run with a much finer solid mesh with multiple layers of elements in the PA wall to more accurately predict deformation and stress-strain distributions so that differences in material models can be better defined.

Finally, for the eight retrospective patients analyzed in this study, there were no statistically significant differences between mPAP and PCWP and the amount of time the patient had spent on dialysis. This finding seems to contrast those reported by Santosh et al. [6], who reported annual sPAP increases of approximately 2.4 mmHg/ year in patients undergoing dialysis. While sPAP was not available in the clinical information pulled for the eight retrospective patients here, it was expected that mPAP would increase in cases of prolonged times on dialysis. The lack of statistical difference between the 3-5 year group and the 7-10 year group could be explained by decreases in diastolic pulmonary artery pressures, assuming sPAP stays the same or rises at a slower rate, or lower pulmonary artery pressures in the 7-10 year group before beginning dialysis, which would require a longer period of time for the patient's sPAPs to increase significantly compared to the 3-5 year group.

The retrospective patients analyzed here had an average mPAP of 42.9 ± 5.74 mmHg, which is slightly higher than a group of seven PH patients formerly analyzed in this lab. These seven patients, which did not have ESRD but did have PH confirmed via RHC, had an average mPAP of 36.0 ± 11.8 mmHg. It is worth mentioning that this sample was a mixture of pre- and post-capillary PH patients. In the Tang et al. [64] study, their five pre-capillary PH patients had an average mPAP of 56.8 ± 9.78 mmHg. The retrospective ESRD-PH patients analyzed here had mPAP values between the patients studied in these earlier works. It is interesting that these ESRD-PH patients seemed to develop PA pressures similar to those found in more severe PH cases and not just pressures slightly above the 20 mmHg threshold used to diagnose PH.

One interesting finding from this group of retrospective patients was that all eight individuals were African American, and five of the eight individuals were female. In this study, the lack of a diverse sample did not further complicate analysis by introducing complex differences due to race and biological sex. However, it is concerning that the sample was African American and predominantly female. Previous work has found higher ESRD prevalence in African Americans and Hispanics compared to Caucasian individuals and in females as opposed to males [2], [120]. Carrero et al. [120] also reported that women tend to report higher symptom burdens and greater symptom severity than men who have progressed to ESRD. While no statistical significance was found between the length of time on dialysis and pulmonary artery pressures, the findings presented here do align with those earlier studies claiming gender and ethnic health disparities. This study echoes the sentiment of earlier work claiming the discrepancies in disease prevalence and progression for both ethnic minorities and women, and further justifies the need for more work to be done to better limit these disparities.

The study discussed in this document was designed to further advance protocol and techniques for modeling PA hemodynamics by quantifying how different mechanical properties for vessel walls affected the results of a model and to offer groundwork for establishing correlations between AVF and PA hemodynamics. As stated before, RHC, which is invasive and time-consuming, is the current gold standard for diagnosing PH. Non-invasive techniques, such as echocardiography and 4D MRI, offer potential for safer and more efficient ways to quantify blood flow in the pulmonary arteries of PH patients. Computational modeling approaches, like CFD and FSI models, can help highlight areas and parameters of interest for physicians to monitor or investigate. Results from this study further demonstrated what computational models of blood flow are able to offer physicians by calculating vessel deformation through the construction of the linear elastic FSI model. In normotensive patients, higher velocities, higher wall shear stresses, and larger deformations have been reported in earlier literature. These parameters, which were all calculated in this study, may prove useful in the future. In larger studies, these parameters could be compared between normotensive and PH patients to help identify non-invasive metrics useful for discriminating between normotensive and hypertensive individuals. Additionally, the retrospective patients analyzed in this study revealed no differences in mPAP and PCWP based on time on dialysis but did support earlier claims of existing health disparities for ethnic minorities and women with ESRD.

5.1 Limitations of the Current Study

This study is limited in a number of ways. The most obvious is the lack of a diverse sample size. Due to complications associated with the COVID-19 outbreak, patient recruitment was made severely more difficult than before. Only one prospective patient was recruited for this study and the imaging set obtained from this patient was the only set used to construct the models discussed throughout this document. Thus, it goes without saying that a larger and more diverse sample size should be used in future studies. This improvement will allow for a more convincing and thorough statistical analysis that may justify the application of that study’s findings to the clinical environment. Until concerns with COVID-19 transmission and pandemic growth are ameliorated, this may be a difficult improvement to implement.

The second most apparent limitation of this study is the use of computational modeling. While incredibly useful for cutting down on physical resources and extreme timeframes associated with physical *in vivo* or *in vitro* experiments, *in silico* experiments are inherently limited in their utility by assumptions and simplifications taken in the model and the residual errors created during the solving of the models [92]. An attempt at validation was included in this study that did offer some support of the model’s results, but there were still discrepancies between the validation imaging sets and those predicted by the FSI model used for the study. One limitation of the mechanical model is the omission of any pre-stressing on the model. In the human body, the PA is under constant stress, even during diastole. The mechanical model constructed in this study assumed no pre-stressing, which is physiologically inaccurate. Since the imaging used to reconstruct the PA geometry was acquired during diastole, this omission is not as severe as it would have been if imaging would have occurred during peak systole. The fixing of inlets and outlets was also physiologically inaccurate. No portion of the PA is rigidly fixed in the human body as it was in the models discussed here. While this boundary condition allowed for increased numerical stability and has been used in other studies [95], [97], it may have unintentionally restricted the PA from deforming in a realistic manner. A more ideal outlet boundary condition for the PA wall might include the use of frictionless rollers or a Robin boundary condition with a specified spring stiffness, which would allow some translational motion. Both of these boundary conditions were used in an FSI model of an AVF done by Guess et al. [67]. Limitations like those aforementioned are associated with all computational studies. Future studies should continue to seek model validation and verification when possible. This validation could include simpler methods of validation, such as those presented here, or more advanced techniques like comparisons to 4D MRI flow fields or physical phantom models.

Lastly, the reduced image quality of MRI compared to CT scans is another study limitation. Using CT, studies like Tang et al. [64] and Kong et al. [95] were able to capture several bifurcations on each side of the PA. This allowed for more physiologically accurate geometries and the observation of both proximal and distal flow in the PA. While MRI conducted on a 1.5 T machine does not allow for the same quality of images that CT does, it is non-ionizing and presents no known harm to patients. In addition to enhanced safety, MRI allows for the calculation of velocity profiles throughout a cardiac cycle that can be used for model validation. This limitation is most certainly a trade-off as it comes at the expense of model quality and resolution, but presents less risk to patients and is often required as standard-of-care for ESRD patients suspected of PH.

5.2 Future Work

Given the findings of this study, the aforementioned limitations, and the existing field of literature pertinent to AVF and PA hemodynamics, there are several logical paths forward. It is still unknown how the inclusion of hyperelastic mechanical properties for the PA walls would affect model results. Based on the results of the steady-state models in this study, it does not appear that hyperelastic wall properties would greatly alter the fluid variables of interest; however, the inclusion of a finer solid mesh with multiple layers of elements in the PA wall could reveal greater differences among models. Future work should be done to further develop a stable, transient hyperelastic FSI model of PA blood flow. Assuming the inclusion of a decently sized patient population, comparisons could be made between CFD models, linear elastic FSI models, and hyperelastic FSI models. Future studies may consider permitting a larger number of coupling iterations for each timestep, a greater number of FLUENT iterations per coupling iteration, and a greater number of substeps in ANSYS Mechanical to prevent model instability and element distortion. Different material models may be used to model vessel hyperelasticity as well. The Holzapfel model, which assumes both hyperelasticity and anisotropy, may be a more physiologically accurate material model to incorporate into future simulations. This model utilizes two groups of fibers that are perpendicular to one another to more accurately mimic vessel deformation and mechanical behavior. Although complicated, this model could be beneficial. Other computational modeling applications, such as ABAQUS (Dassault Systemes, France) and COMSOL (COMSOL, Inc., Sweden), might be considered for future analyses. These applications both have reputable finite element solvers that lend themselves well to non-linear problems. Once transient hyperelastic models are created for PA blood flow, the same approach could be taken for modeling AVF flow. Hyperelastic models, linear elastic models, and rigid wall CFD models could all be compared and differences between models could be better defined. This would help future groups seeking to model PA or AVF flow by better quantifying effects of certain assumptions and could help further develop computational modeling as a non-invasive tool for studying and monitoring PH progression.

When correlated with AVF flow, PA hemodynamic properties may offer more insight into how AVF creation and use during dialysis affects pressures in the right heart and PA. If a large and diverse patient population is recruited and analyzed, some of these metrics may offer physicians improved insight about AVF monitoring and may lead to more informed surgical interventions to prevent the development of PH. Over time, this improvement could lead to fewer incidences of PH development in this patient population, more desirable healthcare outcomes, an enhanced quality of life, and a reduction of health disparities associated with this condition.

CHAPTER 6. CONCLUSIONS

End-stage renal disease is a life-threatening and progressive condition characterized by severely impaired renal function, anemia, and the development of various cardiovascular diseases. The most frequently used method for mitigating effects of this condition is dialysis facilitated through surgically created arteriovenous fistulas. Recent research has suggested that while these fistulas are useful in dialysis, they may lead to the development of PH if too much blood flows through them. Studies have been conducted using computational fluid dynamics to model blood flow in arteriovenous fistulas and in pulmonary arteries, but no studies have modelled blood flow in PAs using a variety of different mechanical properties and no studies have utilized CFD to model PA blood flow in ESRD patients. The objective of this work was to use magnetic resonance imaging (MRI) and computational fluid dynamics (CFD) to model pulmonary artery (PA) blood flow and PA fluid-structure interactions so properties of these models could be related to clinical parameters relevant to PH and ESRD. Steady-state rigid wall CFD models, FSI models using a linear modulus of 2 MPa for the vessel walls, and a hyperelastic FSI model were constructed using patient-specific boundary conditions and mechanical properties from Azadani et al. [113] and Zambrano et al. [97]. A transient rigid wall CFD model and linear elastic FSI model were also created using similar properties and methodologies. It was found that while steady-state models differed noticeably based on the mechanical behavior of the walls, the transient fluid models are mostly unaffected. Despite the transient FSI model requiring almost 16 times more run time than the CFD model, only minor differences were found in peak systolic maximum and volume weighted average velocity values (0.6% and 1.3% difference, respectively) and maximum and average WSS values (0.1% and 0.3% difference, respectively) for the two models. In the future, this work may be used to inform groups about the impact of including fluid-structure interactions in models. Additionally, a larger sample size of patients should be recruited so that differences in models and correlations between AVF flow and PA hemodynamic metrics of interest can be better defined. Larger sample sizes will also allow for a better understanding of the assumptions that go into each type of model and how they affect results. Eventually, a better understanding of the underlying relationship between AVF use during dialysis and the subsequent development of PH may reveal parameters that physicians can use to more effectively monitor AVF development. This advanced monitoring protocol could provide physicians with information enabling them to make more informed decisions about surgical intervention, such as fistula ligation. Hopefully, in time, these interventions lead to fewer cases of PH in the ESRD population, improved chances for kidney transplant success for these patients, enhanced quality of life, and an alleviation of the ethnic and socioeconomic health disparities associated with chronic kidney disease, end-stage renal disease, and pulmonary hypertension.

CHAPTER 7. REFERENCES

[1] A. C. Webster, E. V Nagler, R. L. Morton, and P. Masson, “Chronic Kidney Disease.,” *Lancet (London, England)*, vol. 389, no. 10075, pp. 1238–1252, Mar. 2017, doi: 10.1016/S0140-6736(16)32064-5.

[2] U.S. Renal Data System, “2015 USRDS Annual Data Report Volume 2: Epidemiology of Kidney Disease in the United States,” *United States Ren. Data Syst.*, vol. 2, pp. 1–274, 2016, Accessed: May 22, 2019. [Online]. Available: https://www.usrds.org/2015/download/vol2_USRDS_ESRD_15.pdf.

[3] M. Yigla *et al.*, “Pulmonary Hypertension in Patients With End-Stage Renal Disease,” *Chest*, vol. 123, no. 5, pp. 1577–1582, May 2003, doi: 10.1378/chest.123.5.1577.

[4] M. Yigla, Z. Abassi, S. A. Reisner, and F. Nakhoul, “Pulmonary Hypertension in Hemodialysis Patients: An Unrecognized Threat,” *Semin. Dial.*, vol. 19, no. 5, pp. 353–357, Sep. 2006, doi: 10.1111/j.1525-139X.2006.00186.x.

[5] C. E. Dagli *et al.*, “Prevalence of and Factors Affecting Pulmonary Hypertension in Hemodialysis Patients,” *Respiration*, vol. 78, no. 4, pp. 411–415, 2009, doi: 10.1159/000247334.

[6] S. Santosh *et al.*, “Changes in pulmonary artery systolic pressure and right ventricular function in patients with end-stage renal disease on maintenance dialysis,” *Nephrology*, vol. 24, no. 1, pp. 74–80, Jan. 2019, doi: 10.1111/nep.13183.

[7] C. A. O’Callaghan, *The Renal System at a Glance Thrid edition*, Third. Wiley-Blackwell, 2009.

[8] Les Laboratoires Servier, "SMART - Servier Medical ART - 3000 free medical images. Licensed under a creative commons attribution 3.0 license," 2018. https://smart.servier.com/ (accessed May 22, 2019).

[9] American Kidney Fund, "Chronic Kidney Disease (CKD) Symptoms, Treatment, Causes & Prevention - American Kidney Fund (AKF)." http://www.kidneyfund.org/kidney-disease/chronic-kidney-disease-ckd/ (accessed May 22, 2019).

[10] R. Saran *et al.*, "US Renal Data System 2015 Annual Data Report: Epidemiology of Kidney Disease in the United States," *Am. J. Kidney Dis.*, vol. 67, no. 3, pp. A7–A8, Mar. 2016, doi: 10.1053/j.ajkd.2015.12.014.

[11] B. Wong *et al.*, "Comparison of Patient Survival Between Hemodialysis and Peritoneal Dialysis Among Patients Eligible for Both Modalities," *Am. J. Kidney Dis.*, vol. 71, no. 3, pp. 344–351, Mar. 2018, doi: 10.1053/j.ajkd.2017.08.028.

[12] B. Long, A. Koyfman, and C. M. Lee, "Emergency medicine evaluation and management of the end stage renal disease patient," *Am. J. Emerg. Med.*, vol. 35, no. 12, pp. 1946–1955, Dec. 2017, doi: 10.1016/j.ajem.2017.09.002.

[13] H.-U. Meier-Kriesche, J. A. Arndorfer, and B. Kaplan, "The impact of body mass index on renal transplant outcomes: a significant independent risk factor for graft failure and patient death.," *Transplantation*, vol. 73, no. 1, pp. 70–4, Jan. 2002, Accessed: May 22, 2019. [Online]. Available: http://www.ncbi.nlm.nih.gov/pubmed/11792981.

[14] E. Nehus, "Obesity and chronic kidney disease," *Curr. Opin. Pediatr.*, vol. 30, no. 2, pp. 241–246, Apr. 2018, doi: 10.1097/MOP.0000000000000586.

[15] C. P. Kovesdy, S. L. Furth, C. Zoccali, and on behalf of the W. K. D. S. World Kidney Day Steering Committee, “Obesity and Kidney Disease: Hidden Consequences of the Epidemic.,” *Can. J. kidney Heal. Dis.*, vol. 4, p. 2054358117698669, 2017, doi: 10.1177/2054358117698669.

[16] P. Ravani *et al.*, “Associations between Hemodialysis Access Type and Clinical Outcomes: A Systematic Review,” *J. Am. Soc. Nephrol.*, vol. 24, no. 3, pp. 465–473, Mar. 2013, doi: 10.1681/ASN.2012070643.

[17] K. B. Quencer and M. Arici, “Arteriovenous Fistulas and Their Characteristic Sites of Stenosis,” *Am. J. Roentgenol.*, vol. 205, no. 4, pp. 726–734, Oct. 2015, doi: 10.2214/AJR.15.14650.

[18] C. Martin, R. Pillai, and R. Pillai, “Dialysis Access Anatomy and Interventions: A Primer.,” *Semin. Intervent. Radiol.*, vol. 33, no. 1, pp. 52–5, Mar. 2016, doi: 10.1055/s-0036-1578811.

[19] K. J. Woodside *et al.*, “Arteriovenous Fistula Maturation in Prevalent Hemodialysis Patients in the United States: A National Study,” *Am. J. Kidney Dis.*, vol. 71, no. 6, pp. 793–801, Jun. 2018, doi: 10.1053/j.ajkd.2017.11.020.

[20] J. M. MacRae *et al.*, “Arteriovenous Access Failure, Stenosis, and Thrombosis.,” *Can. J. kidney Heal. Dis.*, vol. 3, p. 2054358116669126, 2016, doi: 10.1177/2054358116669126.

[21] UCSF Department of Surgery, “Department of Surgery - Vascular Access for Hemodialysis.” https://surgery.ucsf.edu/conditions--procedures/vascular-access-for-hemodialysis.aspx (accessed May 22, 2019).

[22] L. Zhang *et al.*, “Prevalence and risk factors for pulmonary arterial hypertension in end-stage renal disease patients undergoing continuous ambulatory peritoneal dialysis,” *Ren. Fail.*, vol. 38, no. 5, pp. 815–821, May 2016, doi: 10.3109/0886022X.2015.1103637.

[23] G. Simonneau *et al.*, “Haemodynamic definitions and updated clinical classification of pulmonary hypertension,” *Eur. Respir. J.*, vol. 53, no. 1, p. 1801913, Dec. 2018, doi: 10.1183/13993003.01913-2018.

[24] M. M. Hoeper, H.-A. Ghofrani, E. Grünig, H. Klose, H. Olschewski, and S. Rosenkranz, “MEDICINE Pulmonary Hypertension,” pp. 73–84, 2017, doi: 10.3238/arztebl.2017.0073.

[25] M. E. Sise, A. M. Courtwright, and R. N. Channick, “Pulmonary hypertension in patients with chronic and end-stage kidney disease,” *Kidney Int.*, vol. 84, no. 4, pp. 682–692, Oct. 2013, Accessed: Mar. 12, 2019. [Online]. Available: http://www.ncbi.nlm.nih.gov/pubmed/23739239.

[26] A. Fadaii, H. Koohi-Kamali, B. Bagheri, F. Hamidimanii, and B. Taherkhanchi, “Prevalence of pulmonary hypertension in patients undergoing hemodialysis.,” *Iran. J. Kidney Dis.*, vol. 7, no. 1, pp. 60–3, Jan. 2013, Accessed: May 24, 2019. [Online]. Available: http://www.ncbi.nlm.nih.gov/pubmed/23314144.

[27] H. Suresh, B. Arun, V. Moger, P. Vijayalaxmi, and K. T. K. M. Mohan, “A prospective study of pulmonary hypertension in patients with chronic kidney disease: A new and pernicious complication,” *Indian J. Nephrol.*, vol. 0, no. 0, p. 0, 2017, doi: 10.4103/ijn.IJN_36_17.

[28] J. Babadjanov, R. Miler, K. Niebauer, and L. Kirksey, “Arteriovenous Fistula Creation for End-Stage Renal Disease May Worsen Pulmonary Hypertension,” *Ann. Vasc. Surg.*, vol. 36, pp. 293.e1-293.e3, Oct. 2016, doi: 10.1016/j.avsg.2016.03.020.

[29] S. Narechania and A. Tonelli, “Hemodynamic Consequences of a Surgical Arteriovenous Fistula,” *Ann. Am. Thorac. Soc.*, vol. 13, no. 2, 2016, doi: 10.1513/ANNALSATS.201509-636CC.

[30] G. Acarturk *et al.*, “The relationship between arteriovenous fistula blood flow rate and pulmonary artery pressure in hemodialysis patients,” *Int. Urol. Nephrol.*, vol. 40, no. 2, pp. 509–513, Jun. 2008, doi: 10.1007/s11255-007-9269-8.

[31] A. UNAL *et al.*, “The long-term effects of arteriovenous fistula creation on the development of pulmonary hypertension in hemodialysis patients,” *Hemodial. Int.*, vol. 14, no. 4, pp. 398–402, Oct. 2010, doi: 10.1111/j.1542-4758.2010.00478.x.

[32] F. Hayati, S. S. Beladi Mousavi, S. M. Mousavi Movahed, and M. Mofrad Bushehri, “Pulmonary hypertension among patients undergoing hemodialysis,” *J. Ren. Inj. Prev.*, vol. 6, no. 2, pp. 122–126, Dec. 2016, doi: 10.15171/jrip.2017.24.

[33] C. Nickson, “Pulmonary Hypertension Echocardiography • LITFL • CCC.” https://litfl.com/pulmonary-hypertension-echocardiography/ (accessed May 22, 2019).

[34] G. Simonneau *et al.*, “Haemodynamic definitions and updated clinical classification of pulmonary hypertension.,” *Eur. Respir. J.*, vol. 53, no. 1, 2019, doi: 10.1183/13993003.01913-2018.

[35] G. A. Cobos, A. Femia, and R. A. Vleugels, “Dermatomyositis: An Update on Diagnosis and Treatment,” *American Journal of Clinical Dermatology*, vol. 21, no. 3. pp. 339–353, 2020, doi: 10.1007/s40257-020-00502-6.

[36] M. R. Fisher *et al.*, “Accuracy of Doppler Echocardiography in the Hemodynamic Assessment of Pulmonary Hypertension,” vol. 179, no. 7, pp. 615–621, Apr. 2009, doi: 10.1164/rccm.200811-1691OC.

[37] A. Shujaat, A. A. Bajwa, F. Al-Saffar, J. Bellardini, L. Jones, and J. D. Cury, “Diagnostic accuracy of echocardiography combined with chest CT in pulmonary hypertension,” *Clin. Respir. J.*, vol. 12, no. 3, pp. 948–952, Mar. 2018, doi: 10.1111/crj.12610.

[38] B. Fei *et al.*, “Impact of severe tricuspid regurgitation on accuracy of systolic pulmonary arterial pressure measured by Doppler echocardiography: Analysis in an unselected patient population,” *Echocardiography*, vol. 34, no. 7, pp. 1082–1088, Jul. 2017, doi: 10.1111/echo.13555.

[39] C. S. Johns *et al.*, “Diagnosis of Pulmonary Hypertension with Cardiac MRI: Derivation and Validation of Regression Models,” *Radiology*, vol. 290, no. 1, pp. 61–68, Jan. 2019, doi: 10.1148/radiol.2018180603.

[40] A. B. Goldberg, W. Mazur, and D. K. Kalra, “Pulmonary hypertension: diagnosis, imaging techniques, and novel therapies,” *Cardiovasc. Diagn. Ther.*, vol. 7, no. 4, pp. 405–417, Aug. 2017, doi: 10.21037/cdt.2017.04.11.

[41] O. Bane *et al.*, “A Non-Invasive Assessment of Cardiopulmonary Hemodynamics with MRI in Pulmonary Hypertension HHS Public Access,” *Magn Reson Imaging*, vol. 33, no. 10, pp. 1224–1235, 2015, doi: 10.1016/j.mri.2015.08.005.

[42] A. Lungu, J. M. Wild, D. Capener, D. . Kiely, A. . Swift, and D. R. Hose, “MRI model-based non-invasive differential diagnosis in pulmonary hypertension,” *J. Biomech.*, vol. 47, no. 12, pp. 2941–2947, Sep. 2014, doi: 10.1016/J.JBIOMECH.2014.07.024.

[43] M. Schäfer *et al.*, “Measuring Flow Hemodynamic Indices and Oxygen Consumption in Children with Pulmonary Hypertension: A Comparison of Catheterization and Phase-Contrast MRI,” *Pediatr. Cardiol.*, vol. 39, no. 2, pp. 268–274, Feb. 2018, doi: 10.1007/s00246-017-1751-1.

[44] Z. Stankovic, B. D. Allen, J. Garcia, K. B. Jarvis, and M. Markl, “4D flow imaging with MRI.,” *Cardiovasc. Diagn. Ther.*, vol. 4, no. 2, pp. 173–92, Apr. 2014, doi: 10.3978/j.issn.2223-3652.2014.01.02.

[45] M. M. P. Driessen *et al.*, “Tricuspid flow and regurgitation in congenital heart disease and pulmonary hypertension: Comparison of 4D flow cardiovascular magnetic resonance and echocardiography,” *J. Cardiovasc. Magn. Reson.*, vol. 20, no. 1, 2018, doi: 10.1186/s12968-017-0426-7.

[46] M. Schäfer *et al.*, “Differences in pulmonary arterial flow hemodynamics between children and adults with pulmonary arterial hypertension as assessed by 4D-flow CMR studies,” *Am. J. Physiol. Circ. Physiol.*, vol. 316, no. 5, pp. H1091–H1104, May 2019, doi: 10.1152/ajpheart.00802.2018.

[47] K. Odagiri *et al.*, “Non-invasive evaluation of pulmonary arterial blood flow and wall shear stress in pulmonary arterial hypertension with 3D phase contrast magnetic resonance imaging,” *Springerplus*, vol. 5, no. 1, p. 1071, Dec. 2016, doi: 10.1186/s40064-016-2755-7.

[48] V. O. Kheyfets *et al.*, “4D magnetic resonance flow imaging for estimating pulmonary vascular resistance in pulmonary hypertension,” *J. Magn. Reson. Imaging*, vol. 44, no. 4, pp. 914–922, Oct. 2016, doi: 10.1002/jmri.25251.

[49] V. O. Kheyfets *et al.*, “Patient-specific computational modeling of blood flow in the pulmonary arterial circulation,” *Comput. Methods Programs Biomed.*, vol. 120, no. 2, pp. 88–101, Jul. 2015, doi: 10.1016/j.cmpb.2015.04.005.

[50] O. Zikanov, *Essential Computational Fluid Dynamics*. Wiley (1721), 2010.

[51] C. Taylor and P. Hood, “A numerical solution of the Navier-Stokes equations using the finite element technique,” *Comput. Fluids*, vol. 1, no. 1, pp. 73–100, Jan. 1973, doi: 10.1016/0045-7930(73)90027-3.

[52] J. Tu, K. Inthavong, and K. K. L. Wong, *Computational Hemodynamics - Theory, Modelling, and Applications*. 2015.

[53] V. O. Kheyfets, W. O’Dell, T. Smith, J. J. Reilly, and E. A. Finol, “Considerations for Numerical Modeling of the Pulmonary Circulation—A Review With a Focus on Pulmonary Hypertension,” *J. Biomech. Eng.*, vol. 135, no. 6, p. 061011, May 2013, doi: 10.1115/1.4024141.

[54] FDA, “Benefits and Risks | FDA,” 2017. https://www.fda.gov/radiation-emitting-products/mri-magnetic-resonance-imaging/benefits-and-risks (accessed May 22, 2019).

[55] ANSYS Inc., “Introduction to ANSYS Fluent (Workshops).pdf,” 2009, Accessed: May 22, 2019. [Online]. Available: https://www.kth.se/social/files/57149285f27654646b25d53b/05-Quality-ANSYS.pdf.

[56] ANSYS Inc., “ANSYS Meshing Advanced Techniques - PADT Lunch & Learn Series,” pp. 1–72, 2016, Accessed: May 22, 2019. [Online]. Available: http://www.padtinc.com/blog/wp-content/uploads/2017/04/Advanced-Techniques-in-ANSYS-Meshing_Blog.pdf.

[57] L. Antiga, B. Ene-Iordache, L. Caverni, G. P. Cornalba, and A. Remuzzi, “Geometric reconstruction for computational mesh generation of arterial bifurcations from CT angiography.,” *Comput. Med. Imaging Graph.*, vol. 26, no. 4, pp. 227–35, Accessed: May 22, 2019. [Online]. Available: http://www.ncbi.nlm.nih.gov/pubmed/12074917.

[58] S. Prakash and C. R. Ethier, “Requirements for mesh resolution in 3D computational hemodynamics.,” *J. Biomech. Eng.*, vol. 123, no. 2, pp. 134–44, Apr. 2001, Accessed: May 22, 2019. [Online]. Available: http://www.ncbi.nlm.nih.gov/pubmed/11340874.

[59] P. Krawczyk, A. Beyene, and D. MacPhee, “Fluid structure interaction of a morphed wind turbine blade,” *Int. J. Energy Res.*, vol. 37, no. 14, pp. 1784–1793, Nov. 2013, doi: 10.1002/er.2991.

[60] J. Rabidou and S. George, “Pulmonary Artery Hemodynamics Using MRI & CFD,” East Carolina University, 2017.

[61] U. Morbiducci, R. Ponzini, D. Gallo, C. Bignardi, and G. Rizzo, “Inflow boundary conditions for image-based computational hemodynamics: Impact of idealized versus measured velocity profiles in the human aorta,” *J. Biomech.*, vol. 46, no. 1, pp. 102–109, Jan. 2013, doi: 10.1016/J.JBIOMECH.2012.10.012.

[62] L. Grinberg and G. E. Karniadakis, “Outflow Boundary Conditions for Arterial Networks with Multiple Outlets,” *Ann. Biomed. Eng.*, vol. 36, no. 9, pp. 1496–1514, Sep. 2008, doi: 10.1007/s10439-008-9527-7.

[63] I. E. Vignon-Clementel, C. Alberto Figueroa, K. E. Jansen, and C. A. Taylor, “Outflow boundary conditions for three-dimensional finite element modeling of blood flow and pressure in arteries,” *Comput. Methods Appl. Mech. Eng.*, vol. 195, no. 29–32, pp. 3776–3796, Jun. 2006, doi: 10.1016/J.CMA.2005.04.014.

[64] B. T. Tang, S. S. Pickard, F. P. Chan, P. S. Tsao, C. A. Taylor, and J. A. Feinstein, “Wall Shear Stress is Decreased in the Pulmonary Arteries of Patients with Pulmonary Arterial Hypertension: An Image-Based, Computational Fluid Dynamics Study,” *Pulm. Circ.*, vol. 2, no. 4, pp. 470–476, Oct. 2012, doi: 10.4103/2045-8932.105035.

[65] E. O. Kung and C. A. Taylor, “Development of a Physical Windkessel Module to Re-Create In Vivo Vascular Flow Impedance for In Vitro Experiments,” *Cardiovasc. Eng. Technol.*, vol. 2, no. 1, pp. 2–14, Mar. 2011, doi: 10.1007/s13239-010-0030-6.

[66] N. Westerhof, J.-W. Lankhaar, and B. E. Westerhof, “The arterial Windkessel,” *Med. Biol. Eng. Comput.*, vol. 47, no. 2, pp. 131–141, Feb. 2009, doi: 10.1007/s11517-008-0359-2.

[67] W. P. Guess, B. D. Reddy, A. Mcbride, B. Spottiswoode, J. Downs, and T. Franz, “Fluid-structure interaction modelling and stabilisation of a patient-specific arteriovenous access fistula,” 2017. Accessed: May 28, 2019. [Online]. Available: https://arxiv.org/pdf/1704.07753.pdf.

[68] Y. I. Cho and K. R. Kensey, “Effects of the non-Newtonian viscosity of blood on flows in a diseased arterial vessel. Part 1: Steady flows,” *Biorheology*, vol. 28, no. 3–4, pp. 241–262, 1991, doi: 10.3233/BIR-1991-283-415.

[69] P. Reymond, P. Crosetto, S. Deparis, A. Quarteroni, and N. Stergiopulos, “Physiological simulation of blood flow in the aorta: Comparison of hemodynamic indices as predicted by 3-D FSI, 3-D rigid wall and 1-D models,” *Med. Eng. Phys.*, vol. 35, no. 6, pp. 784–791, Jun. 2013, doi: 10.1016/j.medengphy.2012.08.009.

[70] Y. Bazilevs, M.-C. Hsu, D. J. Benson, S. Sankaran, and A. L. Marsden, “Computational fluid–structure interaction: methods and application to a total cavopulmonary connection,” *Comput. Mech.*, vol. 45, no. 1, pp. 77–89, Dec. 2009, doi: 10.1007/s00466-009-0419-y.

[71] F. G. Simsek and Y. W. Kwon, “Investigation of material modeling in fluid-structure interaction analysis of an idealized three-layered abdominal aorta: aneurysm initiation and fully developed aneurysms.,” *J. Biol. Phys.*, vol. 41, no. 2, pp. 173–201, Mar. 2015, doi: 10.1007/s10867-014-9372-x.

[72] J. P. Mills, L. Qie, M. Dao, C. T. Lim, and S. Suresh, “Nonlinear Elastic and Viscoelastic Deformation of the Human Red Blood Cell with Optical Tweezers,” 2004.

[73] S. M. Javid Mahmoudzadeh Akherat, K. Cassel, M. Boghosian, M. Hammes, and F. Coe, “A predictive framework to elucidate venous stenosis: CFD & shape optimization,” *Comput. Methods Appl. Mech. Eng.*, vol. 321, pp. 46–69, 2017, doi: 10.1016/j.cma.2017.03.036.

[74] G. T. Carroll, T. M. McGloughlin, P. E. Burke, M. Egan, F. Wallis, and M. T. Walsh, “Wall Shear Stresses Remain Elevated in Mature Arteriovenous Fistulas: A Case Study,” *J. Biomech. Eng.*, vol. 133, no. 2, p. 021003, 2010, doi: 10.1115/1.4003310.

[75] L. D. Browne, K. Bashar, P. Griffin, E. G. Kavanagh, S. R. Walsh, and M. T. Walsh, “The Role of Shear Stress in Arteriovenous Fistula Maturation and Failure: A Systematic Review,” *PLoS One*, vol. 10, no. 12, p. e0145795, Dec. 2015, doi: 10.1371/journal.pone.0145795.

[76] A. Quaini *et al.*, “Validation of a 3D computational fluid–structure interaction model simulating flow through an elastic aperture,” *J. Biomech.*, vol. 45, no. 2, pp. 310–318, Jan. 2012, doi: 10.1016/J.JBIOMECH.2011.10.020.

[77] I. Decorato, Z. Kharboutly, T. Vassallo, J. Penrose, C. Legallais, and A.-V. Salsac, “Numerical simulation of the fluid structure interactions in a compliant patient-specific arteriovenous fistula,” *Int. j. numer. method. biomed. eng.*, vol. 30, no. 2, pp. 143–159, Feb. 2014, doi: 10.1002/cnm.2595.

[78] F.-K. Benra, H. J. Dohmen, J. Pei, S. Schuster, and B. Wan, “A Comparison of One-Way and Two-Way Coupling Methods for Numerical Analysis of Fluid-Structure Interactions,” *J. Appl. Math.*, vol. 2011, pp. 1–16, Nov. 2011, doi: 10.1155/2011/853560.

[79] S. T. Ha, L. C. Ngo, M. Saeed, B. J. Jeon, and H. Choi, “A comparative study between partitioned and monolithic methods for the problems with 3D fluid-structure interaction of blood vessels,” *J. Mech. Sci. Technol.*, vol. 31, no. 1, pp. 281–287, 2017, doi: 10.1007/s12206-016-1230-2.

[80] A. Miettinen and T. Siikonen, “Application of pressure- and density-based methods for different flow speeds,” *Int. J. Numer. Methods Fluids*, vol. 79, no. 5, pp. 243–267, Oct. 2015, doi: 10.1002/fld.4051.

[81] ANSYS Fluent, “FLUENT 6.3 User’s Guide - 25.9.1 Choosing the Pressure-Velocity Coupling Method.” https://www.sharcnet.ca/Software/Fluent6/html/ug/node1021.htm (accessed May 30, 2019).

[82] I. E. Barton, “Comparison of SIMPLE- and PISO-type algorithms for transient flows,” *Int. J. Numer. Methods Fluids*, vol. 26, no. 4, pp. 459–483, Feb. 1998, doi: 10.1002/(SICI)1097-0363(19980228)26:4<459::AID-FLD645>3.0.CO;2-U.

[83] M. Kuron, “3 Criteria for Assessing CFD Convergence,” *Engineering.com*, 2015. https://www.engineering.com/DesignSoftware/DesignSoftwareArticles/ArticleID/9296/3-Criteria-for-Assessing-CFD-Convergence.aspx (accessed May 30, 2019).

[84] T. Papaioannou and C. Stefanadis, “Vascular Wall Shear Stress: Basic Principles and Methods,” *Hell. J. Cardiol.*, vol. 46, pp. 9–15, 2005, Accessed: May 31, 2019. [Online]. Available: https://www.researchgate.net/publication/7929606.

[85] R. Steller and J. Iwko, “New generalized Newtonian fluid models for quantitative description of complex viscous behavior in shear flows,” *Polym. Eng. Sci.*, vol. 58, no. 8, pp. 1446–1455, Aug. 2018, doi: 10.1002/pen.24741.

[86] C. Irace *et al.*, “Arterial remodeling of the common carotid artery after aortic valve replacement in patients with aortic stenosis.,” *Stroke*, vol. 33, no. 10, pp. 2446–50, Oct. 2002, Accessed: May 31, 2019. [Online]. Available: http://www.ncbi.nlm.nih.gov/pubmed/12364736.

[87] M. I. Cybulsky and M. A. Gimbrone, “Endothelial expression of a mononuclear leukocyte adhesion molecule during atherogenesis.,” *Science*, vol. 251, no. 4995, pp. 788–91, Feb. 1991, doi: 10.1126/SCIENCE.1990440.

[88] D. N. Ku, D. P. Giddens, C. K. Zarins, and S. Glagov, “Pulsatile flow and atherosclerosis in the human carotid bifurcation. Positive correlation between plaque location and low oscillating shear stress.,” *Arteriosclerosis*, vol. 5, no. 3, pp. 293–302, Accessed: May 31, 2019. [Online]. Available: http://www.ncbi.nlm.nih.gov/pubmed/3994585.

[89] L. H. Timmins *et al.*, “Focal Association Between Wall Shear Stress and Clinical Coronary Artery Disease Progression,” *Ann. Biomed. Eng.*, vol. 43, no. 1, pp. 94–106, Jan. 2015, doi: 10.1007/s10439-014-1155-9.

[90] C. K. Zarins, M. A. Zatina, D. P. Giddens, D. N. Ku, and S. Glagov, “Shear stress regulation of artery lumen diameter in experimental atherogenesis,” *J. Vasc. Surg.*, vol. 5, no. 3, pp. 413–420, Mar. 1987, doi: 10.1016/0741-5214(87)90048-6.

[91] C. K. Zarins, D. P. Giddens, B. K. Bharadvaj, V. S. Sottiurai, R. F. Mabon, and S. Glagov, “Carotid bifurcation atherosclerosis. Quantitative correlation of plaque localization with flow velocity profiles and wall shear stress.,” *Circ. Res.*, vol. 53, no. 4, pp. 502–14, Oct. 1983, Accessed: May 31, 2019. [Online]. Available: http://www.ncbi.nlm.nih.gov/pubmed/6627609.

[92] D. Pearce, S. Fischer, F. Huda, and A. Vahdati, “Applications of Computer Modeling and Simulation in Cartilage Tissue Engineering,” *Tissue Engineering and Regenerative Medicine*, vol. 17, no. 1. Korean Tissue Engineering and Regenerative Medicine Society, pp. 1–13, Feb. 01, 2020, doi: 10.1007/s13770-019-00216-9.

[93] P. D. Morris *et al.*, “Computational fluid dynamics modelling in cardiovascular medicine,” doi: 10.1136/heartjnl.

[94] B. T. Tang, T. A. Fonte, F. P. Chan, P. S. Tsao, J. A. Feinstein, and C. A. Taylor, “Three-Dimensional Hemodynamics in the Human Pulmonary Arteries Under Resting and Exercise Conditions,” *Ann. Biomed. Eng.*, vol. 39, no. 1, pp. 347–358, Jan. 2011, doi: 10.1007/s10439-010-0124-1.

[95] F. Kong, V. Kheyfets, E. Finol, and X.-C. Cai, “Simulation of unsteady blood flows in a patient-specific compliant pulmonary artery with a highly parallel monolithically coupled fluid-structure interaction algorithm,” Oct. 2018, Accessed: May 28, 2019. [Online]. Available: http://arxiv.org/abs/1810.04289.

[96] A. Hosseinsabet, “Longitudinal deformation of pulmonary artery: A case series study,” *Int. Cardiovasc. Res. J.*, vol. 7, no. 4, pp. 147–149, 2013.

[97] B. A. Zambrano *et al.*, “Image-based computational assessment of vascular wall mechanics and hemodynamics in pulmonary arterial hypertension patients,” *J. Biomech.*, vol. 68, pp. 84–92, Feb. 2018, doi: 10.1016/j.jbiomech.2017.12.022.

[98] P. D. Edwards, R. K. Bull, and R. Coulden, “CT measurement of main pulmonary artery diameter.,” *Br. J. Radiol.*, vol. 71, no. 850, pp. 1018–1020, Oct. 1998, doi: 10.1259/bjr.71.850.10211060.

[99] A. Mahammedi, A. Oshmyansky, P. M. Hassoun, D. R. Thiemann, and S. S. Siegelman, “Pulmonary Artery Measurements in Pulmonary Hypertension,” *J. Thorac. Imaging*, vol. 28, no. 2, pp. 96–103, Mar. 2013, doi: 10.1097/RTI.0b013e318271c2eb.

[100] R. Naeije and S. Huez, "Right ventricular function in pulmonary hypertension: physiological concepts," *Eur. Hear. J. Suppl.*, vol. 9, no. suppl_H, pp. H5–H9, Dec. 2007, doi: 10.1093/eurheartj/sum023.

[101] Y.-C. Lai, K. C. Potoka, H. C. Champion, A. L. Mora, and M. T. Gladwin, "Pulmonary arterial hypertension: the clinical syndrome.," *Circ. Res.*, vol. 115, no. 1, pp. 115–30, Jun. 2014, doi: 10.1161/CIRCRESAHA.115.301146.

[102] D. Pike *et al.*, "High resolution hemodynamic profiling of murine arteriovenous fistula using magnetic resonance imaging and computational fluid dynamics," doi: 10.1186/s12976-017-0053-x.

[103] B. S. Dixon, "Why don't fistulas mature?," *Kidney Int.*, vol. 70, no. 8, pp. 1413–1422, Oct. 2006, doi: 10.1038/sj.ki.5001747.

[104] S. Sivanesan, T. V. How, R. A. Black, and A. Bakran, "Flow patterns in the radiocephalic arteriovenous fistula: an in vitro study," *J. Biomech.*, vol. 32, no. 9, pp. 915–925, Sep. 1999, doi: 10.1016/S0021-9290(99)00088-3.

[105] I. Van Tricht, D. De Wachter, J. Tordoir, and P. Verdonck, "Hemodynamics and complications encountered with arteriovenous fistulas and grafts as vascular access for hemodialysis: a review.," *Ann. Biomed. Eng.*, vol. 33, no. 9, pp. 1142–57, Sep. 2005, Accessed: May 28, 2019. [Online]. Available: http://www.ncbi.nlm.nih.gov/pubmed/16175669.

[106] M. Bozzetto, B. Ene-Iordache, P. Brambilla, and A. Remuzzi, "Characterization of the flow-field in a patient-specific model of arteriovenous fistula for hemodialysis," 2016. Accessed: May 28, 2019. [Online]. Available: http://villacamozzi.marionegri.it/~bogdan/downloads/Bozzetto_CAE_2016.pdf.

[107] Y. He, Y.-T. Shiu, D. B. Pike, P. Roy-Chaudhury, A. K. Cheung, and S. A. Berceli, "Comparison of hemodialysis arteriovenous fistula blood flow rates measured by Doppler ultrasound and phase-contrast magnetic resonance imaging," *J. Vasc. Surg.*, vol. 68, no. 6, pp. 1848-1857.e2, Dec. 2018, doi: 10.1016/J.JVS.2018.02.043.

[108] B. Ene-Iordache, L. Mosconi, G. Remuzzi, and A. Remuzzi, "Computational fluid dynamics of a vascular access case for hemodialysis.," *J. Biomech. Eng.*, vol. 123, no. 3, pp. 284–92, Jun. 2001, Accessed: May 29, 2019. [Online]. Available: http://www.ncbi.nlm.nih.gov/pubmed/11476373.

[109] N. DePaola, P. F. Davies, W. F. Pritchard, L. Florez, N. Harbeck, and D. C. Polacek, "Spatial and temporal regulation of gap junction connexin43 in vascular endothelial cells exposed to controlled disturbed flows in vitro," *Proc. Natl. Acad. Sci.*, vol. 96, no. 6, pp. 3154–3159, Mar. 1999, doi: 10.1073/pnas.96.6.3154.

[110] M. Sigovan, V. Rayz, W. Gasper, H. F. Alley, C. D. Owens, and D. Saloner, "Vascular Remodeling in Autogenous Arterio-Venous Fistulas by MRI and CFD," *Ann. Biomed. Eng.*, vol. 41, no. 4, pp. 657–668, Apr. , doi: 10.1007/s10439-012-0703-4.

[111] A. M. de Villiers, A. T. McBride, B. D. Reddy, T. Franz, and B. S. Spottiswoode, “A validated patient-specific FSI model for vascular access in haemodialysis,” *Biomech. Model. Mechanobiol.*, vol. 17, no. 2, pp. 479–497, Apr. 2018, doi: 10.1007/s10237-017-0973-8.

[112] S. M. George, L. M. Eckert, D. R. Martin, and D. P. Giddens, “Hemodynamics in Normal and Diseased Livers: Application of Image-Based Computational Models,” *Cardiovasc. Eng. Technol.*, vol. 6, no. 1, pp. 80–91, Dec. 2015, doi: 10.1007/s13239-014-0195-5.

[113] A. N. Azadani *et al.*, “Biomechanical comparison of human pulmonary and aortic roots,” *Eur. J. Cardio-thoracic Surg.*, vol. 41, no. 5, pp. 1111–1116, 2012, doi: 10.1093/ejcts/ezr163.

[114] K. S. Hunter *et al.*, “In vivo measurement of proximal pulmonary artery elastic modulus in the neonatal calf model of pulmonary hypertension: development and ex vivo validation,” *J. Appl. Physiol.*, vol. 108, no. 4, pp. 968–975, Apr. 2010, doi: 10.1152/japplphysiol.01173.2009.

[115] O. H. Yeoh, “Some forms of the strain energy function for rubber,” *Rubber Chem. Technol.*, vol. 66, no. 5, pp. 754–771, Nov. 1993, doi: 10.5254/1.3538343.

[116] M. Tudoran, T. Ciocarlie, A. Mates, S. A. Pescariu, A. Abuawwad, and C. Tudoran, “Pulmonary Hypertension in Patients with End Stage Renal Disease Undergoing Hemodialysis,” *Niger. J. Clin. Pract.* ¦, vol. 23, no. 2, 2020, doi: 10.4103/njcp.njcp_278_19.

[117] M. Abdelghany, W. Mohamad, and A. Elden, “Pulmonary hypertension in patients with end-stage renal disease under regular hemodialysis: a cross-sectional study,” *Egypt. J. Chest Dis. Tuberc.*, vol. 69, no. 1, p. 235, 2020, doi: 10.4103/ejcdt.ejcdt_38_19.

[118] M. Hirschhorn, V. Tchantchaleishvili, R. Stevens, J. Rossano, and A. Throckmorton, “Fluid–structure interaction modeling in cardiovascular medicine – A systematic review 2017–2019,” *Medical Engineering and Physics*, vol. 78. Elsevier Ltd, pp. 1–13, Apr. 01, 2020, doi: 10.1016/j.medengphy.2020.01.008.

[119] E. R. Pursell, D. Vélez-Rendón, and D. Valdez-Jasso, “Biaxial Properties of the Left and Right Pulmonary Arteries in a Monocrotaline Rat Animal Model of Pulmonary Arterial Hypertension,” *J. Biomech. Eng.*, vol. 138, no. 11, Nov. 2016, doi: 10.1115/1.4034826.

[120] J. J. Carrero, M. Hecking, N. C. Chesnaye, and K. J. Jager, “Sex and gender disparities in the epidemiology and outcomes of chronic kidney disease,” *Nature Reviews Nephrology*, vol. 14, no. 3. Nature Publishing Group, pp. 151–164, Mar. 01, 2018, doi: 10.1038/nrneph.2017.181.

APPENDIX A: SUPPLEMENTARY TABLES AND FIGURES

The following chapter contains tables and figures that supplement the aforementioned study. Readers may find them useful if they are interested in more specific details pertaining to the employed methods and observed results of this project. Given below, Table 8.1 provides a summary of the mesh independence test results for the transient CFD model.

Table 8.1. CFD mesh independence test results.

Mesh #	Element Size (mm)	Elements	Average Element Quality	Average Skewness	Average Orthogonal Quality	Velocity at Maximum cMRI Velocity (m/s)	Difference
1	2.5	146,473	0.514	0.267	0.733	0.639	-
2	2	264,620	0.563	0.241	0.758	0.629	-1.56%
3	1.5	560,589	0.625	0.219	0.781	0.639	1.56%
4	1.25	921,076	0.659	0.211	0.788	0.696	8.16%
5	1	1,731,216	0.693	0.205	0.794	0.701	0.70%

Table 8.2 provides results from the mesh independence test conducted on the solid domain of the model.

Table 8.2. Initial mechanical mesh independence test results done with the hyperelastic material model.

Mesh #	Element Size (mm)	Elements	Average Element Quality	Average Skewness	Average Orthogonal Quality	Maximum Deformation (mm)	Difference
1	2	68,937	0.718	0.388	0.61	2.365	-
2	1.5	138,585	0.726	0.379	0.619	2.370	0.20%

Table 8.3 includes additional mesh independence results for meshes that included multiple layers of elements in the vessel walls. This mesh was not used for modeling and may offer improved results.

Table 8.3. Secondary mechanical mesh independence test results done with the linear elastic material model.

Element Size (mm)	Elements	Average Element Quality	Average Skewness	Average Orthogonal Quality	Maximum Deformation (mm)	Difference
2	115130	0.24797	0.55826	0.43605	0.0209	-
1.5	199582	0.33145	0.44684	0.55158	0.030446	45.55%
1	438011	0.45528	0.28838	0.71059	0.03435	12.82%
0.8	572585	0.80924	0.26921	0.72948	0.042614	24.06%
0.6	1281036	0.83863	0.22568	0.77251	0.042674	0.14%
0.5	2122483	0.82753	0.24347	0.75494	0.043043	0.86%

Below, Table 8.4 provides results from the timestep independence test for the transient CFD simulation with varying numbers of timesteps.

Table 8.4. Timestep independence test results for the CFD simulation.

Timesteps	Timestep Size (s)	Maximum Systolic Velocity (m/s)	Maximum Velocity (m/s)	Difference
179	0.013324022	0.222201	0.769964	-
268	0.008899254	0.221656	0.766342	0.47%
357	0.006680672	0.222201	0.744528	2.85%
446	0.005347534	0.222104	0.744267	0.04%

Table 8.5 includes MATLAB output and results for each timestep of the cardiac cycle used to create the transient velocity profile.

Table 8.5. MATLAB output for creation of the transient velocity profile.

Point in Cycle	Time (s)	Vessel Area (cm^2)	Velocity (cm/s)	Flow Rate (cm^3/s)	Diameter (cm)	Maximum WSS (dyn/cm^2)
1	0.0265	9.5016	1.6618	-15.7900	3.4782	0.1449
2	0.053	9.9093	4.4689	-44.2832	3.5520	0.3673
3	0.0795	9.8466	13.4607	-132.5422	3.5408	1.0938
4	0.106	10.1288	21.3647	-216.3987	3.5912	1.7068
5	0.1325	10.5051	21.5944	-226.8516	3.6573	1.6936
6	0.159	9.4389	19.4710	-183.7858	3.4667	1.6127
7	0.1855	10.1288	17.5281	-177.5387	3.5912	1.4017
8	0.212	10.3483	17.7683	-183.8719	3.6299	1.4055
9	0.2385	10.2856	17.1724	-176.6287	3.6188	1.3628
10	0.265	10.4424	15.5202	-162.0685	3.6463	1.2230
11	0.2915	10.6933	14.3983	-153.9644	3.6899	1.1215
12	0.318	10.2542	12.9004	-132.2840	3.6133	1.0272
13	0.3445	10.9755	10.0964	-110.8126	3.7382	0.7782
14	0.371	10.1915	7.5952	-77.4065	3.6023	0.6098
15	0.3975	10.7873	2.0486	-22.0986	3.7061	0.1649
16	0.424	10.3483	-2.4492	25.3451	3.6299	0.1853
17	0.4505	10.1288	-2.0524	20.7889	3.5912	0.1555
18	0.477	10.4424	-0.0156	0.1629	3.6463	0.0061
19	0.5035	10.6933	1.2524	-13.3920	3.6899	0.1040
20	0.53	10.3169	0.8809	-9.0878	3.6244	0.0769
21	0.5565	10.1602	0.2409	-2.4472	3.5967	0.0268
22	0.583	10.5051	-0.4890	5.1373	3.6573	0.0309
23	0.6095	10.7560	1.5623	-16.8045	3.7007	0.1276
24	0.636	9.8779	1.3308	-13.1460	3.5464	0.1152
25	0.6625	10.6619	0.1096	-1.1683	3.6844	0.0156
26	0.689	9.6271	1.2978	-12.4942	3.5011	0.1142
27	0.7155	10.0974	2.1830	-22.0432	3.5856	0.1816
28	0.742	10.0974	2.4132	-24.3675	3.5856	0.2000
29	0.7685	10.2229	-0.1317	1.3466	3.6078	0.0028
30	0.795	9.9093	-0.5163	5.1158	3.5520	0.0336

APPENDIX B: IRB APPROVAL

EAST CAROLINA UNIVERSITY
University & Medical Center Institutional Review Board
4N-64 Brody Medical Sciences Building· Mail Stop 682
600 Moye Boulevard · Greenville, NC 27834
Office **252-744-2914** · Fax **252-744-2284** ·
rede.ecu.edu/umcirb/

Notification of Initial Approval: Expedited

From: Biomedical IRB
To: Veeranna Maddipati
CC:
Date: 11/5/2019
Re: UMCIRB 19-000708
ESRD-Hemodynamics-cMRI

I am pleased to inform you that your Expedited Application was approved. Approval of the study and any consent form(s) occurred on 11/4/2019. The research study is eligible for review under expedited category # 4,5,7. The Chairperson (or designee) deemed this study no more than minimal risk.

Changes to this approved research may not be initiated without UMCIRB review except when necessary to eliminate an apparent immediate hazard to the participant. All unanticipated problems involving risks to participants and others must be promptly reported to the UMCIRB. The investigator must submit a Final Report application to the UMCIRB prior to the Expected End Date provided in the IRB application. If the study is not completed by this date, an Amendment will need to be submitted to extend the Expected End Date. The Investigator must adhere to all reporting requirements for this study.

Approved consent documents with the IRB approval date stamped on the document should be used to consent participants (consent documents with the IRB approval date stamp are found under the Documents tab in the study workspace).

The approval includes the following items:

Name	Description
Consent Form	Consent Forms
Grant Application	Study Protocol or Grant Application
HIPAA-Authorizationv2.docx	HIPAA Authorization
MRI Protocol	Other Medical Procedures/Considerations
MRI Safety Questionnaire	Surveys and Questionnaires
Preparation for research.pdf	HIPAA Authorization
Research on Decedents Form	HIPAA Authorization
Waiver of HIPPA	HIPAA Authorization

For research studies where a waiver of HIPAA Authorization has been approved, each of the waiver criteria in 45 CFR 164.512(i)(2)(ii) has been met. Additionally, the elements of PHI to be collected as described in items 1 and 2 of the Application for Waiver of Authorization have been determined to be the minimal necessary for the specified research.

The Chairperson (or designee) does not have a potential for conflict of interest on this study.

IRB00000705 East Carolina U IRB #1 (Biomedical) IORG0000418
IRB00003781 East Carolina U IRB #2 (Behavioral/SS) IORG0000418